

**HYDRAULIC FRACTURE CONTAINMENT IN
LAYERED RESERVOIRS**

by

Pengju Xing

B. E. in Civil Engineering, Wuhan University, China, 2009

M. S. in Structural Engineering, Tongji University, China, 2012

Submitted to the Graduate Faculty of
the Swanson School of Engineering in partial fulfillment
of the requirements for the degree of

Doctor of Philosophy

University of Pittsburgh

2017

UNIVERSITY OF PITTSBURGH
SWANSON SCHOOL OF ENGINEERING

This dissertation was presented

by

Pengju Xing

It was defended on

June 12th 2017

and approved by

Andrew P. Bunger, PhD, Assistant Professor, Department of Civil and Environmental
Engineering

Robert Enick, PhD, Professor, Department of Chemical and Petroleum Engineering

Jeen-Shang Lin, ScD, Associate Professor, Department of Civil and Environmental
Engineering

Luis Vallejo, PhD, Professor, Department of Civil and Environmental Engineering

Keita Yoshioka, PhD, Staff Research Scientist, Chevron Energy Technology Company, a
division of Chevron U.S.A. Inc.

Dissertation Director: Andrew P. Bunger, PhD, Assistant Professor, Department of Civil
and Environmental Engineering

Copyright © by Pengju Xing
2017

HYDRAULIC FRACTURE CONTAINMENT IN LAYERED RESERVOIRS

Pengju Xing, PhD

University of Pittsburgh, 2017

Hydraulic fracturing has been widely used for enhancing gas and oil recovery. Often the desire is for the hydraulic fractures to be confined in the reservoir layer, while in other cases the desire is to grow through barriers in order to connect production across multiple strata. In either case, accurate prediction of height growth is important for successful design. This research is oriented to study the hydraulic fracture propagation in the layered reservoirs using: 1) fully coupled, lattice type Distinct Element (DEM) simulator, and 2) laboratory experiments carried out using an analogue three-layered medium constructed from transparent polyurethane.

The work is presented in three parts. Firstly, I present experimental validation of several theoretically-predicted asymptotic behaviors, namely for hydraulic fracture growth under conditions of negligible fracture toughness, with growth progressing from early-time radial geometry to large-time blade-like (PKN) geometry. Secondly, I present laboratory experiments comprising a parametric study in hydraulic fracture containment/height growth. There are four observed geometries generated by these experiments: containment, height growth, T-shape growth and the combination of height growth and T-shape. The results indicate that these cases fall within distinct regions when plotted in a parametric space defined by horizontal confining stress contrast between the reservoir and barrier layers as well as the vertical confining stress, both normalized by the fluid pressure. Finally, a numerical study of hydraulic fracture containment in layered reservoirs is carried out. Again, four distinct geometries are observed, depending on the input parameters. These numerical results match

well to relevant experimental benchmarks, and they extend the dimensionless parameters beyond what can be considered in the laboratory configuration.

The results presented in this paper show the vital role of weak interfaces for determining hydraulic fracture height growth. This research shows that neglecting the role of weak interfaces on hydraulic fracture height growth must be done with the utmost of caution and only if the combination of stress conditions, rock strength, and horizontal interface strength can indeed show to correspond to a range where the interface is expected to play a negligible role in limiting the fracture height growth.

TABLE OF CONTENTS

PREFACE	xvi
1.0 LABORATORY MEASUREMENT OF TIP AND GLOBAL BEHAVIOR FOR ZERO-TOUGHNESS HYDRAULIC FRACTURES WITH CIRCULAR AND BLADE-SHAPED (PKN) GEOMETRY	1
1.1 Preamble	1
1.2 Abstract	1
1.3 Introduction	2
1.4 Tip asymptotic behaviors	7
1.4.1 Governing equations	7
1.4.2 Tip solutions	9
1.5 Experimental method	13
1.5.1 Observed tip behavior	16
1.5.2 Comparison of experiments with global solutions	24
1.6 Chapter conclusion	25
2.0 LABORATORY DEMONSTRATION OF HYDRAULIC FRACTURE HEIGHT GROWTH ACROSS WEAK DISCONTINUITIES	28
2.1 Preamble	28
2.2 Abstract	28
2.3 Introduction	29
2.4 Experimental methods	31
2.5 Experimental results	35
2.5.1 Observed behavior	35

2.5.2 Parametric space	39
2.5.3 Experimental results in the proposed parametric space	44
2.5.4 Hydraulic fracture height	48
2.6 Conclusions	50
3.0 LATTICE SIMULATION OF HYDRAULIC FRACTURE CONTAIN-	
MENT IN LAYERED RESERVOIRS	54
3.1 Preamble	54
3.2 Abstract	54
3.3 Introduction	55
3.4 Experimental methods	57
3.5 Lattice model description	58
3.5.1 Geometry and mechanical formulation	58
3.5.2 Fluid flow formulation	61
3.5.3 Joints	62
3.5.4 Macroscopic and spring parameters	63
3.5.5 Toughness calibration	63
3.5.6 Verification problem	66
3.6 Numerical simulations	70
3.6.1 Zero and small toughness vertical interface	78
3.6.2 Medium to large toughness vertical interface	78
3.6.3 Hydraulic fracture height	81
3.6.4 Discussion	84
3.7 Chapter conclusions	87
4.0 CONCLUSIONS	89
APPENDIX A. SQUEEZE OUT METHOD	93
APPENDIX B. INTERFACE FRACTURE TOUGHNESS MEASUREMENT	97
APPENDIX C. HYDRAULIC FRACTURE GROWTH RATE	101
BIBLIOGRAPHY	104

LIST OF TABLES

1.1	Summary of the asymptotic solutions to be compared with the experiments.	19
1.2	Experimental parameters.	19
2.1	κ_T^{-1} in field and experiments with different adhesives in vertical interfaces . .	42
3.1	Fracture toughness with different adhesives in the experiments and the corresponding tensile strength of vertical interface in XSite.	67
3.2	Criteria for fracture geometries based on crack aperture and fluid volume ratio.	73
B1	Fracture toughness for PU specimen with various adhesives	100

LIST OF FIGURES

1.1	Sketch of HF growth from a horizontal well in a reservoir bounded above and below by barriers to height growth, from Bunger et al. (2014) (with permission). The early time behavior is shown to be radial growth, for which the tip region is governed by a local plane strain condition provided the curvature is not too large, as shown experimentally by Bunger & Detournay (2008). Once the radially-growing fracture reaches the barriers, growth is predominantly along the reservoir, forming the blade shape considered by Perkins & Kern (1961) and Nordgren (1972)	3
1.2	Photometrically-measured tip opening for finite (i.e. non-zero) fracture toughness HFs from Bunger & Detournay (2008), with permission. These pertain to radially-growing HFs for which the tip region is under local conditions of plane strain. a) crack opening (w) as a function of distance from the tip (s) normalized by crack radius (R). b) A repeat of the experiment shown in (a) but with large viscous dissipation relative to the energy required for rock fracture. c) A composite image with results of 11 experiments with various relative importance of viscous dissipation compared to rock fracture, showing how all experimental results collapse onto a single tip solution provided by Garagash & Detournay (2000). Please note that the scalings, scaled crack opening and scaled distance defined in Bunger & Detournay (2008) are different from this paper.	5
1.3	Geometry of a general, planar HF, modified from Detournay (2016).	8

1.4	Plane strain tip solution, modified from Detournay (2016), after Garagash & Detournay (2000).	12
1.5	The experimental setup. Sub-blocks 1 and 6 comprise the top barrier; sub-blocks 2 and 5 comprise the reservoir layer; sub-blocks 3 and 4 comprise the bottom barrier. All the interfaces are unbonded. Note that the sketch on the bottom was rotated 90 degrees compared to the figure on the top in order to make it analogue to horizontal layers underground.	17
1.6	Images of the fluid driven fracture captured from the video of Test A: (a) radial stage at $t = 3$ s, $l/H = 0.96$, and (b) blade shape stage at $t = 12$ s, $l/H = 4.76$	18
1.7	Crack opening w vs s along the crack length (x axis) at various stages of Test A	22
1.8	Comparison between measured crack openings w vs s along the crack length and tip asymptotic solutions of (a) Test A- lower confining stress ($\sigma_o = 0.31$ MPa) and (b) Test B-higher confining stress ($\sigma_o = 0.74$ MPa) at two different stages (radial and blade shape) of fracture propagation.	23
1.9	Comparison of experiment results with tip asymptotic solutions.	24
1.10	Experimental crack opening w along the height (z axis) at $x = 0$ and its comparison with PKN solution. Note some data is obscured by shadows in the image associated with the horizontal interfaces (see Fig. 1.6).	25
1.11	Measured crack length in Test A compared with radial and PKN global solution vs (a) Time and (b) Ratio of crack length over height l/H	26
1.12	Measured crack length in Test A scaled by (a) Radial global solution and (b) PKN global solution vs ratio of crack length over height l/H	26

2.1	The experimental setup, shows the specimen composed of six sub-blocks. Sub-blocks 1 and 6 comprise the top barrier; sub-blocks 2 and 5 comprise the analogue reservoir layer; sub-blocks 3 and 4 comprise the bottom barrier. There are three different analogue reservoir heights H_R : 50.8 mm, 25.4 mm and 12.7 mm. The stresses $\sigma_{h,O}$ (horizontal overlayer confining stress), $\sigma_{h,R}$ (horizontal reservoir confining stress), $\sigma_{h,U}$ (horizontal underlayer confining stress) and σ_v (vertical confining stress) are generated by Load 2 and Load 1. Note that there are two directions of load applied (Load 2 and Load 1) and the other direction is free, however the crack growth orientation is restricted to the planes between the blocks so that the horizontal stress (Load 2) is analogous to the minimum stress.	32
2.2	Typical fracture propagation for the four cases in the bonded tests: (a) Fracture containment, (b) Limited height growth, (c) T-shape, (d) Limited height growth and T-shape (there are two directions of views required for complete observation). The crack region is outlined by blue lines. Sub-blocks 1 and 6 comprise the top barrier; 2 and 5 comprise the analogue reservoir layer; 3 and 4 comprise the bottom barrier.	37
2.3	Pressure evolution for cases with and without notches. The blue solid line shows a typical 50.8 mm analogue reservoir test without a notch ($\sigma_v = 0.94$ MPa, $\sigma_{h,B} = 0.39$ MPa, $\sigma_{h,R} = 0.16$ MPa). The red dashed line shows a typical 12.7 mm analogue reservoir test with notch ($\sigma_v = 0.99$ MPa, $\sigma_{h,B} = 0.55$ MPa, $\sigma_{h,R} = 0.23$ MPa). Here End of Test (EOT) is designated when the fracture reaches the specimen boundary. The inset describes the geometry of limited height growth.	38
2.4	Pressure record for bonded tests (medium toughness) with a notch corresponding to: (a) Fracture containment, (c) T-shape, and (c) Limited height growth and T-shape. The inset in each subfigure describes the corresponding fracture geometry. Note limited height growth is shown in Figure 2.3.	40

2.5 Range of κ_T^{-1} in field and Tape A reduced, also refer to Table 2.1. Note the field reservoirs typically can be classified as: shallow reservoir (500 – 1500 m), transient part (1500 – 2000 m), deep reservoir (2000 – 3500 m). Following Brown & Hoek (1978), the vertical stress of the field σ_v is calculated as $0.027h_z$, and upper and lower bound of field $\sigma_{h,B}$ are $0.0135h_z + 40.5$ and $0.0081h_z + 2.7$ respectively, where h_z is the depth (depth h_z unit is m and stress unit is MPa). 43

2.6 Results of the tests with unbonded vertical interfaces (zero toughness $K_{Ic} = 0$) in the proposed parametric space. Curve A and Curve B are hand drawn. The insets describe the fracture geometries. 44

2.7 Results of the tests with bonded vertical interfaces in the parametric space: (a) with tape A $K_{Ic} = 0.40 \text{ MPa}\cdot\text{m}^{\frac{1}{2}}$, (b)with tape B reduced $K_{Ic} = 0.069 \text{ MPa}\cdot\text{m}^{\frac{1}{2}}$, (c)with tape A reduced $K_{Ic} = 0.026 \text{ MPa}\cdot\text{m}^{\frac{1}{2}}$. The region of different geometries are separated by the hand drawn lines. The insets describe the fracture geometries. 47

2.8 Two types of hydraulic fracture height growth in a layered medium (cross section view). Here H_R is the reservoir height and H_f is the overall fracture height. 49

2.9 Comparison of experimental results of relative height growth H_f/H_R vs \mathcal{H}_b with equilibrium height growth solution. Note that all the data presented here are asymmetric height growth with the analogue reservoir height 12.7 mm and the the maximum fracture length over reservoir height ratio is 6. For the Jeffery and Bungler (2009) experimental result, the maximum fracture length over reservoir height ratio is 3. 51

3.1	The experimental setup from Xing et al. (In Press), showing the specimen composed of six sub-blocks. Sub-blocks 1 and 6 comprise the top barrier; sub-blocks 2 and 5 comprise the analogue reservoir layer; sub-blocks 3 and 4 comprise the bottom barrier. There are three different analogue reservoir heights H_R : 50.8 mm, 25.4 mm and 12.7 mm. The stresses $\sigma_{h,O}$ (horizontal overlayer confining stress), $\sigma_{h,R}$ (horizontal reservoir confining stress), $\sigma_{h,U}$ (horizontal underlayer confining stress) and σ_v (vertical confining stress) are generated by Load 2 and Load 1. Note that there are two directions of load applied (Load 2 and Load 1) and the other direction is free, however the crack growth orientation is restricted to the planes between the blocks so that the horizontal stress (Load 2) is analogous to the minimum stress.	59
3.2	Typical fracture geometries, from Xing et al. (In Press): (a) Fracture containment, (b) Limited height growth, (c) T-shape, (d) Limited height growth and T-shape (there are two directions of views required for complete observation). The crack region is outlined by blue lines.	60
3.3	Fracture toughness calibration for the pre-existing joint: (a) sketch of the calibration experiment, (b) simulated force versus time for the case with $\sigma_t = 0.75$ MPa and $R = 0.004$ m, (c) fracture toughness versus tensile strength for resolution $R=0.004$ m and (d) fracture toughness versus tensile strength for resolution $R=0.003$ m.	65
3.4	The fluid pressure field inside the hydraulic fracture for the verification case. Note the pressure are negative in the outer annulus of the flow disk.	68
3.5	The verification case at 0.058 s (0.013 m radius) showing: (a) Net fluid pressure profile, and (b) crack aperture profile.	69
3.6	Sketch of the numerical model. The model far-field boundary conditions are fixed displacement. Here σ_v is the vertical confining stress, $\sigma_{h,R}$ is the confining stress of reservoir, $\sigma_{h,O}$ is the overlayer horizontal confining stress, and $\sigma_{h,U}$ is the overlayer horizontal confining stress.	71
3.7	Pressure distribution for the vertical interface (top) and the crack aperture profiles (bottom) for a limited height growth case.	74

3.8	Pressure distribution for the vertical interface (top) and the crack aperture profiles (bottom) for a containment case.	75
3.9	Pressure distribution for the horizontal interface (top) and the crack aperture profiles (bottom) for case with a T-shape growth.	76
3.10	Pressure distribution for the vertical interface (top) and horizontal interface (middle) as well as the crack aperture profiles (bottom) for a combination for T-shape and limited height growth case.	77
3.11	Comparison of simulation and experimental results for cases with zero toughness vertical interfaces.	79
3.12	Comparison of simulation and experimental results with both zero and small toughness vertical interfaces.	80
3.13	Comparison of simulation and experimental for cases with medium toughness vertical interfaces.	82
3.14	Comparison of simulation and experimental results for cases with large toughness vertical interfaces.	83
3.15	Comparison of simulation results for relative height growth H_f/H_R versus \mathcal{H}_b with experimental values and proposed curves from Xing et al. (In Press). Note that all the data presented here are characterized by asymmetric height growth upward with the reservoir height 12.7 mm and the maximum fracture length over reservoir height ratio is 6. For the Jeffery and Bungler (2009) experimental result, the maximum fracture length over reservoir height ratio is 3.	85
3.16	Comparison of simulation results for relative height growth H_f/H_R versus \mathcal{H}_b under different \mathcal{H}_v for (a) both small and zero toughness, and (b) medium toughness.	86

A1	Squeeze-out experiments, showing a) two rectangular plates separated by a viscous fluid layer and the fluid flow restricted in x direction, where a_s and b_s are the width and length of the plates and F_s is the applied compressive force, and b) the setup for the experiment with fluid being initially placed between all 3 layers (analogue reservoir and 2 barriers in Figure 2.1) and squeezed out simultaneously by an applied load (note that the fluid among different layers is separated by a thin film to avoid flow across the layers so that the fluid flow is also restricted in x direction). Here $\sigma_{h,U}$ is the stress of the bottom barrier, $\sigma_{h,R}$ is the stress of the analogue reservoir, and $\sigma_{h,O}$ is the stress of the top barrier. Figure adapted from Xing et al. (2016).	95
A2	The results of the squeeze out test, showing a) absorbance variation with time of three layers, and b) the relationship of the stress among different layers ($\sigma_{h,U}$ is the stress of the bottom barrier, $\sigma_{h,R}$ is the stress of the analogue reservoir, and $\sigma_{h,O}$ is the stress of the top barrier). Figure adapted from Xing et al. (2016).	96
B1	The double notch direct tension specimen (after Tada et al. 2000). Here σ is the applied stress, b is the half of the initial crack length, a is the half of the specimen width, and h is the specimen height.	98
B2	The force-displacement of double notch tension tests of PU sub-block bounded by adhesives.	98
B3	Plastic energy absorbed by a test specimen during a critical energy release rate test (after Anderson 2005). Here A_{pl} is the plastic area under the load-displacement curve.	99
C1	Measured crack length in the containment case scaled by a) Radial global solution and b) PKN global solution vs ratio of crack length over height L/H_R . In the test, analogue reservoir height H_R is 12.7 mm. Figure from Xing et al. (2017) (with permission).	102

PREFACE

In the past four years during pursuing my PhD degree, there are many people who helped me. I cannot imagine how I can achieve this without your help. I hope these words would express my gratitude.

I would like first to thank my adviser Dr. Andrew Bungler. He first brought me into the research field of hydraulic fracturing. His guidance, advising and help have made great contributions to my research, from running experiments to writing papers. His profound knowledge, and rigorous and diverse research methods will inspire me throughout my academic life. I am also grateful to his family, Tennille and their kids Callan and Ingrid for warmly hosting us in their home several times.

I would also like to thank Dr. Robert Enick, Dr. Jeen-Shang Lin, and Dr. Luis Vallejo for serving as my committee member. Their suggestions and comments are essential to improve this work.

I would like to thank Charles “Scooter” Hager, who helped to start and build the experiments and overcome many difficulties in the experiments, especially in the casting of polyurethane blocks. I am also grateful to Brandon Ames, Garrett Swarm, Roslyn Gober, who helped to run the tests.

I would like to thank my fellow graduate students in Dr. Andrew Bungler’s team: Navid Zolfaghari, Guanyi Lu, Wei Fu, Di Wang, Qiao Lu and Delal Gunaydin. We had many interesting discussions, which helped me to further understand my research problems.

I gratefully acknowledge the financial support from Chevron Energy Technology Company. I would like to thank Dr. Keita Yoshioka, Dr. Jose Adachi and Amr El-Fayoumi, who brought me a lot of important ideas through the collaboration of the project with Chevron.

I would also like to owe my thanks to Dr. Branko Damjanac from Itasca Consulting Group, who patiently helped to understand several key issues when using XSite.

Finally, and in particular, I would like to thank my wife. Ruoxuan's support and companionship are the most important reason that I can keep exploring the research field. She is always supporting me to pursue my academic career since we met each other, from Shanghai to Pittsburgh. I am also grateful to our coming baby, who is a precious gift inspiring me to complete the work.

1.0 LABORATORY MEASUREMENT OF TIP AND GLOBAL BEHAVIOR FOR ZERO-TOUGHNESS HYDRAULIC FRACTURES WITH CIRCULAR AND BLADE-SHAPED (PKN) GEOMETRY

1.1 PREAMBLE

The content of this chapter comprises a preprint of [Xing et al. \(2017\)](#). It presents the first experimental validation of several theoretically-predicted asymptotic behaviours, namely for hydraulic fracture growth under conditions of negligible fracture toughness, with growth progressing from early-time radial geometry to large-time blade-like (PKN) geometry. The rich nesting of asymptotic solutions uniquely shown in these experiments make hydraulic fracturing theoretically elegant while comprising a formidable challenge for the development of efficient and accurate numerical simulators.

1.2 ABSTRACT

The tip behavior of hydraulic fractures is characterized by a rich nesting of asymptotic solutions, comprising a formidable challenge for the development of efficient and accurate numerical simulators. We present experimental validation of several theoretically-predicted asymptotic behaviors, namely for hydraulic fracture growth under conditions of negligible fracture toughness, with growth progressing from early-time radial geometry to large-time blade-like (PKN) geometry. Our experimental results demonstrate: 1) existence of a asymptotic solution of the form $w \sim s^{3/2}$ (LEFM) in the near tip region, where w is the crack opening and s is the distance from the crack tip, 2) transition to an asymptotic solution

of the form $w \sim s^{2/3}$ away from the near-tip region, with the transition length scale also consistent with theory, 3) transition to an asymptotic solution of the form $w \sim s^{1/3}$ after the fracture attains blade-like (PKN) geometry, and 4) existence of a region near the tip of a blade-like (PKN) hydraulic fracture in which plane strain conditions persist, with the thickness of this region of the same order as the crack height.

1.3 INTRODUCTION

Hydraulic fracturing is widely used in the stimulation of oil and gas reservoirs. Motivated by its importance to hydrocarbon recovery, hydraulic fracture (HF) modeling possesses over 60 years of contributions. Early works focused on simplified geometries of growth, rendering the mathematics more tractable and, when judiciously carried out, maintaining useful ties to real-world geometries. One of the most popular of these early models is the so-called PKN model, named after its developers (Perkins-Kern-Nordgren)([Perkins & Kern 1961](#), [Nordgren 1972](#)). This model is applicable when the HF is confined by barrier layers such that its height remains constant and its length becomes much larger than its height (blade shape), as depicted in [Fig. 1.1](#). The importance of this model is at least two-fold. Firstly its blade-shape is considered to be representative of a commonly-encountered geometry in hydrocarbon reservoirs. [de Pater \(2015\)](#), for example, presents a compilation of fracture diagnostic data (such as microseismic monitoring) from a wide range of reservoir types and shows that HFs almost ubiquitously attain a half-length greater than about 3 times the height, thus approaching and satisfying the requirement for sufficient accuracy of the local elasticity approximation used in the PKN model ([Adachi & Peirce 2008](#)). Secondly, the popularity of the PKN model arises from the adoption of the local elasticity equation first argued by [Perkins & Kern \(1961\)](#) into a generation of so-called “Pseudo-3D” (P3D) simulators ([Settari & Cleary 1984](#)). Indeed approaches that trace their roots to P3D continue to be popular to this day, especially for design models and more recently in conjunction with explicit consideration of growth through a pre-existing discrete fracture network ([Meyer & Bazan 2011](#), [Kresse et al. 2013](#)).

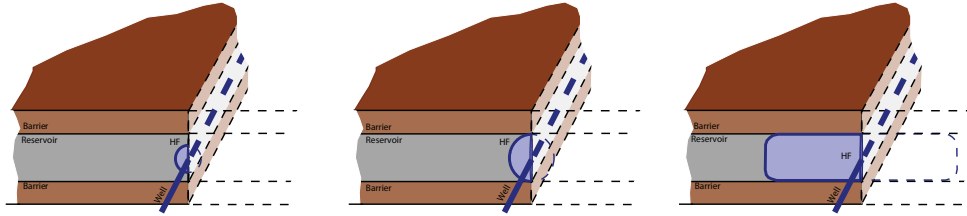


Figure 1.1: Sketch of HF growth from a horizontal well in a reservoir bounded above and below by barriers to height growth, from [Bunger et al. \(2014\)](#) (with permission). The early time behavior is shown to be radial growth, for which the tip region is governed by a local plane strain condition provided the curvature is not too large, as shown experimentally by [Bunger & Detournay \(2008\)](#). Once the radially-growing fracture reaches the barriers, growth is predominantly along the reservoir, forming the blade shape considered by [Perkins & Kern \(1961\)](#) and [Nordgren \(1972\)](#) .

The PKN model is not the only popular model considering a simplified geometry. Other works present plane strain ([Geertsma & De Klerk 1969](#)) and radial ([Spence & Sharp 1985](#)) models. Inevitably these simple geometries have been largely overrun for design and research purposes by numerical simulations - not only the P3D simulators previously mentioned but also a host of others (see reviews in ([Mendelsohn 1984b,a](#), [Warpinski et al. 1993](#), [Adachi et al. 2007](#))) all driving towards more realistic representation of the 3D geometry of HFs. Nonetheless, these early models continue to provide invaluable benchmarks for the development of simulators, but more than that, they also point to some initially subtle but eventually critical challenges associated with the simulation of HF growth. The articulation of these challenges, as well as paths to resolution, have come via a systematic revisiting of these simple geometries ([Savitski & Detournay 2000](#), [Adachi & Detournay 2002](#), [Kovalyshen & Detournay 2010](#)), as well an intensified focus on the behavior of the region near the leading edge of the growing fracture ([Garagash & Detournay 2000](#), [Kovalyshen & Detournay 2010](#)).

Perhaps the most striking outcome of the last 2 decades of research in HF is the realization that the tip region of a HF is: a) critical for the accuracy and computational efficiency of

simulators; and b) difficult to describe, because it consists of different physical processes each associated with its own length scale. For example, in Linear Elastic Fracture Mechanics (LEFM) the fracture tip is usually described by a $w \sim s^{1/2}$ solution, where w is the crack opening and s is the distance from the crack tip (e.g. [Irwin 1957](#)). Commercial HF simulators often use this tip solution in order to impose a propagation condition, computing a stress intensity factor or energy release rate based on the tip opening or on some integral form of the strain energy (e.g. [Rice 1968](#)). However, when the fluid viscosity and propagation velocity are sufficiently large (but still within the quasi-static limit), the solution $w \sim s^{1/2}$ is confined to a small boundary layer near the tip (inner asymptote), and a $w \sim s^{2/3}$ behavior dominates at the observable tip scale (outer asymptote) ([Desroches et al. 1994](#)). The $w \sim s^{2/3}$ is an eigensolution resulting from the combination of the lubrication and elasticity equations with the zero flux boundary condition. This boundary layer structure is predicted by [Garagash & Detournay \(2000\)](#) and experimentally verified by [Bunger & Detournay \(2008\)](#). These prior results are presented in [Fig. 1.2](#).

The importance of this boundary layer structure is examined in detail by [Lecampion et al. \(2013\)](#). Their contribution presents multiple numerical simulators calculating the same problem of HF growth under so-called viscosity-dominated conditions, which means that the $w \sim s^{2/3}$ outer asymptote dominates at the observable scale and the boundary layer with the $w \sim s^{1/2}$ inner asymptote is small relative to the crack length. Their results show that simulators with a propagation condition defined by the $w \sim s^{1/2}$ inner asymptote require 100-1000 times more elements in each modeling dimension to achieve the same accuracy as models that impose a propagation condition based on the $w \sim s^{2/3}$ outer asymptote. These results imply that computation time could be reduced by orders of magnitude without loss of accuracy, provided that the simulator appropriately accounts for the tip behavior that is dominant at the scale of a coarse mesh.

Modeling strategies must also consider the conditions under which other asymptotes will dominate the tip behavior. For example, if the HF growth is guided by a pre-existing, uncemented natural fracture, the inner asymptote at the tip boundary layer is dominated by a $w \sim s^{3/2}$ solution instead of $w \sim s^{1/2}$ ([Garagash & Detournay 2000](#)).

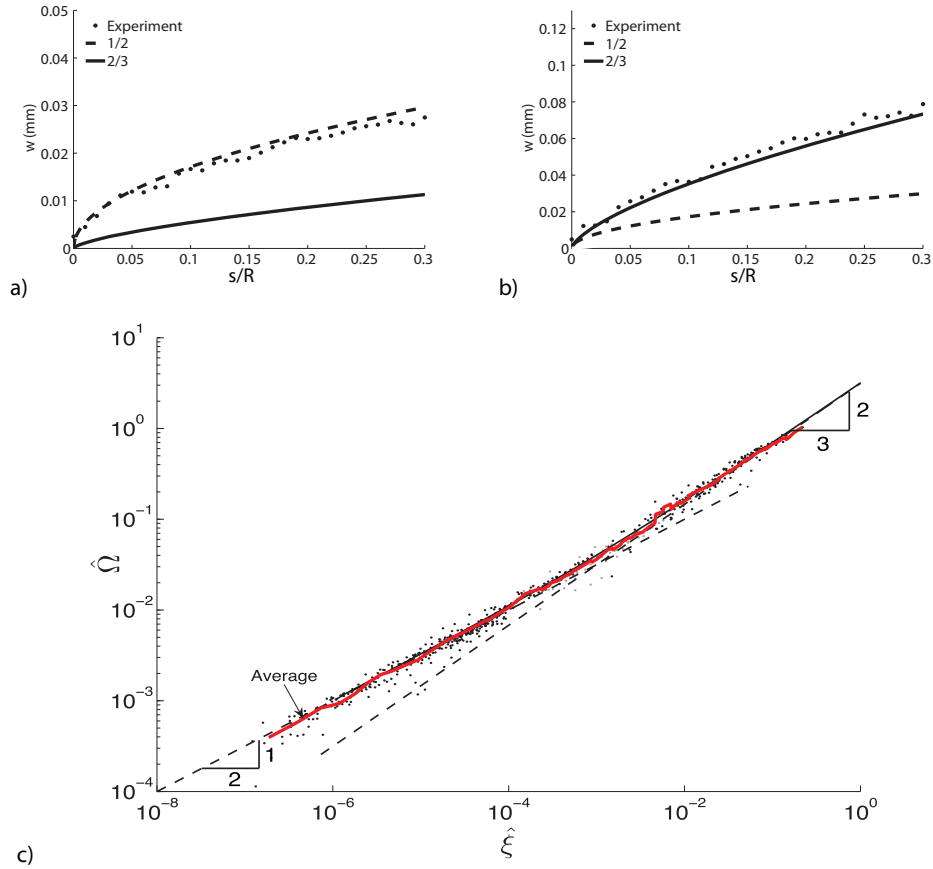


Figure 1.2: Photometrically-measured tip opening for finite (i.e. non-zero) fracture toughness HF from [Bunger & Detournay \(2008\)](#), with permission. These pertain to radially-growing HF for which the tip region is under local conditions of plane strain. a) crack opening (w) as a function of distance from the tip (s) normalized by crack radius (R). b) A repeat of the experiment shown in (a) but with large viscous dissipation relative to the energy required for rock fracture. c) A composite image with results of 11 experiments with various relative importance of viscous dissipation compared to rock fracture, showing how all experimental results collapse onto a single tip solution provided by [Garagash & Detournay \(2000\)](#). Please note that the scalings, scaled crack opening and scaled distance defined in [Bunger & Detournay \(2008\)](#) are different from this paper.

For an HF propagating from a horizontal well into a rock layer bounded by barriers to height growth (see Fig. 1.1), it is expected for the fracture to start propagating radially. The tip behavior on this radial fracture corresponds to the above described transition from $w \sim s^{1/2}$ (or $w \sim s^{3/2}$) to $w \sim s^{2/3}$, depending on the toughness of the rock. At later time, when the HF geometry is such that its half-length exceeds its height by a factor of ~ 3 (PKN geometry), all the previously discussed asymptotes start to be confined into yet another near-tip boundary layer with thickness proportional to the fracture height (Adachi & Peirce 2008), with an outer asymptote predicted to be dominated by a $w \sim s^{1/3}$ term (Kovalyshen & Detournay 2010).

This paper is focused on providing experimental validation for the two tip asymptotic behaviors described above: the presence of the $w \sim s^{3/2}$ solution instead of $w \sim s^{1/2}$ as the inner near-tip asymptote for an HF propagating along a pre-existing joint; and the gradual emergence of a new $w \sim s^{1/3}$ outer asymptote as the fracture geometry transitions from radial into PKN. Neither of these processes were addressed by previous validation experiments done by Bungler & Detournay (2008). We also provide experimental validation of the global PKN solution for the limiting case of an impermeable rock.

The paper firstly describes the formulation of tip asymptotics in different cases, showing the governing equations, asymptotic solution, and length scale associated with dominance of the $w \sim s^{1/2}$ (LEFM), $w \sim s^{3/2}$ (LEFM), $w \sim s^{2/3}$, and $w \sim s^{1/3}$ behaviors. We then describe the experimental method, which entails laboratory HFs carried out under zero-toughness conditions in transparent polyurethane specimens. Detailed comparison with predictions is enabled by photometric measurements, following the method developed by Bungler (2006). We then present comparison of the measured crack opening with the predicted asymptotics, illustrating not only the validity of the solutions but also the boundary layer structure of the tip region of the HF. Finally, we show comparison of measured crack length with the theoretical global solution, validating the solution of Nordgren (1972).

1.4 TIP ASYMPTOTIC BEHAVIORS

1.4.1 Governing equations

The behavior of the tip region has been previously described in detail (see e.g. [Garagash & Detournay 2000](#), [Kovalyshen & Detournay 2010](#)). Here, for completeness, we will present the relevant governing equations and tip solutions. We begin with a general formulation for a planar HF growing with an arbitrary planar shape $\mathcal{A}(t) = \mathcal{A}_f(t) + \mathcal{A}_\lambda(t)$, where $\mathcal{A}_f(t)$ and $\mathcal{A}_\lambda(t)$ are the fluid-filled portion of the fracture and the non-filled “lag” region between the fluid front $\mathcal{C}_f(t)$ and the crack front $\mathcal{C}_c(t)$ (Fig. 1.3). The basic field equations consist of an elasticity relation and Reynolds’ lubrication equation for laminar flow of a Newtonian fluid with viscosity μ . These are given, respectively, by (after e.g. [Peirce & Detournay 2008](#))

$$p - \sigma_o = -\frac{E'}{8\pi} \int_{\mathcal{A}(t)} \frac{w(x', y', t) dS(x', y')}{[(x' - x)^2 + (y' - y)^2]^{3/2}}, \quad (1.1)$$

and

$$\frac{\partial w}{\partial t} = \frac{1}{12\mu} \nabla \cdot (w^3 \nabla p) + Q\delta(x, y). \quad (1.2)$$

Here w is the width (opening) of the crack (HF), p is the fluid pressure, and σ_o is the pre-existing stress (i.e. *in situ* stress) perpendicular to the fracture plane. The elastic behavior of the solid (rock) is described by the plane strain modulus, $E' = E/(1 - \nu^2)$ for Young’s modulus E and Poisson’s ratio ν . Furthermore, $\delta(x, y)$ denotes the Dirac delta function, with the origin of the system of coordinates (x, y) taken to coincide with the injection point, and $Q(t)$ is the volumetric injection rate (a given function of time). Note these equations embed assumptions that the rock is impermeable, isotropic and homogeneous, gravitational forces are negligible, and the fluid is incompressible.

In addition to the elasticity and lubrication equations, propagation is taken according to LEFM, that is, requiring $K_I = K_{Ic}$ for stress intensity factor K_I and fracture toughness K_{Ic} . If the curvature of the crack front is not too large, then the tip region is locally under conditions of plane strain ([Irwin 1957](#), [Rice 1968](#)) and so its asymptotic form is given by

$$w \sim 4 \left(\frac{2}{\pi} \right)^{1/2} \frac{K_{Ic}}{E'} s^{1/2} + O(s^{3/2}). \quad (1.3)$$

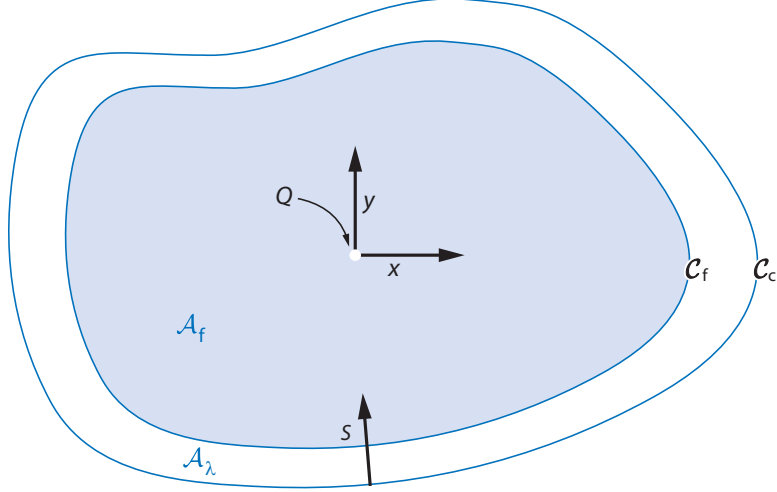


Figure 1.3: Geometry of a general, planar HF, modified from [Detournay \(2016\)](#).

The system is closed by a boundary condition at the moving fluid front. In the case where $\mathcal{C}_f = \mathcal{C}_c$, it is required for the fluid flux to vanish at the crack tip ([Detournay & Peirce 2014](#)). Alternatively, if there is a so-called fluid lag region, then we let

$$p = 0, \quad (x, y) \in \mathcal{A}_\lambda(t). \quad (1.4)$$

In reality, of course, there will be a non-zero pressure in the lag region. This pressure could be due to rapidly evaporating fluid from the fluid front into the tip or to rapid inflow of fluid from a permeable surrounding formation, drawn by the suction of the lag region. However, we will here remain consistent in our assumption of an impermeable formation and we will assume pressure in the lag region to be uniform and to differ from atmospheric pressure (the pressure datum) by an amount which is negligible compared to the far-field minimum stress σ_o (after e.g. [Garagash & Detournay 2000](#)), leaving us with the condition in Eq. (1.4).

In general, solution to this system of equations requires numerical methods. However, for certain cases, approximate (asymptotic) solutions are available. For example, [Savitski & Detournay \(2002\)](#) solve the problem under conditions of radial (circular) growth, as in the early stages portrayed in Fig. 1.1. Taking this radial geometry, and further considering

the limiting case of negligibly-small fracture toughness (relevant to the experiments we will present here), the evolution of the crack radius is given by [Savitski & Detournay \(2002\)](#)

$$l = 0.5277 \left(\frac{E'(2V_c)^3}{\mu} \right)^{1/9} t^{1/9}. \quad (1.5)$$

Relative to the original solution, here we have replaced the product $Q_o t$, where Q_o is a constant injection rate, with $2V_c$, representing the crack volume. Technically the original solution is valid for constant injection rate Q_o . Our *ad hoc* generalization anticipates the present motivation, which is to compare this solution with experimental results. For the experiments, Q_o is not strictly constant due to the compressibility of the injection system, and therefore to ensure the solution is compatible with the actual volume of the crack we introduce V_c , which can be measured in the experiments.

Similarly, [Nordgren \(1972\)](#) provides an approximate solution valid when the HF is much longer than its height and when the height growth is completely restricted by barrier layers, as in the latter stages of [Fig. 1.1](#). In this case, and again introducing the half-volume of the crack V_c , the evolution of the crack length is given by

$$l = 0.68 \left(\frac{E'V_c^3}{2\mu H^4} \right)^{1/5} t^{1/5}, \quad (1.6)$$

where H is the crack height.

1.4.2 Tip solutions

As detailed by [Garagash & Detournay \(2000\)](#), the tip behavior is governed by local plane strain conditions, provided the crack front curvature is not too large. Assuming that the crack propagates with constant velocity V , the storage term $\partial w / \partial t$ in the governing equation [Eq. \(1.2\)](#) can then be expressed for the tip region in terms of a moving coordinate attached to the crack tip s ($s = Vt - x$, [Fig. 1.4](#), inset) as

$$\frac{\partial w}{\partial t} = \frac{Dw}{Dt} + V \frac{\partial w}{\partial s} \quad (1.7)$$

It can be seen that the advective term, $V \partial w / \partial s$, dominates the time derivative Dw / Dt when moving closer to the tip. Hence, the solution near the tip of a propagating finite crack at

time t becomes identical to the stationary solution of semi-finite crack moving at a constant velocity V , which is equal to the instantaneous tip velocity of the finite crack at time t . Therefore, after transformation from a fixed to the moving coordinate system the governing equations can be reduced to (Garagash & Detournay 2000)

$$w^2 \frac{dp}{ds} = 12\mu V, \quad (1.8)$$

and

$$p(s) - \sigma_o = \frac{E'}{4\pi} \int_0^\infty \frac{dw}{d\hat{s}} \frac{d\hat{s}}{s - \hat{s}}. \quad (1.9)$$

The eigensolution simultaneously satisfying both equations is given by Desroches et al. (1994)

$$w \sim 2 \cdot 3^{7/6} \left(\frac{\mu V}{E'} \right)^{1/3} s^{2/3} \quad (1.10)$$

This asymptotic is shown by Garagash & Detournay (2000) to comprise an outer asymptotic, governing the far field behavior with respect to the tip. Meanwhile, the inner asymptotic governing the behavior nearest the tip comes from LEFM (Eq. 1.3). The dominance of the leading order ($w \sim s^{1/2}$) term relative to the next order ($w \sim s^{3/2}$) depends upon the magnitude of K_{Ic} . Specifically

$$w \sim 2.14 \left(\frac{1}{12\mu V} \right)^{1/2} \frac{\sigma_o^{5/2}}{E'^2} s^{3/2}, \quad \kappa \ll 1, \quad (1.11)$$

and

$$w \sim 4 \left(\frac{2}{\pi} \right)^{1/2} \frac{K_{Ic}}{E'} s^{1/2}, \quad \kappa \gg 1, \quad (1.12)$$

where

$$\kappa = \left(\frac{32K_{Ic}^2 \sigma_o}{12\pi\mu V E'^2} \right)^{1/2}. \quad (1.13)$$

The tip behavior from Garagash & Detournay (2000) gives rise to a scaling

$$\hat{\Omega} = w \frac{E'}{\sigma_o L_\mu}, \quad \hat{\xi} = \frac{s}{L_\mu}, \quad (1.14)$$

where the characteristic length is given by

$$L_\mu = \frac{12\mu V E'^2}{\sigma_o^3}. \quad (1.15)$$

Note we have retained the hatted notation for consistency with [Garagash & Detournay \(2000\)](#), and this scaling is different from the scaling used in the results of [Bunger & Detournay \(2008\)](#) presented in Fig. 1.2. In scaling (1.14-1.15), the tip asymptotics (1.11), (1.12) and (1.10) can be expressed as

$$\hat{\Omega} \sim 2.14\hat{\xi}^{3/2}, \quad \hat{\xi} \ll 1, \kappa \ll 1, \quad (1.16)$$

$$\hat{\Omega} \sim \kappa\hat{\xi}^{1/2}, \quad \hat{\xi} \ll 1, \kappa \gg 1, \quad (1.17)$$

$$\hat{\Omega} \sim \frac{1}{2\sqrt{3}}(36\hat{\xi})^{2/3}, \quad \hat{\xi} \gg 1. \quad (1.18)$$

The complete tip solution embodying these asymptotic limits is shown in Fig. 1.4. The $w \sim s^{2/3}$ is herein shown as a far-field (relative to the tip) or outer asymptotic for any value of κ , while the inner behavior has a limit of $w \sim s^{1/2}$ for large κ and $w \sim s^{3/2}$ for small κ . Hence, the experiments of [Bunger & Detournay \(2008\)](#) (see Fig. 1.2) validate this tip structure for $\kappa \gg 1$. However, they do not address $\kappa \ll 1$ conditions, nor do they address how this tip structure is modified at the observational and modeling scale if the fracture transitions to blade-like (PKN) geometry.

In the case of a PKN HF, the crack half length l is much greater than its height H and the elasticity equation can be suitably approximated with a local expression given by ([Perkins & Kern 1961](#), [Nordgren 1972](#))

$$w(x, z, t) = \frac{2}{E'}(H^2 - 4z^2)^{1/2}(p(x, z, t) - \sigma_o). \quad (1.19)$$

The maximum crack opening in each elliptical cross section can be written as

$$W(x, t) = w_{max} = w(x, 0, t) = \frac{2}{E'}H(p(x, t) - \sigma_o). \quad (1.20)$$

Reynolds' lubrication equation (1.2) can be integrated across each elliptical crack cross section to give

$$\frac{\partial W}{\partial t} = \frac{E'}{128\mu H} \frac{\partial^2 W^4}{\partial x^2}. \quad (1.21)$$

In the moving coordinate system ($s = Vt - x$), the lubrication equation becomes

$$V - \frac{E'}{32\mu H} W^2 \frac{dW}{ds} = 0. \quad (1.22)$$

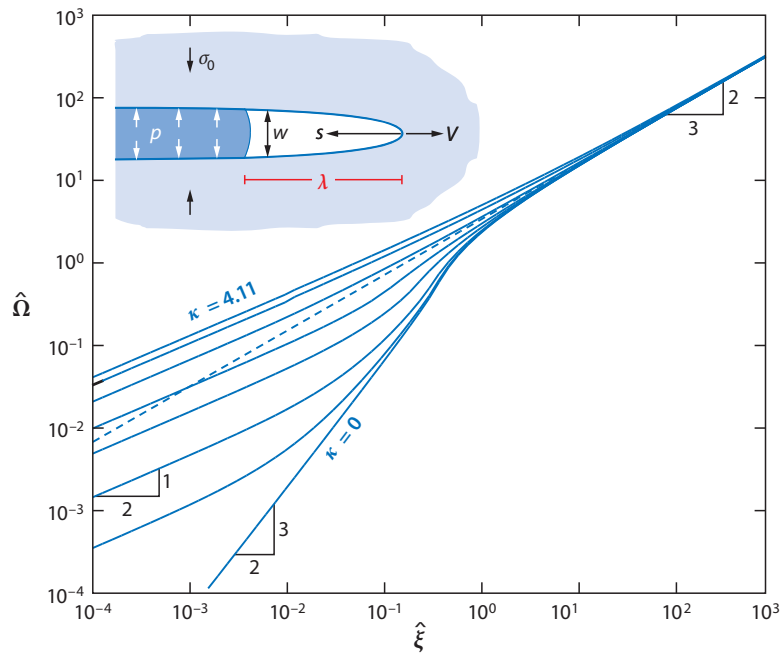


Figure 1.4: Plane strain tip solution, modified from [Detournay \(2016\)](#), after [Garagash & Detournay \(2000\)](#).

An eigensolution simultaneously satisfying local elasticity and the PKN lubrication equation is then given by [Kovalyshen & Detournay \(2010\)](#)

$$W \sim 96^{1/3} \left(\frac{\mu HV}{E'} \right)^{1/3} s^{1/3}. \quad (1.23)$$

The above expression is an outer asymptote that is uniformly valid both in the tip region as well as across the entire, finite-length crack ([Kovalyshen & Detournay 2010](#)). However, as discussed by [Adachi & Peirce \(2008\)](#), there is expected to be a boundary layer near the tip where plane strain conditions persist. In this region, which has a predicted thickness on the order of the fracture height H , the plane strain tip structure of [Garagash & Detournay \(2000\)](#) is expected to be observed.

To enable plotting on the same graph as the plane strain tip structure, it is convenient to scale this solution according to Eqs. (1.14-1.15), resulting in

$$\hat{\Omega} \sim 2 \left(\frac{H}{L_\mu} \right)^{1/3} \hat{\xi}^{1/3}. \quad (1.24)$$

Hence, when plotted in the same scaling as the plane strain tip asymptotics (see Fig. 1.4), the PKN tip solution gives a family of curves depending on the ratio H/L_μ .

1.5 EXPERIMENTAL METHOD

The experiments are designed to enable measurement of the HF length and opening through analysis of images of its growth. Hence, they are performed in a transparent material. The experiments are also designed to focus on the zero toughness ($\kappa \rightarrow 0$) limit. The specimens are therefore constructed from multiple blocks with the HF growing along the unbonded interface between the blocks.

Because the interfaces are unbonded, there is technically no “fracture” in the classical sense of breaking bonds within a material. However, there remains an equivalence to an HF propagating with negligible toughness because: (i) the width and pressure are related by the elasticity equation (1.9) for a crack (derived from superposition of elastic dislocations), (ii) accordingly, there is a sharp moving boundary at the leading edge of the crack whereby

$w = 0$ for $s < 0$, in contrast to flow in a pre-opened slot, and (iii) there exists a well-defined and extensively studied regime of hydraulic fracture growth that is completely independent of K_{Ic} (e.g. Savitski & Detournay 2000, Adachi & Detournay 2002, Kovalyshen & Detournay 2010, Desroches et al. 1994, Lecampion et al. 2013, Peirce & Detournay 2008, Detournay 2016, Savitski & Detournay 2002), where K_{Ic} is relatively small enough that it is irrelevant - i.e. the sensitivity of the solution to its value is negligibly small. Hence, in the regime examined in our experiments, $K_{Ic} = 0$ is mathematically and physically equivalent to cases where K_{Ic} is finite but small enough to be irrelevant. Note also that the use of an unbonded interface as a “zero toughness” hydraulic fracture has precedent in the hydraulic fracturing literature (e.g. Johnson & Cleary 1991, Jeffrey & Bunger 2009, Wu et al. 2008, Garagash et al. 2009, Rohde & Bunger 2009).

Besides designed to consider negligibly small toughness, the experiments are also designed to allow investigation of HF growth through the transition from early-time radial growth to large time blade-like (PKN) growth, as illustrated in Fig. 1.1. Hence the experiments are performed in specimens under stress conditions designed to provide effective barriers to height growth, as demonstrated by Xing et al. (2016). Finally, the experiments are designed to allow L_μ (Eq. 1.15) to be varied relative to the overall size of the HF. This has been enabled by selecting a material with relatively small stiffness (Young’s modulus around 100-200 MPa) compared with actual rocks. Taken together, the analog experiments, illustrated in this section, are able to provide detailed data on HF behavior in selected limiting regimes which have not yet been experimentally validated. Naturally, they are not intended to capture all the physical process of hydraulic fracturing that is specific to rock materials, such as crack nucleation, interaction with heterogeneities and natural fractures, or fluid leakoff.

The experimental setup is depicted in Fig. 1.5. The specimen is comprised of three layers, analogous to a central reservoir layer bounded on each side by a layer that serves as a barrier to fracture growth. Each layer has two sub-blocks. Polyurethane (PU) is selected as the transparent material as its stiffness can be manufactured differently by using particular formulation. The Young’s modulus of the reservoir layer (E) and the barrier layers (E_b) are manufactured as 100 MPa and 200 MPa respectively while the Poisson’s ratio (ν) is 0.48 for all the blocks. The surfaces of the transparent PU sub-blocks are clear and smooth, indicating

the roughness is less than wavelength of visible light (see [Stone & Shafer 1994](#)), and hence at least 2-3 orders of magnitude smaller than typical HF opening magnitudes observed in the experiments. Note that attaining a geometry consistent with the PKN model requires that crack length over height ratio $l/H \geq 3$. In this experimental setup H is 12.7 mm and the maximum half length of the crack l is 76.8 mm, which satisfies the PKN condition (the crack length over height ratio l/H is around 6).

In the experiments, the specimens are firstly loaded symmetrically with hydraulic actuators using two axes of a true tri-axial loading frame. Transparent polymethyl methacrylate (PMMA) blocks are used to evenly spread the load from the smaller actuators to the PU specimens (see [Fig. 1.5](#)). Due to lower stiffness of the analogue reservoir layer, application of confinement (load direction 2 in [Fig. 1.5](#)) gives a lower stress in the reservoir layers than in the barrier layers. Furthermore, through application of loading across the layers (load direction 1, [Fig. 1.5](#)), the stresses on the interfaces between the barrier layers and the reservoir layer are also maintained at larger magnitudes than the stress within the reservoir. After the loading, the fracturing fluid is injected into the reservoir layer through a 3.175 mm injection hole by a syringe pump. Initiation is promoted at the inlet by a 2 mm deep and 10 mm diameter notch. An HF is thus initiated at the reservoir block interface and is contained within the layer because of higher stresses applied in all other interfaces. The leak-off into the horizontal interfaces is prevented by the larger vertical confining stress and the smooth interfaces, as demonstrated by [Xing et al. \(2016\)](#). Direct visual monitoring of the HF growth during the experiments verifies the effectiveness of this approach for generating contained HFs.

The HF growth is monitored directly using a video camera. Based on these images, the crack aperture is obtained by a photometric method described in detail by [Bunger \(2006\)](#). This approach relies on a classical exponential extinction law relating the opening of a crack that is filled with a dye-laden fluid to the loss of light intensity, namely

$$w = k \log_{10} \frac{I_o}{I}. \quad (1.25)$$

Here I_o is the background light intensity and I is the light intensity after the fluid passes through the fluid-filled crack (HF). The photometric constant k is calibrated for our partic-

ular light-camera-fluid combination using fluid-filled wedges of known geometry and further validating the calibration by a plate calibration rig using linear variable differential transformer (LVDT), as detailed in [Bunger \(2006\)](#). Hence the value of $k = 0.25$ mm obtained for these experiments is verified through two calibration methods. The calibration is repeatable within 5%-10%. The same approach is used in the experiments of [Bunger & Detournay \(2008\)](#), showing a similar experimental uncertainty of around 10%. Note also that the value of k embeds a correction for the oblique viewing angle of the camera, which is required due to obstruction of the orthogonal viewing angle by the loading platens.

Throughout the experiments, the fluid is injected at a fixed rate. The fluid pressure is monitored using a pressure transducer that is placed near the location where the injection tube enters the specimen. The fluid used in these experiments is an aqueous solution of glycerin and magenta food dye. The magenta food dye is chosen because it provides maximum absorption of the green light obtained by using a polymer filter placed over a white light source. The laboratory temperature, and hence the fluid and specimen temperature, were maintained at 20° C. At this temperature, the fluid has a viscosity of $\mu = 0.3$ Pa · s, measured with a capillary-type viscometer.

1.5.1 Observed tip behavior

As anticipated from the experimental design, the HF propagates radially at first and then transitions into the blade-like (PKN) geometry, as shown from the images in [Fig. 1.6](#). [Table 1.1](#) shows the summary of the tip asymptotics in radial shape and blade-shape cracks in the experiments respectively. In this section we will contrast the tip behavior through this growth period in two cases, denoted Test A and Test B, with parameter values given in [Table 1.2](#).

The main difference between these cases is the confining stress, which is higher in Test B. Hence L_μ is smaller ([Eq. 1.15](#)) and so a point with the same location s relative to the HF tip (on the order of millimeters to centimeters in these experiments) corresponds to a higher value of $\hat{\xi}$. It is therefore expected that the inner $w \sim s^{3/2}$ behavior will be visible over a greater portion of the HF in Test A than in Test B.

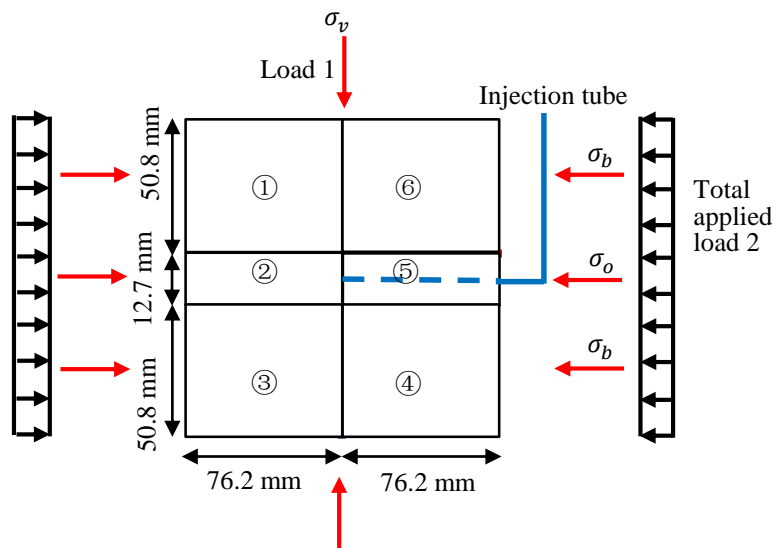
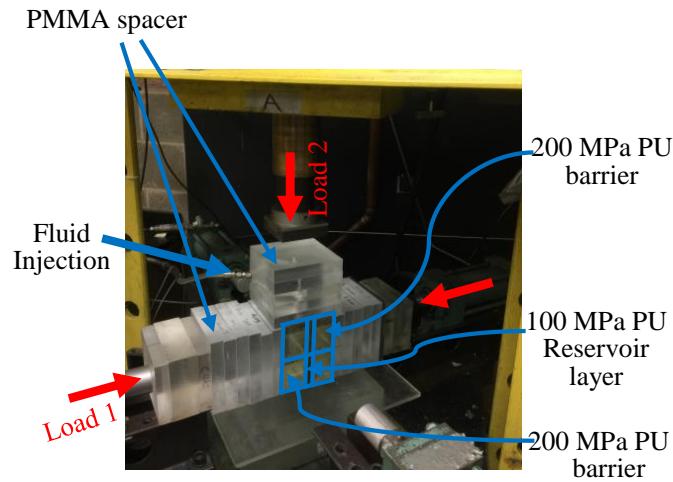


Figure 1.5: The experimental setup. Sub-blocks 1 and 6 comprise the top barrier; sub-blocks 2 and 5 comprise the reservoir layer; sub-blocks 3 and 4 comprise the bottom barrier. All the interfaces are unbonded. Note that the sketch on the bottom was rotated 90 degrees compared to the figure on the top in order to make it analogue to horizontal layers underground.

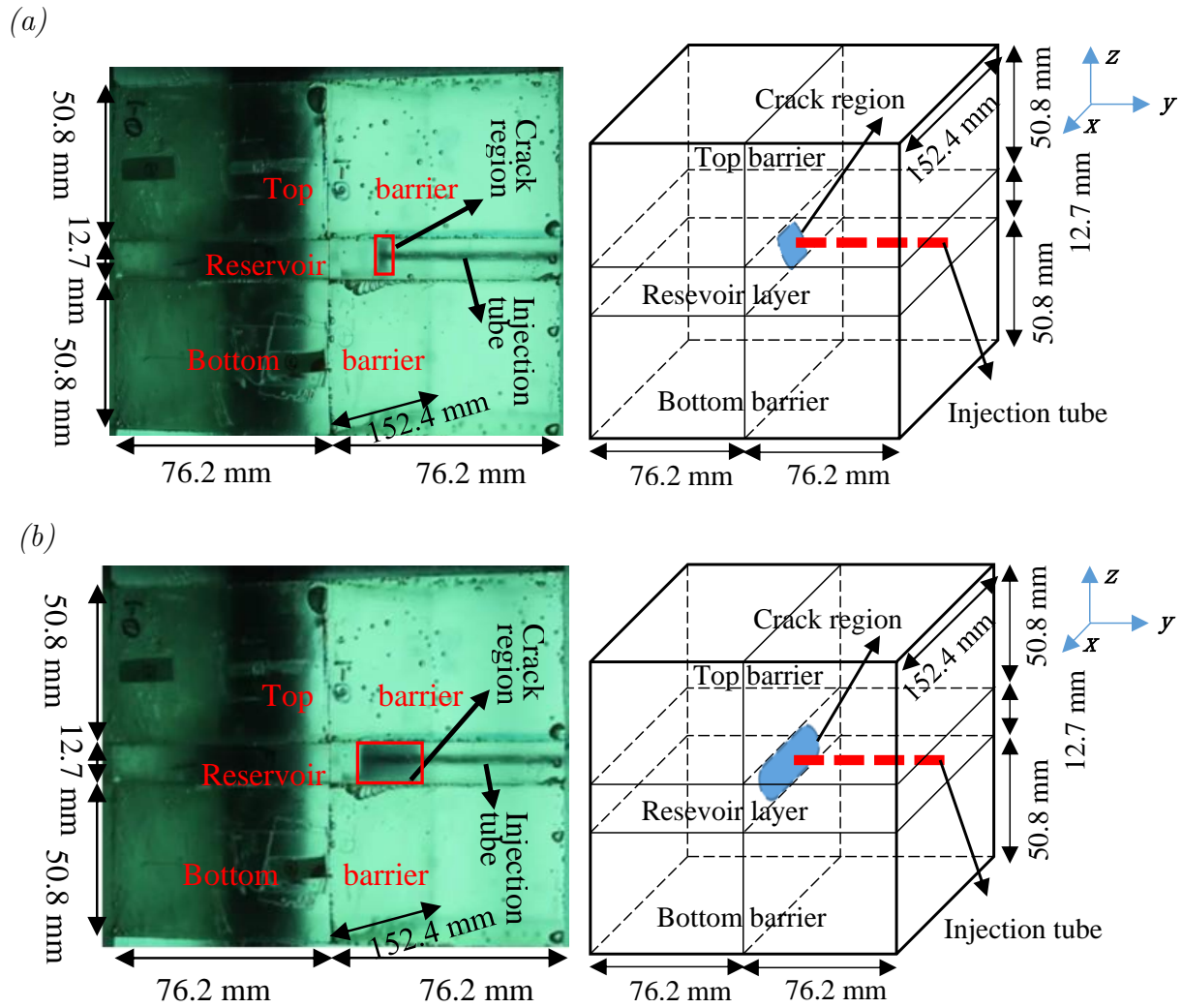


Figure 1.6: Images of the fluid driven fracture captured from the video of Test A: (a) radial stage at $t = 3$ s, $l/H = 0.96$, and (b) blade shape stage at $t = 12$ s, $l/H = 4.76$.

Table 1.1: Summary of the asymptotic solutions to be compared with the experiments.

radial shape crack	inner	$\hat{\Omega} \sim 2.14\hat{\xi}^{3/2}, \kappa \ll 1$
	outer	$\hat{\Omega} \sim \frac{1}{2\sqrt{3}}(36\hat{\xi})^{2/3}$
blade-shape crack	inner	$\hat{\Omega} \sim 2.14\hat{\xi}^{3/2}, \kappa \ll 1;$
	intermediate	$\hat{\Omega} \sim \frac{1}{2\sqrt{3}}(36\hat{\xi})^{2/3}$
	outer	$\hat{\Omega} \sim 2 \left(\frac{H}{L_\mu}\right)^{1/3} \hat{\xi}^{1/3}$

Table 1.2: Experimental parameters.

(a) Measured parameters

Quantity	Test A	Test B	Description
σ_o (MPa)	0.31	0.74	Stress in reservoir layer
σ_b (MPa)	0.74	1.78	Stress in barrier layers
σ_v (MPa)	0.96	1.92	Stress in vertical direction
E (MPa)	100	100	Reservoir Young's modulus
E_b (MPa)	200	200	Barrier Young's modulus
ν, ν_b	0.48	0.48	Reservoir and Barrier Poisson's ratio
μ (Pa·s)	0.3	0.3	Fluid Viscosity
Q (ml/min)	8	8	Pumping rate
H (mm)	12.7	12.7	Reservoir height

(b) Calculated parameters

Quantity	Test A	Test B	Description
L_μ (mm)	6.7	0.39	Characteristic tip solution length

The crack opening w along the crack length at various times for Test A shows existence of a near tip region following the $w \sim s^{3/2}$ as expected (Fig. 1.7). At early time before the length is large relative to height, there appears a transition to $w \sim s^{2/3}$. As time goes on and the length increases relative to the height, the expected $w \sim s^{1/3}$ far field behavior is observed.

Recalling the prediction that $w \sim s^{3/2}$ will be less visible in higher stress case (Test B), Fig. 1.8 further takes comparison between measured HF opening of two snapshots in time for the two tests. One of these corresponds to the radial growth period ($l/H \leq 1$), and the

other corresponds to the PKN growth period ($l/H > 3$). The measurements are compared with the tip asymptotic solutions from Eqs. (1.11, 1.10, and 1.23). Recall that the $w \sim s^{1/2}$ asymptotic (Eq. 1.12) is not applicable for these zero-toughness fractures.

We observe the growth firstly in the the initial stage, at $t = 3$ s in Test A and $t = 2$ s in Test B, wherein the ratio of half crack length over height $l/H \leq 1$ and the geometry corresponds to radial growth. Here the tip asymptotics should follow the plane strain solution. Indeed, as expected, the tip opening transitions from the $w \sim s^{3/2}$ inner solution to the $w \sim s^{2/3}$ outer solution further from the tip at $t = 3$ s in Test A. In contrast, at $t = 2$ s in Test B, only the $w \sim s^{2/3}$ solution is observed. The reason is that in the test with lower confining stress (Test A), the length scale $L_\mu = 6.7$ mm, while in the test with higher confining stress (Test B) $L_\mu = 0.39$ mm. As a result, in the case with lower confining stress (Test A), L_μ is of the same order as the crack radius (≈ 10 mm), resulting in the occurrence of the inner $w \sim s^{3/2}$ asymptote on the observable (crack) scale. In Test B, L_μ is much smaller than the crack scale and so the inner boundary layer over which the $w \sim s^{3/2}$ is valid is too small to be observed. Hence the outer $w \sim s^{2/3}$ asymptote dominates the observable tip region. Note that after initiation, the radial shape stage took place in a very short time and was quickly confined in the vertical direction. The observations are therefore limited to profiles along the length of the HF; we are unable to observe the $w \sim s^{2/3}$ in the height direction because of the containment. Still, in both Test A and Test B, we do not see the crack opening diverge significantly from the $2/3$ tip asymptotics at the “radial” stages in spite of the fact these are not ideally radially growing and we include points that are relatively far from the tip.

As the HF propagates, the crack length increases while the crack height remains constant. When the crack length to height ratio attains $l/H \geq 3$, the local elasticity approximation (Eq. 1.19) is suitable, except in a boundary layer adjacent to the tip with thickness $\sim O(H)$ in which plane strain conditions persist (Adachi & Peirce 2008). Outside of this plane strain boundary layer, the fracture is expected to behave according to the PKN model and so the tip asymptote should follow the $w \sim s^{1/3}$ solution (Eq. 1.23). Indeed, for these examples taken at $t = 12$ s in Test A and $t = 7$ s in Test B, the measured crack opening shows good agreement with the expected $w \sim s^{1/3}$ solution when s is large.

The predicted plane-strain condition in the region close to the tip is also evident in the later-time data for both Test A and Test B. This evidence is provided by the HF opening in a region immediately adjacent to the tip and covering a portion of the HF that is similar to the crack height $H = 12.7$ mm. Specifically, it shows agreement between the $w \sim s^{3/2}$ inner solution in Test A and the $w \sim s^{2/3}$ intermediate solution in Test B when s is small. Note that no evidence of fluid lag is observed. However, fluid lag is not expected to be readily visible in these zero-toughness experiments because there is no change in optical dissipation/reflection due to opening of the interfaces. A similar observation was made by Jeffrey & Bungler (2009), which is in contrast to the clearly-visible lag in Bungler et al. (2005) wherein the lag region entailed a debonding of the blocks. So we must indirectly infer from the good agreement with the predicted near tip asymptotics that any lag that may be present has a negligible impact on the HF behavior.

To further illustrate consistency between the data and the theoretical predictions, Fig. 1.9 shows the test results (including the results of both Test A and Test B) and tip asymptotic solutions, scaled according to Eqs. (1.14) and (1.15). Recall that in this scaling the curves corresponding to the plane strain tip solutions ($w \sim s^{3/2}$ and $w \sim s^{2/3}$) are universal (i.e. there are no parameters one needs to specify in order to draw these curves), while the PKN tip solution ($w \sim s^{1/3}$) depends on the ratio H/L_μ . Hence, in this scaling, Test A and Test B correspond to the same plane strain tip solutions but each has its own PKN tip solution curve because these experiments have a different length scale L_μ . These predictions are compared with the four experimental curves first shown in Fig. 1.8. The results show consistency between the plane strain solution and the data during the radial growth period, with the inner, $w \sim s^{3/2}$ behavior observable in Test A owing to its larger value of L_μ . Upon transition to the blade-shape geometry, the behavior immediately adjacent to the tip continues to follow the plane strain solution while the far field behavior adheres to the PKN ($w \sim s^{1/3}$) solution.

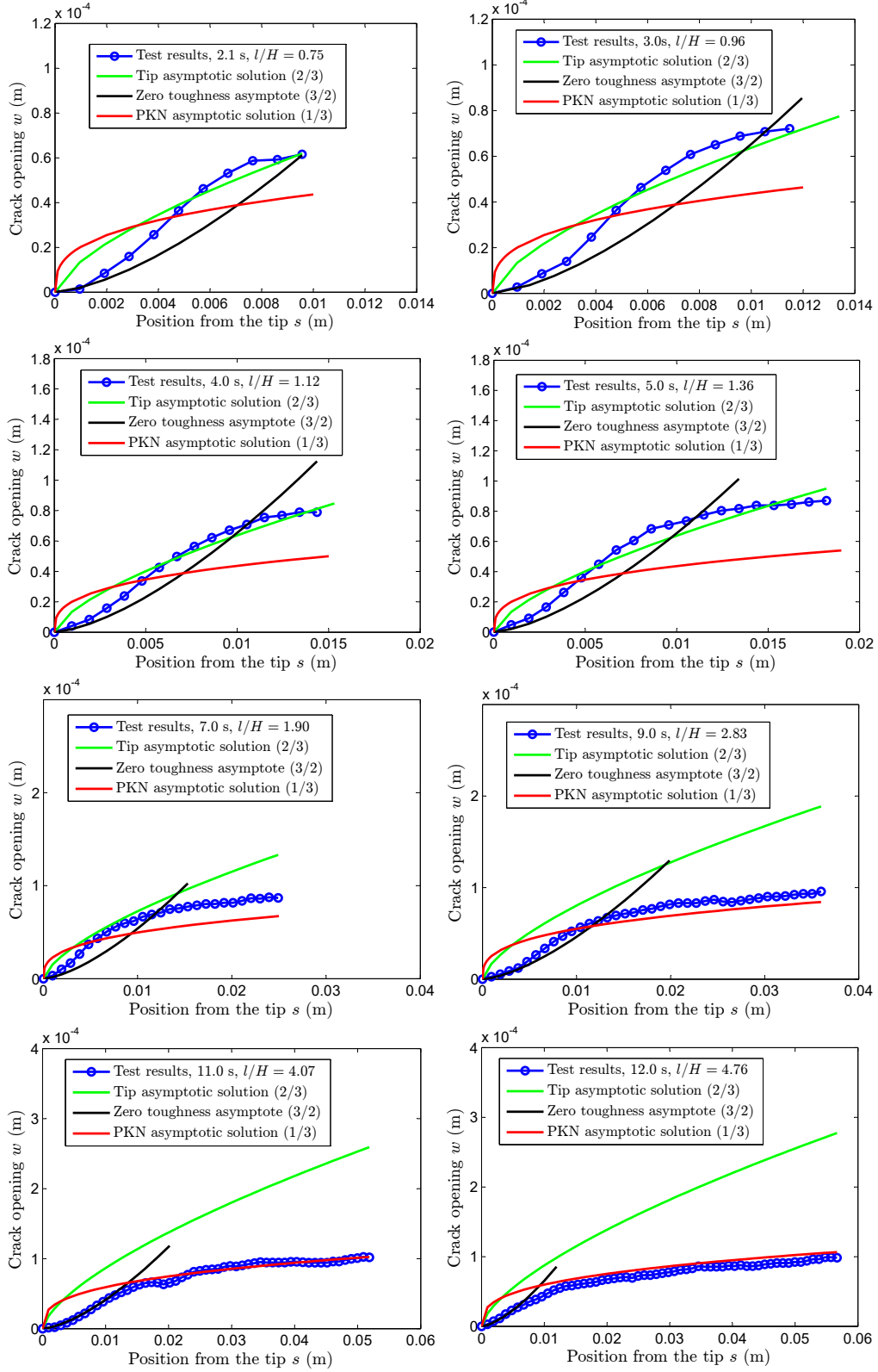


Figure 1.7: Crack opening w vs s along the crack length (x axis) at various stages of Test A

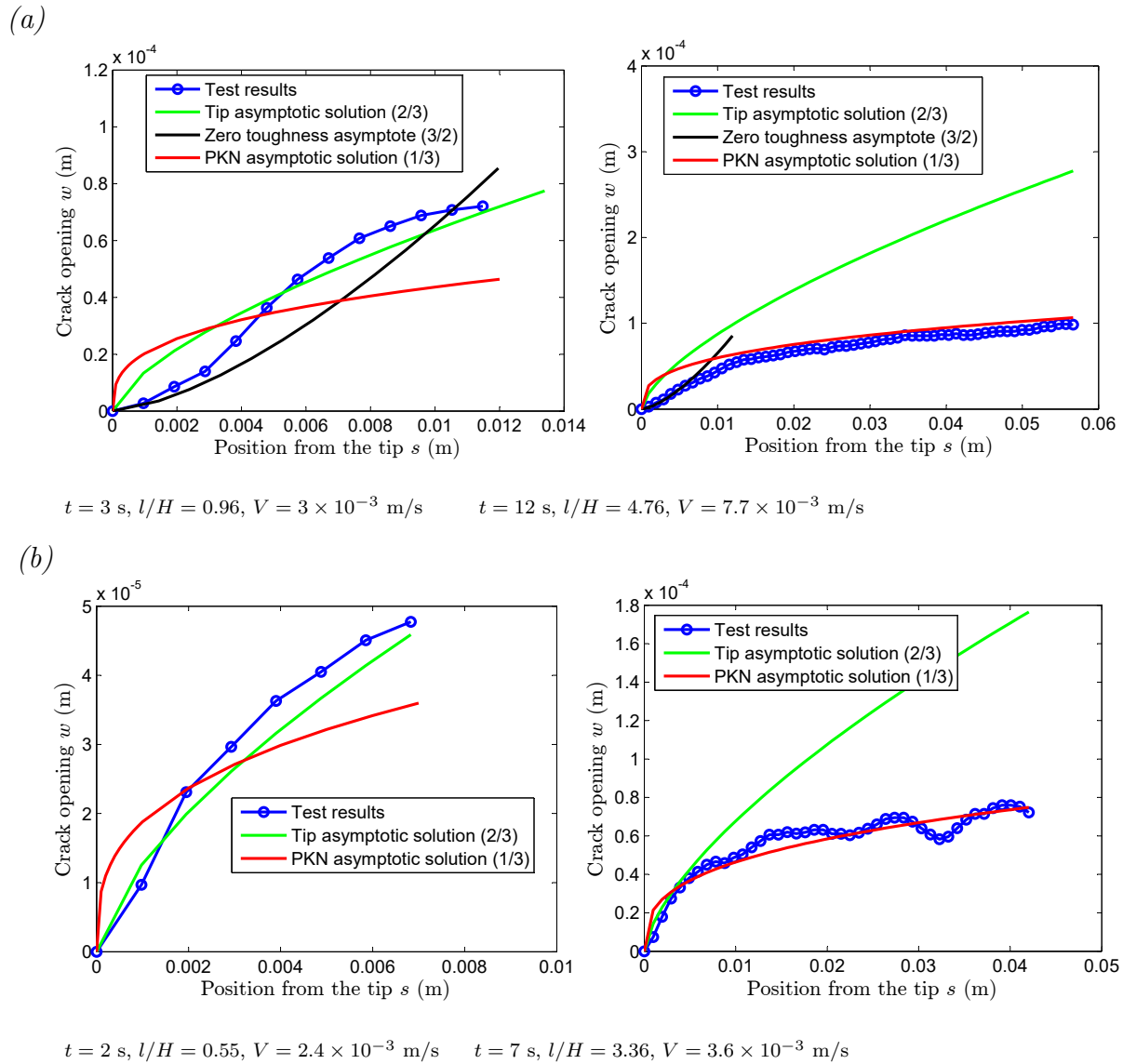


Figure 1.8: Comparison between measured crack openings w vs s along the crack length and tip asymptotic solutions of (a) Test A- lower confining stress ($\sigma_o = 0.31$ MPa) and (b) Test B-higher confining stress ($\sigma_o = 0.74$ MPa) at two different stages (radial and blade shape) of fracture propagation.

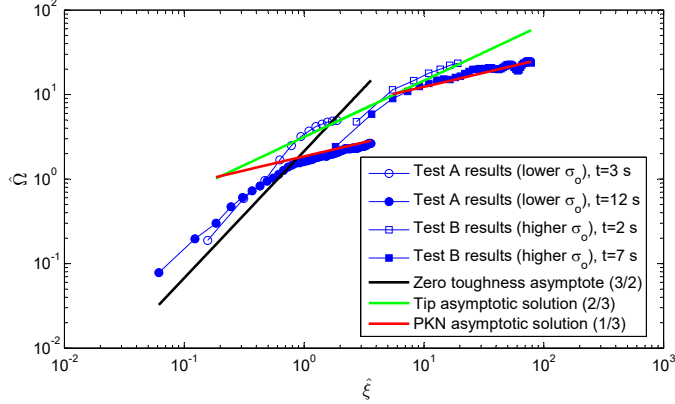


Figure 1.9: Comparison of experiment results with tip asymptotic solutions.

1.5.2 Comparison of experiments with global solutions

Besides the comparison with tip asymptotic solutions, we also compare the experimental results with global solution. Finally, during the PKN period of growth it is useful to examine opening profiles in the height (vertical) direction. These profiles allow examination for agreement with the PKN model as well as evidence for slippage of the interfaces at the top and bottom of the reservoir, which would result in non-zero opening at these boundaries. One representative comparison is shown in Fig. 1.10, taken at $t = 12$ s of Test A. By this time the HF attains PKN geometry and its vertical crack opening profile can thus be calculated using Eq. 1.19, where the measured inlet fluid pressure is $p = 0.95$ MPa. Fig. 1.10 shows the PKN model and the data are in good agreement. We can also see that the crack opening outside the reservoir layer is almost zero, which demonstrates there is no fluid leak off into the barriers. Finally, we observe no evidence of slip at the horizontal interfaces, but instead the opening smoothly approaches zero at the top and bottom of the reservoir layer in a manner consistent with the elliptical predicted opening.

The comparison of measured crack length with theoretical global solutions corresponding to Test A are described in Fig. 1.11. As it is shown, the measured crack length is very close to the global radial solution given by Eq. (1.5) during the radial portion of the growth, that is, when $l/H \leq 1$. As the length increases relative to the height, it approaches the global

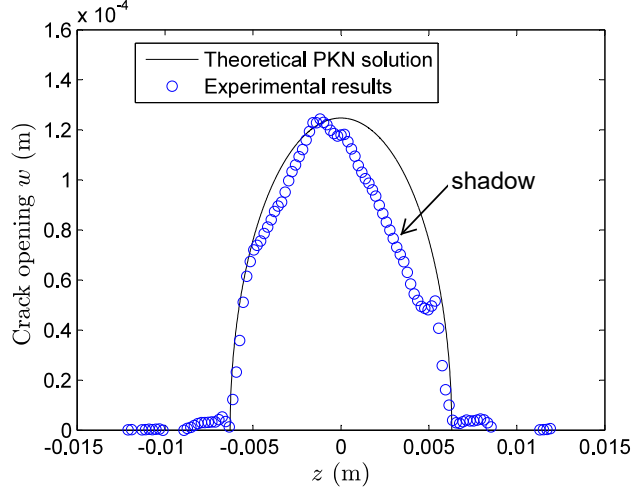


Figure 1.10: Experimental crack opening w along the height (z axis) at $x = 0$ and its comparison with PKN solution. Note some data is obscured by shadows in the image associated with the horizontal interfaces (see Fig. 1.6).

PKN solution from Eq. (1.6). The same conclusions can be obtained by scaling the crack length with the global solutions of radial and PKN models, as illustrated in Fig. 1.12. Here we see that the length follows the radial solution within about 10-20% for $l/H \leq 1$, and the PKN solution within about 10% for $l/H > 1$.

1.6 CHAPTER CONCLUSION

The tip behavior of HF is characterized by a rich nesting of asymptotic solutions, comprising a formidable challenge for the development of efficient and accurate numerical simulators. Although previously predicted by theory, several of these asymptotics had not been observed in experiments. In this context, the present paper presents experimental confirmation obtained through small-scale laboratory investigation wherein HF were created along zero-toughness interfaces within transparent specimens. The specimens were constructed and confining stress conditions were chosen so as to restrict the HF to a central layer within

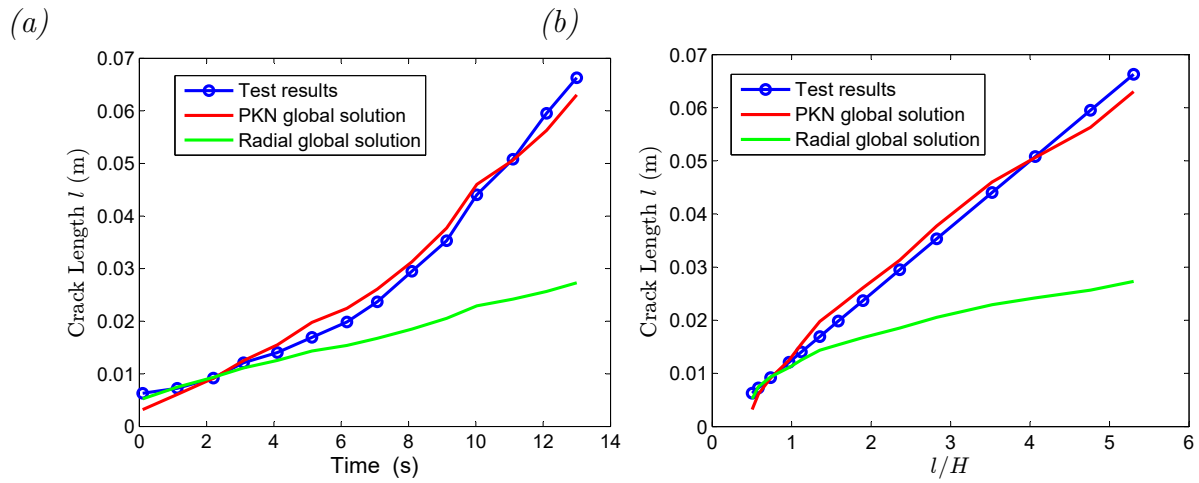


Figure 1.11: Measured crack length in Test A compared with radial and PKN global solution vs (a) Time and (b) Ratio of crack length over height l/H .

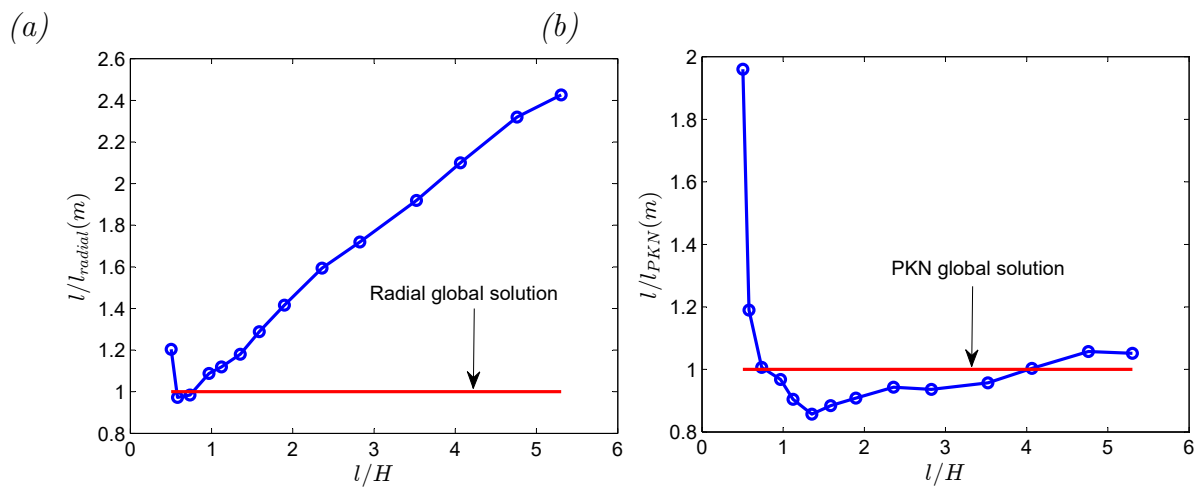


Figure 1.12: Measured crack length in Test A scaled by (a) Radial global solution and (b) PKN global solution vs ratio of crack length over height l/H

the specimen. Hence the experiments pertain to HF growth under conditions of negligible fracture toughness, with growth progressing from early-time radial geometry to large-time blade-like (PKN) geometry.

These experiments show strong agreement between the evolution of the crack length and the relevant global solutions. However, more to the point of the article, the crack opening in the tip region, measured using a photometric method, confirms:

- Existence of an asymptotic solution of the form $w \sim s^{3/2}$ (LEFM) in the region immediately adjacent to the tip,
- Transition to an asymptotic solution of the form $w \sim s^{2/3}$ away from the tip, with the transition length scale also consistent with theory,
- Transition to an asymptotic solution of the form $w \sim s^{1/3}$ after the fracture attains blade-like (PKN) geometry,
- Existence of a region near the tip of a blade-like (PKN) HF in which plane strain conditions persist, with the thickness of this region of the same order as the crack height.

Hence, the contribution of this paper is on the one hand illustrative, showing that the complex behavior of the tip region of HFs is an inescapable but experimentally-demonstrable phenomenon. However, more importantly, these results combine with prior experiments of [Bunger & Detournay \(2008\)](#) to comprehensively validate the theoretically-predicted tip structure for HFs propagating through an impermeable solid, driven by a Newtonian fluid under conditions of laminar flow, and when fracture growth is restricted by containing barrier layers.

2.0 LABORATORY DEMONSTRATION OF HYDRAULIC FRACTURE HEIGHT GROWTH ACROSS WEAK DISCONTINUITIES

2.1 PREAMBLE

The content of this chapter comprises a preprint of [Xing et al. \(In Press\)](#). It shows the first laboratory experiments clearly portraying reduction in height growth associated with the presence of weak discontinuities when considering also the influences of: 1) abrupt stress contrasts between layers, 2) material fracture toughness, and 3) contrasts of material properties between the reservoir and bounding layers. There are four observed geometries generated in the experiments: containment, height growth, T-shape growth and the combination of height growth and T-shape. The results indicate that these cases fall within distinct regions when plotted in a parametric space defined by horizontal confining stress and vertical confining stress, both normalized by the fluid pressure.

2.2 ABSTRACT

Decades of research have led to numerous insights for in modeling the impact of stresses and rock properties on hydraulic fracture height growth. However, the conditions under which weak horizontal interface are expected to impede height growth remains for the most part unknown. We presents an experimental study of the impact of weak horizontal discontinuities on hydraulic fracture height growth, including the influences of: 1) abrupt stress contrasts between layers, 2) material fracture toughness, and 3) contrasts of stiffness between the reservoir and bounding layers. The experiments are carried out with an analogue

three-layered medium constructed from transparent polyurethane, considering toughnesses resisting vertical fracture growth. There are four observed geometries: containment, height growth, T-shape growth and the combination of height growth and T-shape. Results are presented in a parametric space embodying the influence of the horizontal stress contrast, vertical stress, and horizontal barrier stress contrast, as well as the fluid pressure. The results indicate that these cases fall within distinct regions when plotted in the parametric space. The location in the parametric space of these regions are strongly impacted by the vertical fracture toughness, increasing the value of vertical interface fracture toughness leads to a suppression of height growth in favor of containment and T-shaped growth. Besides providing detailed experimental data for benchmarking 3D hydraulic fracture simulators, these experiments show that the fracture height is substantially less than would be predicted in the absence of the weak horizontal discontinuities.

2.3 INTRODUCTION

Hydraulic fracturing has been widely used for enhancing gas and oil recovery. Often the desire is for the hydraulic fractures to be confined in the reservoir layer, while in other cases the desire is to grow through barriers in order to connect production across multiple strata. In either case, accurate prediction of height growth is important for successful design.

Hydraulic fracture height growth is classically considered to be controlled mainly by the stress contrast between the reservoir and the bounding layers (Simonson et al. 1978, Warpinski & Teufel 1987, Nolte & Smith 1981, Economides & Nolte 2000). Laboratory experiments for planar, zero toughness hydraulic fractures illustrate the profound difference between height growth in the presence of a lower stress or higher stress in the bounding layers (Wu et al. 2008, Jeffrey & Bunger 2009). While the stress contrasts may determine the leading behaviour of the height growth, other parameters, such as interlayer contrasts in fracture toughness (Simonson et al. 1978), permeability (de Pater & Dong 2009), and stiffness (Van Eekelen 1982) can also influence height growth.

In addition to these better-studied factors, weak horizontal interfaces (bedding planes) above and/or below the reservoir can substantially limit height growth. On the one hand, the effect of weak horizontal interfaces on height growth has long been recognized through model predictions (Daneshy 1978), field observations (Warpinski & Teufel 1987), and in laboratory experiments (El Rabaa 1987, Teufel & Clark 1984). However, previous investigations have not systematically investigated the impact of the parameters controlling the behavior on hydraulic fracture height growth. Notably, previous investigations (Daneshy 1978, El Rabaa 1987, Teufel & Clark 1984) do not deal with the fracture growth inside the weak horizontal interfaces and/or they do not account for sharp stress contrasts among the layers (e.g. El Rabaa 1987). However, the consequences of the interplay between a growing hydraulic fracture, stress contrasts, and the weak horizontal interfaces have been directly observed in mined-out hydraulic fractures in coal seams; these clearly show both vertical and horizontal sections of fracture orientation (Diamond & Oylar 1987, Jeffrey et al. 1992).

Laboratory experiments demonstrate the impact of weak horizontal interfaces on hydraulic fracture containment. In particular, the focus is on the interplay among weak horizontal interfaces and the pre-existing stress state in determining hydraulic fracture growth. Thus, these experiments serve to clarify the role of these interfaces as they are reactivated by an impinging hydraulic fracture. Natural fracture reactivation by hydraulic fractures is a much broader topic with many past contributions (e.g. Warpinski & Teufel 1987, Renshaw & Pollard 1995, Blanton et al. 1986, Gu et al. 2012, Chuprakov et al. 2014) including recent modeling accounting for the role of fluid flow in promoting height growth across and interface (Abbas et al. 2014). Our goal is to provide experiments necessary to clarify the role of stresses, interface strength, and net pressure, as well as to give benchmarking results for future numerical simulations.

The experiments are carried out with an analogue layered medium constructed of transparent polyurethane (PU) which enables direct observation of the hydraulic fracture geometries in all directions. In addition to demonstrating combinations of parameters leading to containment, height growth and/or growth on the horizontal interfaces, these laboratory experimental results provide data for benchmarking hydraulic fracture simulators. After describing the experimental setup and method, the geometries and fluid pressure profiles

obtained in the experimental tests are presented to show the conditions leading to various height growth behaviors. Finally the experimental results are presented in a proposed parametric space which are defined by dimensionless groups depending on the confining stresses, fluid net pressure, and material fracture toughness.

2.4 EXPERIMENTAL METHODS

The experiments have been performed in transparent materials that enable real-time monitoring of the evolution of the hydraulic fracture geometry. The 152.4 mm cube-shaped specimens are composed of three layers, with each layer subdivided into two sub-blocks made of PU (see Figure 2.1). The analogue reservoir height was varied, with specimens using either a 50.8 mm, 25.4 mm, or a 12.7 mm analogue reservoir layer. In this way, the ratio of final half crack length L over reservoir height H_R varies from 1.5 to 6, which corresponds with compiled field mapping results showing that the half fracture length is often in the vicinity of five times the fracture height (de Pater 2015).

The fracture paths in the experiments are prescribed and the fracture can only propagate along the interfaces between different blocks. There are several benefits of using pre-defined artificial interfaces. Firstly, with artificial interfaces, the fracture toughness can be easily changed by using different adhesives. Secondly, the transparent material we used in the experiments has large tensile strength and fracture toughness, it will be difficult to fracture the blocks while it is much easier to initiate fracture in the artificial interfaces.

The loads were applied with hydraulic actuators using two axes of a true tri-axial loading frame. Transparent polymethyl methacrylate (PMMA) blocks were used to evenly spread the load from the smaller actuators to the PU specimens (Figure 2.1). There are two directions of loads applied, one in horizontal and one in vertical while the third direction is free. The applied horizontal loads are perpendicular to the fracture planes. Hence the horizontal confining stress in the experiments is analogous to the minimum horizontal in-situ stress. In order to generate the horizontal stress contrasts, the analogue reservoir layer and the bounding layers are made of PU materials with different Young's moduli. This modulus

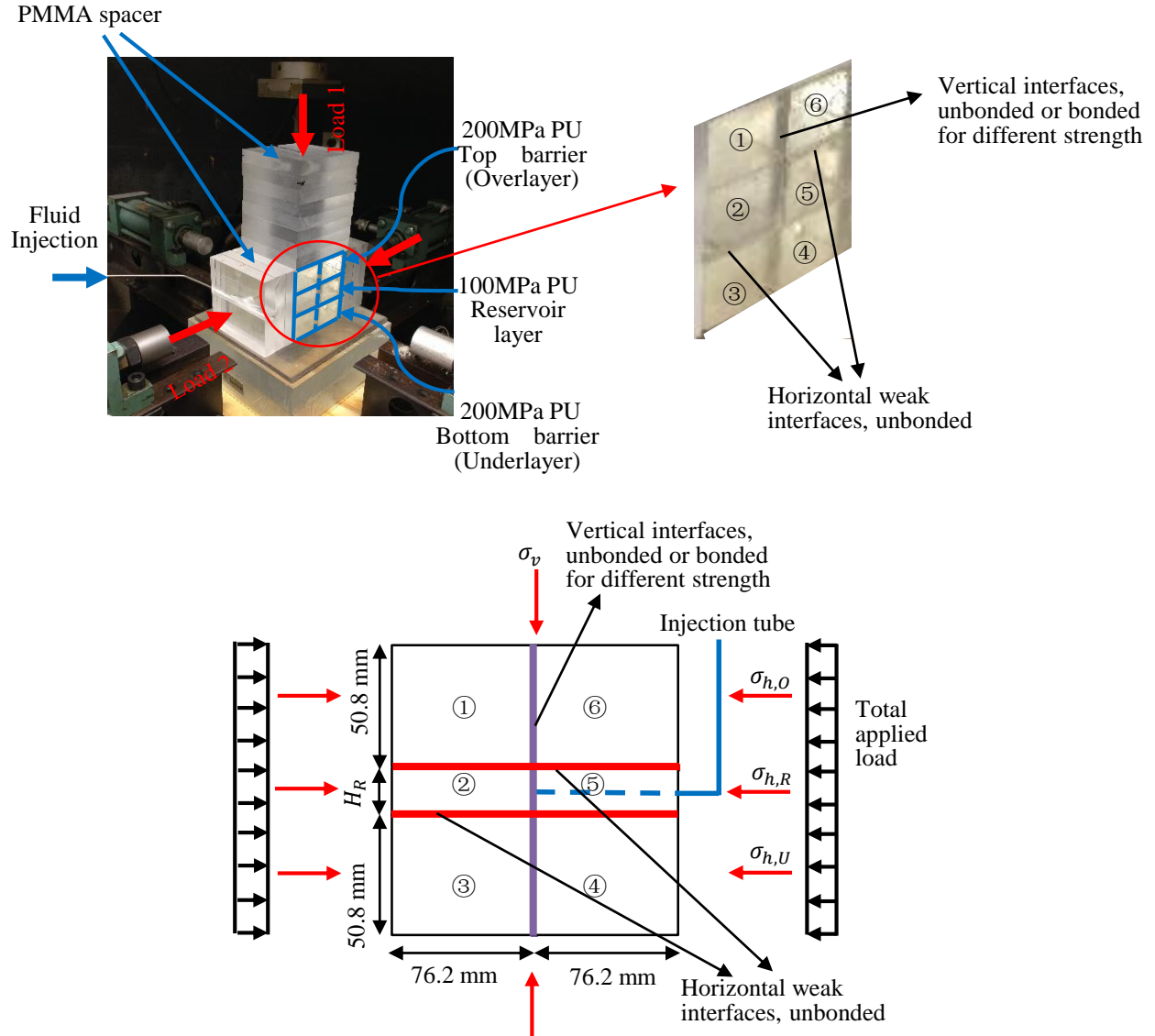


Figure 2.1: The experimental setup, shows the specimen composed of six sub-blocks. Sub-blocks 1 and 6 comprise the top barrier; sub-blocks 2 and 5 comprise the analogue reservoir layer; sub-blocks 3 and 4 comprise the bottom barrier. There are three different analogue reservoir heights H_R : 50.8 mm, 25.4 mm and 12.7 mm. The stresses $\sigma_{h,O}$ (horizontal overlayer confining stress), $\sigma_{h,R}$ (horizontal reservoir confining stress), $\sigma_{h,U}$ (horizontal underlayer confining stress) and σ_v (vertical confining stress) are generated by Load 2 and Load 1. Note that there are two directions of load applied (Load 2 and Load 1) and the other direction is free, however the crack growth orientation is restricted to the planes between the blocks so that the horizontal stress (Load 2) is analogous to the minimum stress.

contrast is obtained by using 2 different PU formulations provided as kits with differing design hardness by the manufacturer¹. The two components were mixed by a prescribed ratio and cast into a ground, polished aluminum mold to ensure the resulting blocks are flat, smooth and transparent. The mixed material was then cured at room temperature (20 °C) for 24 hours in the mold, after which the PU blocks were demolded and cured in an oven at 75 °C for another 16 hours, thereby achieving final material properties.

The load corresponds to a force generated by hydraulic actuators applied through rigid platens. Hence, the bounding condition is a uniform displacement. Subject to the constraint that the integral of the stresses generated at the specimen-platen contact is equal to the total applied force from the actuator. Upon application of the load, different horizontal confining stresses in each of the layers are therefore generated due to the contrasting elastic moduli. The confining stress in the barrier layers (top and bottom) was higher due to use of the PU with higher Young’s modulus ($E \approx 200$ MPa) compared to the analogue reservoir layer ($E \approx 100$ MPa). Although the stiffness is different for the analogue reservoir layer and barrier layers, the containing effect caused by the stiffness contrast is expected to be relatively weak (Van Eekelen 1982). Hence, in this study we focus on varying the stress contrast and vertical fracture toughness with fixed values of the elastic moduli of the layers. Note that quantifying the stress difference between the layers is non-trivial, especially in light of the relatively large Poisson’s ratio ($\nu \approx 0.48$). Hence, the stress contrasts are measured by a “squeeze out” test described in Appendix A. These tests quantify the ratio among the stresses in the layers, after which the different stress contrasts can be obtained by changing the magnitude of the total applied load.

In all the experiments, the interfaces between the analogue reservoir and adjacent layers (analogue horizontal bedding planes) were left unbonded to comprise the weak horizontal interfaces. The friction coefficient of the unbonded horizontal interfaces is found from symmetric direct shear tests (Hoskins et al. 1968) to be 0.20. In contrast, the strength was varied for the vertical interfaces (interfaces between 1-6, 2-5, and 3-4 in Figure 2.1), which provides the analogue for the strength of the reservoir and barrier rocks. We consider the limiting unbonded case and three bonded cases corresponding to different toughnesses, obtained by

¹WC756 (softer kits) and WC766 (stiffer kit) provided by BJB Enterprises were used.

using different adhesives. All adhesives are composed of double sided transparent tapes with a thickness approximately 0.1 mm. This method of adhering the blocks enabled precise location of the bonding, avoiding inadvertent bonding of the horizontal interfaces and allowing an unbonded region near the inlet and at the interface intersections. This unbonded region served as a starter notch for fracture growth. The three types of adhesives were Ve-ge carpet tape (“tape A” for short), Ve-ge carpet tape with surface treating agent Amodimethicone (“tape A reduced” for short), and Chica and Jo double sided tape with Amodimethicone (“tape B reduced” for short), where the surface treating agent Amodimethicone is used to reduce the strength of the tape. The fracture toughness of the interfaces bonded by the three adhesives was obtained by double notch tension tests (Appendix B). For preparing the specimens, in the bonded tests with double sided tape only (no surface treating agent), the sub-blocks were bonded by the tape directly and then the load was applied. In tests with double sided tape with surface treating agent, the surface treating agent was firstly sprayed onto the target interfaces and allowed to dry. After that, the treated sub-blocks were bonded by the tape, and then the load was applied.

After the loading, the fracturing fluid (glycerin mixed with food dye) was injected into the analogue reservoir layer through a 3.175 mm injection hole by a syringe pump. The viscosity of the fluid was 0.3 Pa·s at 20 °C. The hydraulic fracture initiated in the interface between sub-blocks 2 and 5 of the analogue reservoir layer (see Figure 2.1). A fluid pressure transducer was set in the injection line to record the fluid pressure near the borehole. Also, the pump rate, confining stresses, and fracture geometries were recorded during the whole procedure.

The experiments can be run in the viscosity-dominated regime (in which the toughness may be neglected), toughness-dominated regime (in which the viscosity may be neglected), or transition regime (in which both parameters are important) as defined by [Detournay \(2004\)](#). While a global definition of the propagation regime is possible for simple geometries, the propagation regime is most appropriately defined locally around the fracture front and depends on the front velocity ([Peirce & Detournay 2008](#)).

In order to define the propagation regime by tip region, a tip length scale l is introduced (Bunger & Detournay 2008, Garagash & Detournay 2000, Garagash 2009)

$$l = \frac{K'^6}{E'^4 \mu'^2 V^2}, \quad (2.1)$$

where V is the fracture tip velocity, $K' = \sqrt{32/\pi} K_{Ic}$ with fracture toughness K_{Ic} (in this case of the interface between the blocks), $\mu' = 12\mu$ with fluid viscosity μ , and $E' = E/(1 - \nu^2)$. The LEFM asymptote prevails in the tip region if $l/L \gtrsim 10^3$, while the viscous dissipation dominates if $l/L \lesssim 1$ by an accuracy of 10%, where L is the half length of the crack. Both the viscosity-dominated regime and toughness-dominated regime are obtained in the experiments. The unbonded cases are in the viscosity dominated regime ($l/L \cong 0$) and cases with vertical interfaces bonded by tape A are in toughness-dominated regime ($l/L \cong 2 \times 10^{10}$).

2.5 EXPERIMENTAL RESULTS

2.5.1 Observed behavior

The experiments result in four basic geometries: 1) containment, 2) height growth, 3) T-shape growth and 4) the combination of height growth and T-shape. Typical examples are shown in Figure 2.2. Here, Figure 2.2a shows a case of containment in which fracture growth is completely contained in the analogue reservoir layer. In contrast, Figure 2.2b shows an example of limited height growth, in which the fracture grows in height across the analogue reservoir layer boundary and into the bottom barrier which in this case has a lower stress than the upper barrier layer. Note the term “limited” is used here in contrast to uncontrolled height growth, for example in the case when the barrier layer has a lower stress than the reservoir layer (Wu et al. 2008). Figure 2.2c shows a case for which the fluid penetrates into the weak horizontal interface between sub-block 5 and sub-block 6 to form a T-shaped growth geometry. Figure 2.2d depicts a case of the combined limited height growth and T-shaped growth. In this case, the fracture not only forms a limited height growth profile

in the interface of sub-blocks 3 and 4, but also forms a T-shape by penetrating the weak horizontal interface between sub-blocks 5 and 6.

Figure 2.3 shows a pressure record for two typical cases with limited height growth under zero toughness. We observe a substantial contrast between the two cases. In the first case, the peak pressure exceeds the treating pressure (defined as the pressure when the fracture propagates steadily after breakdown) by nearly a factor of ten (see solid curve in Figure 2.3). In the second case, we modified the inlet by milling a 2 mm deep and 10 mm diameter notch. In this way, a point-like source was essentially replaced with a finite sized source, thus reducing the near wellbore fluid pressure gradient. With this modification, the experiment has a similar treating pressure but much lower peak pressure (dashed curve in Figure 2.3). We found the use of a notch improved experimental control, repeatability, and ability to measure the net treating pressure. So, with the exception of a few experiments in the 50.8 mm analogue reservoir, all experiments use an initial notch. In finite toughness cases, similar initiation was also enabled by removing the corresponding part of the double sided tape in the area of original notch. Also, with this modification, we observe a pressure increase immediately after crack initiation, as shown in the dashed curve in Figure 2.3, where it is clear that the peak pressure occurs after initiation. Compressibility of the injection system leading to fluid storage prior to crack initiation may cause a separation between crack initiation and peak pressure, as previously predicted by numerical simulations (see e.g. [Bunger et al. 2010](#), [Lakirouhani et al. 2016](#)), observed in laboratory experiments (see e.g. [Lecampion et al. 2015](#), [Bunger et al. 2013](#)), and shown to be more pronounced for viscosity dominated cases ([Lakirouhani et al. 2016](#)).

Figure 2.4 shows typical inlet pressure records corresponding to the other three basic geometries (containment, T-shape, limited height growth and T-shape). In the containment case (Figure 2.4a), the inlet pressure continues to increase after crack initiation until the fracture reaches the boundary (End of Test-EOT). This continuous increase is consistent with the classical PKN model for a perfectly contained, blade-shaped hydraulic fracture ([Perkins & Kern 1961](#), [Nordgren 1972](#)), wherein the pressure is predicted to grow with time. We would have also expected an early period of time where the pressure was decreasing as the fracture grew radially ([Savitski & Detournay 2002](#)). Such an interpretation follows the

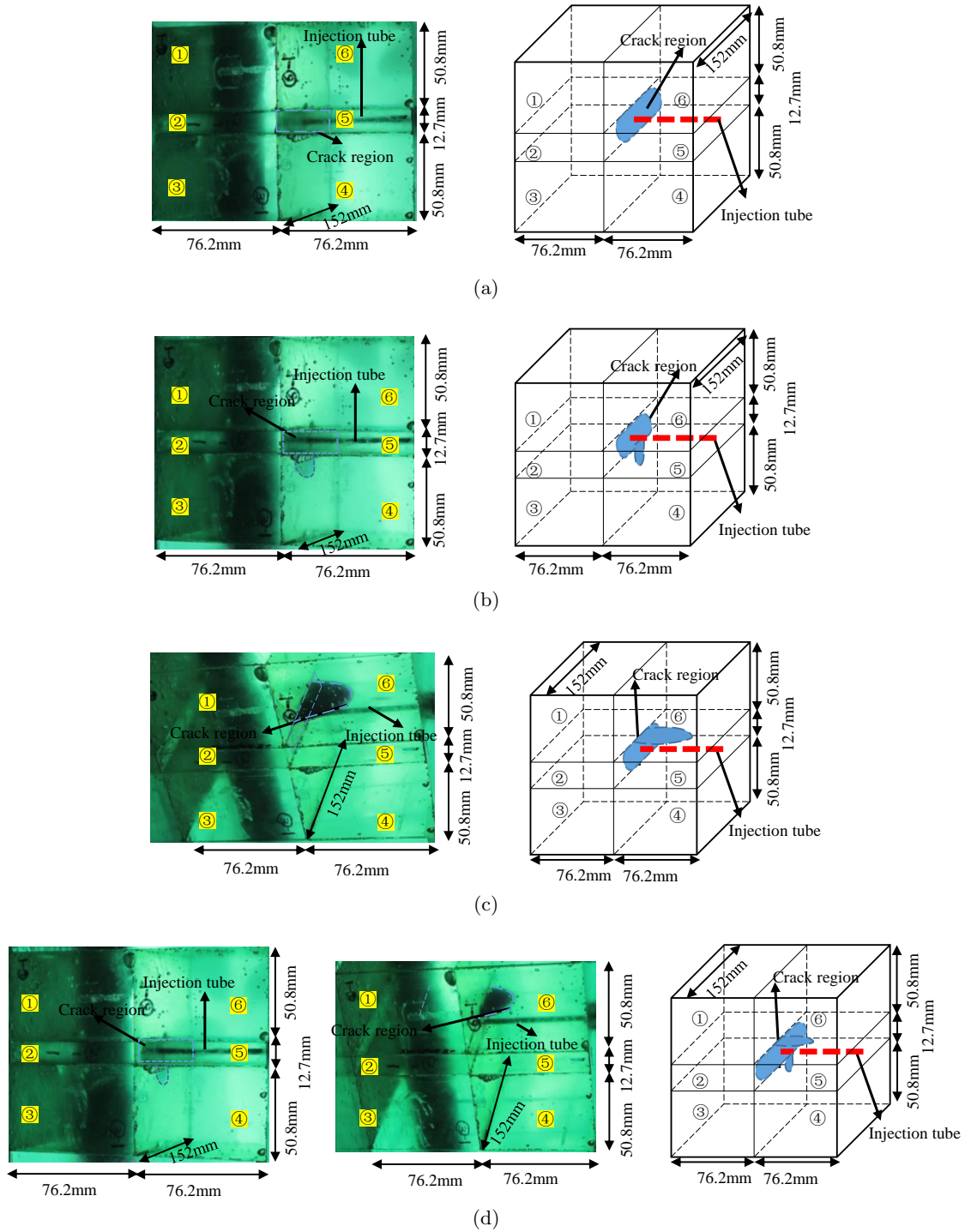


Figure 2.2: Typical fracture propagation for the four cases in the bonded tests: (a) Fracture containment, (b) Limited height growth, (c) T-shape, (d) Limited height growth and T-shape (there are two directions of views required for complete observation). The crack region is outlined by blue lines. Sub-blocks 1 and 6 comprise the top barrier; 2 and 5 comprise the analogue reservoir layer; 3 and 4 comprise the bottom barrier.

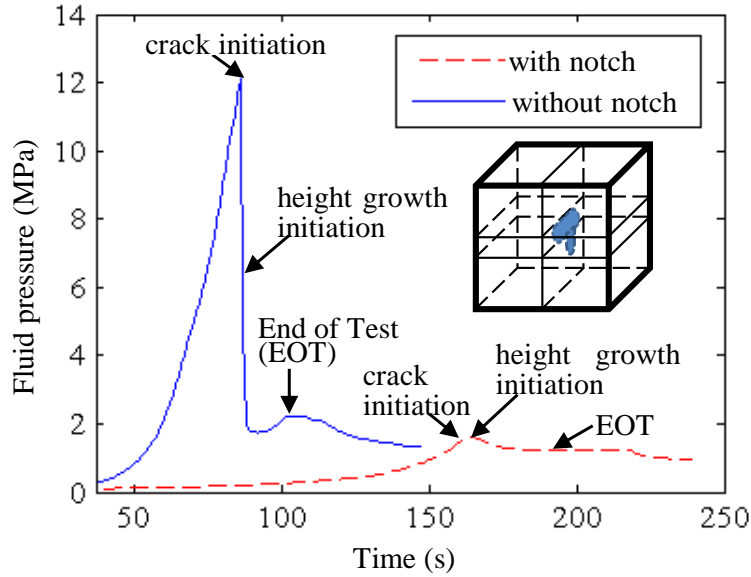


Figure 2.3: Pressure evolution for cases with and without notches. The blue solid line shows a typical 50.8 mm analogue reservoir test without a notch ($\sigma_v = 0.94$ MPa, $\sigma_{h,B} = 0.39$ MPa, $\sigma_{h,R} = 0.16$ MPa). The red dashed line shows a typical 12.7 mm analogue reservoir test with notch ($\sigma_v = 0.99$ MPa, $\sigma_{h,B} = 0.55$ MPa, $\sigma_{h,R} = 0.23$ MPa). Here End of Test (EOT) is designated when the fracture reaches the specimen boundary. The inset describes the geometry of limited height growth.

discussion of [Nolte & Smith \(1981\)](#). Note it is likely the observed early portion of pressure increase rather than the predicted decline is due to compressibility of injection system (see e.g. [Lakirouhani et al. 2016](#)). In spite of the this minor inconsistency between the early behavior of the pressure with the radial model, the growth of the fracture height in these experiments shows remarkable consistency firstly with the radial model and eventually with the PKN model (see Appendix C).

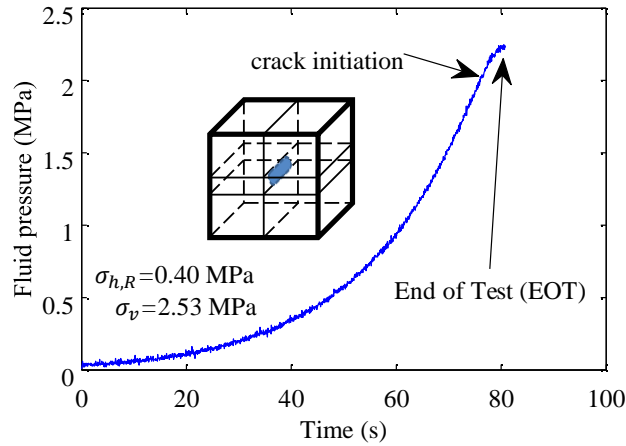
In the T-shape growth case (Figure 2.4b), similar to the limited height growth case, the inlet pressure continues to increase after crack initiation until the fluid penetrates into the interface between the analogue reservoir layer and bounding layer (T-shape growth initiation). Then the inlet pressure starts to decrease with the propagation of the fracture, both in the analogue reservoir layer and the weak horizontal interface. In the case of the combination of limited height growth and T-shape (Figure 2.4c), the inlet pressure firstly increases after crack initiation until the hydraulic fracture propagates into the barrier layer (height growth initiation). Then, after the fluid pressure decreases to a certain point the fluid penetrates into the interface between the analogue reservoir layer and bounding layer (T-shape growth initiation). After that, the fracture continues to grow in the analogue reservoir layer, the bounding layer, and the weak horizontal interface while the fluid pressure continues to decrease.

2.5.2 Parametric space

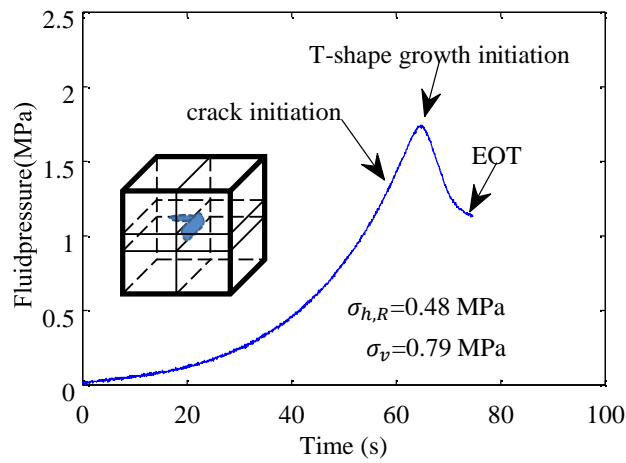
We observe the four geometries (Figure 2.2) resulting from different combinations of confining stresses, vertical interface toughness, and net treating pressure. In order to clarify the influence of these quantities, two dimensionless parameters \mathcal{H}_b (after [Simonson et al. 1978](#)) and \mathcal{H}_v (bearing some similarity to a stress measure used by [Renshaw & Pollard 1995](#)) are given by

$$\begin{aligned}\mathcal{H}_b &= \frac{\sigma_{h,B} - \sigma_{h,R}}{p_{net}} \\ \mathcal{H}_v &= \frac{\sigma_v - \sigma_{h,B}}{p_{net}},\end{aligned}\tag{2.2}$$

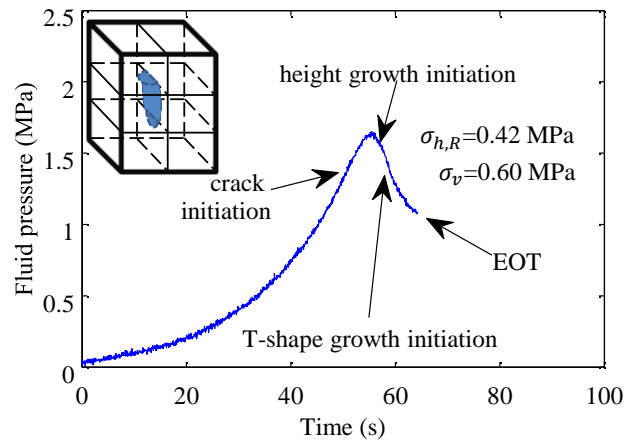
where p_{net} is the net fluid pressure at the wellbore, taken as a difference between the fluid pressure p and the reservoir horizontal (effective) confining stress $\sigma_{h,R}$, σ_v is the vertical



(a)



(b)



(c)

Figure 2.4: Pressure record for bonded tests (medium toughness) with a notch corresponding to: (a) Fracture containment, (b) T-shape, and (c) Limited height growth and T-shape. The inset in each subfigure describes the corresponding fracture geometry. Note limited height growth is shown in Figure 2.3.

(effective) confining stress, and $\sigma_{h,B}$ is the horizontal barrier (effective) confining stress (the smaller one of $\sigma_{h,O}$ and $\sigma_{h,U}$, recalling that $\sigma_{h,O}$ and $\sigma_{h,U}$ are the minimum horizontal stresses in the over and under-layer, respectively). Note that in the experiments both p_{net} and the fracture heights are measured at the moment when the fracture half-length reaches the half-length of the block (EOT).

These two parameters embody comparisons of net pressure with the horizontal stress contrast between the barrier and reservoir, and the stress contrast between the vertical stress acting on horizontal bedding plane and horizontal stress in the barrier, respectively. Hence, when $\mathcal{H}_b \rightarrow 0$, the stress jump to the barrier layer(s) vanishes and the height growth is expected to be unbounded according to the classical equilibrium height growth model (Simonson et al. 1978). In contrast, for large \mathcal{H}_b , the fracture growth is expected to be restricted to the reservoir and/or horizontal bedding planes. On the other hand, whether fracture growth occurs on the horizontal bedding plane is proposed to be embodied mainly by \mathcal{H}_v ; smaller values of \mathcal{H}_v correspond to cases with relatively smaller vertical stresses which are more likely to promote growth along the weak horizontal interfaces. In the experiments, $0 < \mathcal{H}_b < 1.1$ and $-1.5 < \mathcal{H}_v < 2.0$. In the field, typically, the net fluid pressure is around 5 – 10 MPa, $\sigma_{h,B} - \sigma_{h,R}$ is 0 – 20 MPa, and $\sigma_v - \sigma_{h,B}$ is about -40 – 60 MPa (Brown & Hoek 1978). Hence, in the field, the approximate range of \mathcal{H}_b and \mathcal{H}_v are 0 – 4 and -8 – 12, respectively.

For the parameters \mathcal{H}_b and \mathcal{H}_v , we consider the influence of confining stress and fluid pressure, but we still need another parameter incorporating the impact of vertical interface fracture toughness. Hence, a dimensionless fracture toughness parameter is defined as

$$\kappa_T^{-1} = \frac{(\sigma_v - \sigma_{h,B})\sqrt{H_R}}{K_{Ic}}. \quad (2.3)$$

This parameter represents the ratio between the stress increase associated with growth on the horizontal interface rather than into the barrier layer ($\sigma_v - \sigma_{h,B}$) and a measure of the fracture-induced stress $K_{Ic}/\sqrt{H_R}$ (e.g. Simonson et al. 1978), recalling that K_{Ic} is the same for the vertical interfaces in all three layers while the horizontal interfaces are unbonded in all cases. The parameter κ_T is therefore a dimensionless toughness, and here we will deal with an inverse toughness κ_T^{-1} because it avoids having an infinite value when the

Table 2.1: κ_T^{-1} in field and experiments with different adhesives in vertical interfaces

Parameters	Field	Tape A	Tape B reduced	Tape A reduced	Unbonded
$\sigma_v - \sigma_{h,B}$ (MPa)	-40 – 60*	0.50 – 1.80	-0.60 – 1.60	-1.00 – 1.30	-2.74 – 0.70
H_R (m)	25 – 100	0.0127	0.0127	0.0127	0.0127
K_{Ic} (MPa.m ^{1/2})	0.5 – 2.0	0.40	0.069	0.026	0
κ_T^{-1}	-250.0 – 400.0	0.1 – 0.5	-1.0 – 2.6	-4.3 – 5.6	$-\infty - +\infty$

* Obtained from [Brown & Hoek \(1978\)](#)

vertical stress and barrier stress are equal. Practically, κ_T^{-1} relates firstly to the T-shape growth propensity, due to the competition with the difference between vertical and barrier horizontal confining stress and the fracture toughness of the reservoir. It also relates to the impact of the horizontal interface on mitigating height growth; presumably a relatively stronger vertical interface toughness corresponding to small κ_T^{-1} will lead to a larger impact of the weak horizontal interface.

This dimensionless parameter κ_T^{-1} also enables us to compare the experimental results with conditions of typical values expected in the field. These are shown in Table 2.1 and are also depicted as a function of depth in Figure 2.5. The lower bound of κ_T^{-1} represents the tests expected to be prone to T-shape growth while the upper bound represents those prone to containment.

From Table 2.1 and Figure 2.5, we can see that the tests with unbonded vertical interface and tape A reduced vertical interface have the largest range of κ_T^{-1} corresponding to almost any depth of reservoir (0 – 3500 m). The tests with tape B reduced and tape A have smaller range of κ_T^{-1} and also corresponds to a range of the reservoir depths from shallow to deep. Furthermore, we will show that the lab range κ_T^{-1} is sufficient to observe transition from negligible toughness (results are nearly identical to zero toughness cases) to large enough toughness to completely suppress height growth.

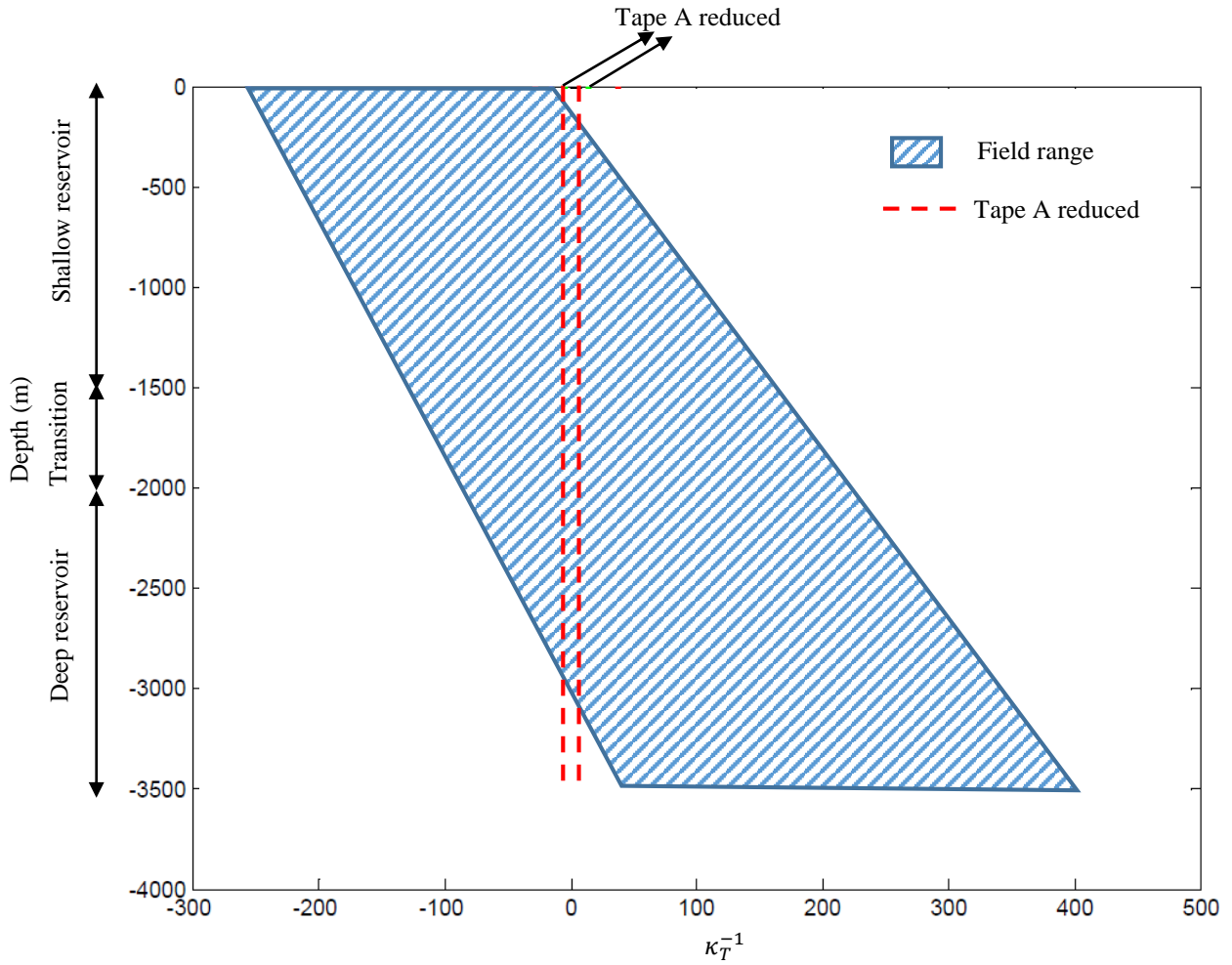


Figure 2.5: Range of κ_T^{-1} in field and Tape A reduced, also refer to Table 2.1. Note the field reservoirs typically can be classified as: shallow reservoir (500 – 1500 m), transient part (1500 – 2000 m), deep reservoir (2000 – 3500 m). Following Brown & Hoek (1978), the vertical stress of the field σ_v is calculated as $0.027h_z$, and upper and lower bound of field $\sigma_{h,B}$ are $0.0135h_z + 40.5$ and $0.0081h_z + 2.7$ respectively, where h_z is the depth (depth h_z unit is m and stress unit is MPa).

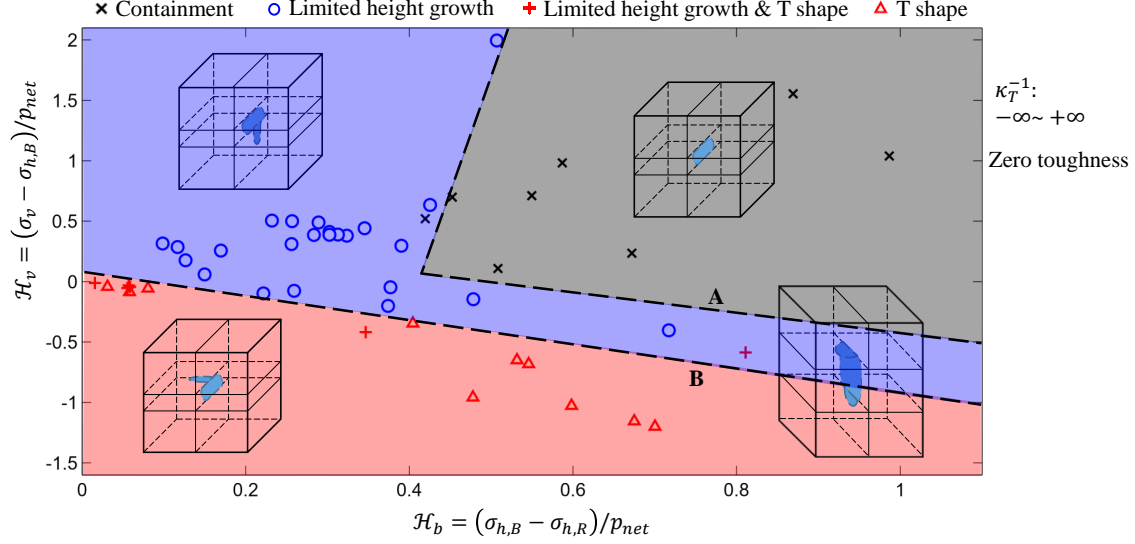


Figure 2.6: Results of the tests with unbonded vertical interfaces (zero toughness $K_{Ic} = 0$) in the proposed parametric space. Curve A and Curve B are hand drawn. The insets describe the fracture geometries.

2.5.3 Experimental results in the proposed parametric space

The results of tests with unbonded (zero toughness) vertical interface and bonded (finite toughness) vertical interface are plotted in the \mathcal{H}_b and \mathcal{H}_v parametric space in Figures 2.6 and 2.7, recalling that the horizontal interface is always unbonded. Each test corresponds to one point in these plots. The shape of the symbols is determined by which of the four geometries (Figure 2.2) are realized in each experiment at the time the hydraulic fracture just reaches the specimen boundary (EOT). The boundaries that separate different geometries in the parametric space are hand drawn and empirically determined based on the experimental results.

Figure 2.6 shows the unbonded tests (zero toughness). Here the curve A separates the cases of containment and limited height growth. It shows that containment is promoted by: 1) larger horizontal confining stress difference relative to the net pressure and 2) larger difference between vertical stress and horizontal barrier stress relative to the net pressure.

This influence of the vertical stress on the containment to height growth transition provides evidence for the impact of the weak horizontal interface. In the region below the curve B, the cases of T-shape are observed. The value of the maximum vertical load that enables the T-shape fracture propagation decreases with the increase of the relative horizontal stress difference. In between the limited height growth case and T-shape case (near the curve B) is a region with combined limited height growth and T-shape. We note this region is narrow and, while suggested by a few results, it is not distinctly defined based on our experiments.

The zero toughness cases establish a baseline from which the influence of finite toughness can be observed. Moving on to finite toughness cases, Figure 2.7a shows the results with the smallest fracture toughness ($K_{Ic}=0.026\text{MPa} \cdot \text{m}^{\frac{1}{2}}$). This is reflected in the inverse dimensionless toughness $\kappa_T^{-1} = -4.3 \sim 5.6$ for the vertical interfaces, recalling we always maintain zero toughness for the horizontal interfaces (see Table 2.1 and Figure 2.5). All four basic geometries are obtained in this series of tests. It can be found that the fracture propagation will change from limited height growth to containment as \mathcal{H}_b increases and from T-shape growth to containment as \mathcal{H}_v increases. In addition, there is one case exhibiting combination height growth and T-shape thus representing a transition region.

The effects of further increasing the toughness are evidenced in the data presented in Figure 2.7b, which correspond to the tests with tape B reduced. These have an intermediate fracture toughness $K_{Ic}=0.069 \text{MPa} \cdot \text{m}^{\frac{1}{2}}$. This is reflected in the dimensionless toughness $\kappa_T^{-1} = -1.0 \sim 2.6$ for the vertical interfaces (see Table 2.1 and Figure 2.5). All four basic geometries are again obtained in this series of tests. We observe that by increasing \mathcal{H}_b , the fracture propagation will change from limited height growth to containment cases. As expected, the T-shape cases are distributed in the lower part of the parametric space, corresponding to a small \mathcal{H}_v . The combination cases occupy a narrow intermediate region among the other three cases. Additionally it is interesting to observe that at $\mathcal{H}_b \sim 0.47$, which is a relatively large horizontal stress difference in the context of this series of experiments, there exists a limited height growth case even though \mathcal{H}_v is small enough one that one might have instead expected T-shaped growth.

Finally, the strongest interface experiments (tape A $K_{Ic}=0.40 \text{MPa} \cdot \text{m}^{\frac{1}{2}}$) are presented in Figure 2.7c. The dimensionless toughness for the vertical interfaces are in the range

$\kappa_T^{-1} = 0.1 \sim 0.5$ (see Table 2.1 and Figure 2.5). There are only containment and T-shape cases; no limited height growth or combination cases were obtained in the tests with highest toughness. We believe the reason is that the larger fracture toughness requires higher fluid pressure to form the crack in the analogue reservoir layer. The higher fluid pressure will in turn promote penetration into the weak horizontal interfaces (e.g. the unbonded interface between sub-block 5 and 6). Also, and perhaps even more importantly, the toughness on the vertical interface in the barrier layer is apparently high enough that it is advantageous to grow in the T-shape geometry. Hence, T-shape cases most frequently occur in this series of tests. This is not to say height growth is impossible with this interface toughnesses. In principle, in order to suppress the T-shape growth in the weak horizontal interfaces to obtain other shapes, the load in vertical load needs to be increased to obtain larger σ_v . However, in our setup, due to large Poisson's ratio of the PU material, the horizontal stress $\sigma_{h,B}$ and $\sigma_{h,R}$ will be substantially increased at the same time, which will result a larger stress difference in the horizontal direction and serve to again suppress height growth. So, for our configuration we are restricted to showing how the fracture propagation will change from T-shape growth to containment as the dimensionless vertical stress contrast, \mathcal{H}_v , increases.

By comparing the data under four different vertical interface toughnesses, we find that the tests under zero toughness were able to cover the largest span in the \mathcal{H}_b and \mathcal{H}_v parametric space, while tests with the highest toughness have the smallest span. The reason is that under the same confining stress, the tests with larger fracture toughness generate higher fluid pressure p_{net} , which results in smaller variation of the dimensionless parameters \mathcal{H}_b and \mathcal{H}_v for a fixed range of experimentally attainable stress contrasts, $\sigma_v - \sigma_{h,B}$ and $\sigma_{h,B} - \sigma_{h,R}$. Also, as we can see in the parametric spaces, even with a smaller range of \mathcal{H}_b and \mathcal{H}_v in the experiments than in the field, we can still find the boundaries of different geometries in the parametric spaces. However, because of the difference in scale, caution must be used in applying results directly to the field. A more suitable approach is probably to benchmark a numerical simulator to the experiments, and then to use the simulator to make field-scale predictions.

We observe, then, that increasing the vertical interface toughness leads to a suppression of height growth in favor of containment and T-shaped growth. This is evidenced by: (1)

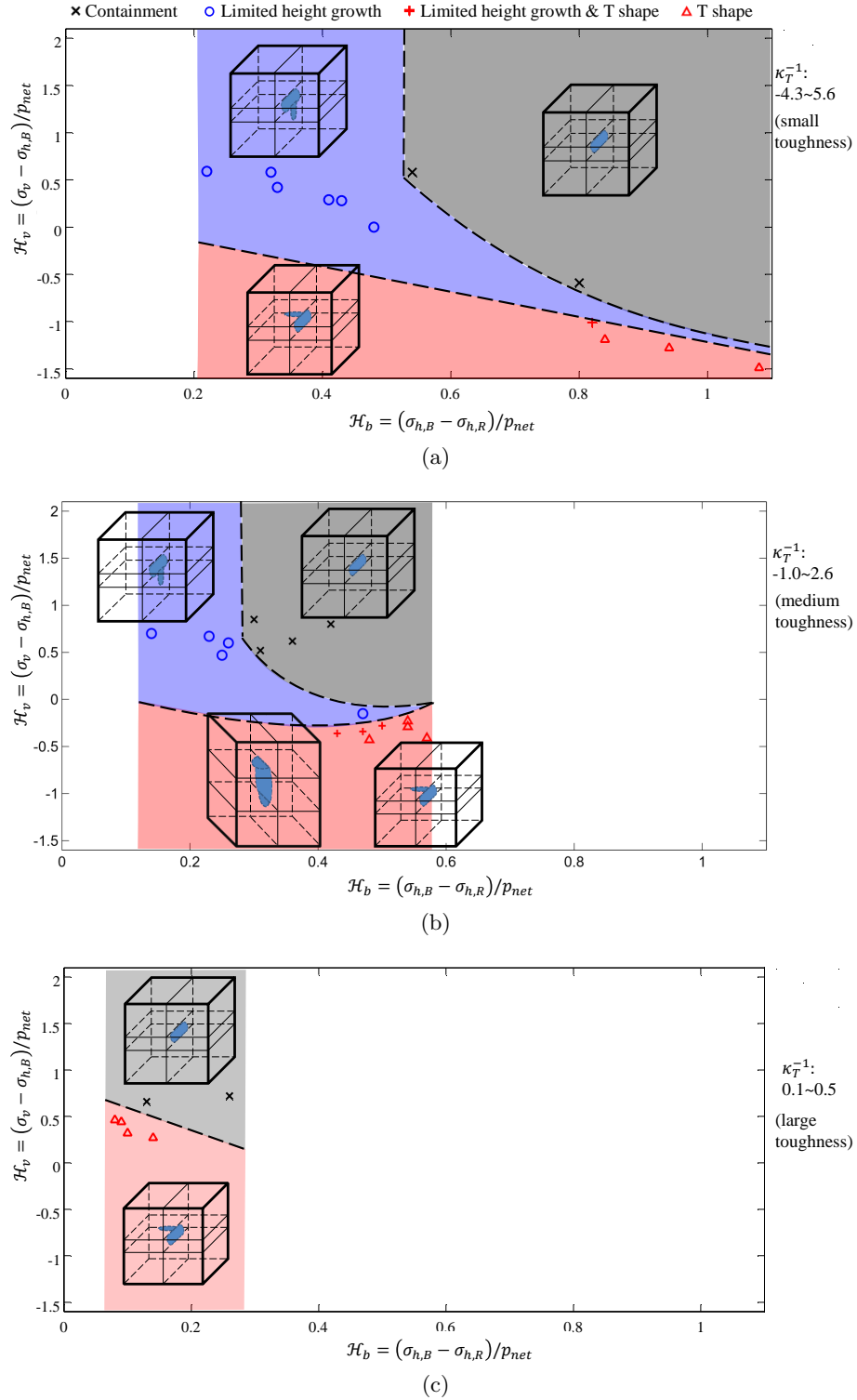


Figure 2.7: Results of the tests with bonded vertical interfaces in the parametric space: (a) with tape A $K_{Ic} = 0.40 \text{ MPa}\cdot\text{m}^{\frac{1}{2}}$, (b) with tape B reduced $K_{Ic} = 0.069 \text{ MPa}\cdot\text{m}^{\frac{1}{2}}$, (c) with tape A reduced $K_{Ic} = 0.026 \text{ MPa}\cdot\text{m}^{\frac{1}{2}}$. The region of different geometries are separated by the hand drawn lines. The insets describe the fracture geometries.

Complete suppression of height growth for the strongest interface, (2) Containment at lower values of \mathcal{H}_b when vertical fracture toughness K_{Ic} increases, (3) Expanded regions corresponding to T-shape for larger values of vertical interface fracture toughness, in particular are the increase in the value of the vertical stress as it impacts on \mathcal{H}_v required to suppress T-shape growth.

We reiterate that the present scope of research focuses on the impact of weak horizontal interfaces and stress contrasts on HF containment. To this regard, we have limited consideration to unbonded horizontal interfaces while varying the strength of the vertical interfaces. A useful extension will include varying the strength of bonded horizontal interfaces. We also note that the parametric space does not explicitly include dependence upon fluid parameters such as injection rate and fluid viscosity. However, these parameters do impact the result because they impact the net pressure, which does appear in the proposed parametric space. Hence, it is possible in principle to substitute a characteristic pressure valid for a given limiting regime (i.e. toughness or viscosity dominated, after [Detournay 2004](#)) to obtain explicit dependence upon such parameters. However, this is also not to say that injection parameters will not impact the geometry through other mechanism(s) not captured through the scaling of the stress contrasts by the net pressure. Hence, another useful line of research will aim at validating the proposed parametric space with systematically-varying injection parameters.

2.5.4 Hydraulic fracture height

Generally, the hydraulic fracture can cross one interface to the top or bottom barrier layer, or it can propagate into both the upper and lower barrier layers. Under zero toughness, the classical equilibrium height growth model ([Simonson et al. 1978](#)) predicts, for the case of symmetric height growth, that

$$\frac{H_f}{H_R} = \frac{1}{\sin\left[\frac{\pi}{2}\left(1 - \frac{1}{\mathcal{H}_b}\right)\right]}, \quad \mathcal{H}_b > 1, \quad (2.4)$$

where H_f is the overall fracture height. Similarly, for the case of asymmetric height growth, this approach leads to

$$\frac{H_f}{H_R} = \frac{2}{1 - \sin\left[\frac{\pi}{2}\left(\frac{2}{\mathcal{H}_b} - 1\right)\right]}, \quad \mathcal{H}_b > 1. \quad (2.5)$$

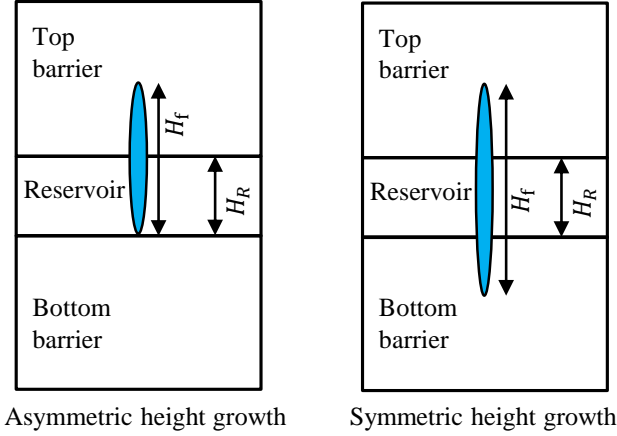


Figure 2.8: Two types of hydraulic fracture height growth in a layered medium (cross section view). Here H_R is the reservoir height and H_f is the overall fracture height.

In our experiments, the horizontal confining stresses in the top barrier layer and bottom barrier layer are not the same. Hence, most of the limited height growth cases are asymmetric, as shown in Figure 2.8. For the experiments with zero toughness (see Figure 2.6), the approximate minimum \mathcal{H}_b for containment cases is about 0.45, which means the fracture could be contained even if the net wellbore fluid pressure is greater than the horizontal stress difference between the reservoir and barriers. According to Equations 2.4 and 2.5, when \mathcal{H}_b tends to 1, the total fracture height H_f tends to infinity and the fracture propagation into the barrier(s) should be uncontrolled. This is not the case in our experiments. The experiments with weak horizontal interfaces are therefore observed to have much smaller height growth compared to the prediction from the classical equilibrium height growth model.

Of course the experiments deviate from the idealization of the equilibrium height growth model in several important ways; the point here is to observe how much of a difference these deviations make to the observed geometry. One obvious difference is the presence of the weak interface, which likely impacts transmission of the necessary stresses and/or fluid pressure to open the interface in the barrier layer. Another possible contributing reason is that Equations 2.4 and 2.5 assume that the fluid pressure in the vertical fracture cross-section is uniform. But this is probably not true in the tests; the wellbore pressure almost certainly

exceeds the pressure at the interface. Thirdly, Equations 2.4 and 2.5 also assume the same elastic properties for all layers, whereas in our case the analogue reservoir is of lower stiffness than the barrier.

To further examine the extent of height growth, Figure 2.9 shows the experimental dependence of the relative height growth H_f/H_R on \mathcal{H}_b . These measurements are compared with the asymmetric equilibrium height growth solution (Equation 2.5). The experimental result of Jeffrey & Bungler (2009), in which there was a stress jump between the analogue reservoir and barrier, but no weak horizontal interfaces, is also presented. We observe that the experimental values of H_f/H_R decrease with the increase of \mathcal{H}_b as expected. While there is some variability, the experimental results nevertheless form a band which is bounded above and below by two proposed curves. Interestingly, the upper and lower bounds described by power-law fitted equations $H_f/H_R = 0.96\mathcal{H}_b^{-1.348}$ and $H_f/H_R = 13.96 - 14.07\mathcal{H}_b^{0.091}$ respectively, have the same shape of a shifted Equation 2.5. We also observe the experimental values of H_f/H_R considering the presence of weak horizontal interfaces are much smaller than that predicted by equilibrium height growth solution and are also smaller than the results of Jeffrey & Bungler (2009). While the difference from the equilibrium height growth solution can have a number of explanations, suggested above, the main difference compared with the experiment of Jeffrey & Bungler (2009), is the presence of the weak horizontal interface. Hence a likely explanation of the much smaller height growth in the present experiments is that it is impeded by the weak horizontal interface.

2.6 CONCLUSIONS

A series of experiments have been carried out in transparent three-layer rock analogue models to explore the influence of horizontal confining stress, vertical confining stress, material fracture toughness and the weak horizontal interfaces between the reservoir and barrier layers on the fracture containment. The tests also provide the data for benchmarking hydraulic fracture simulators.

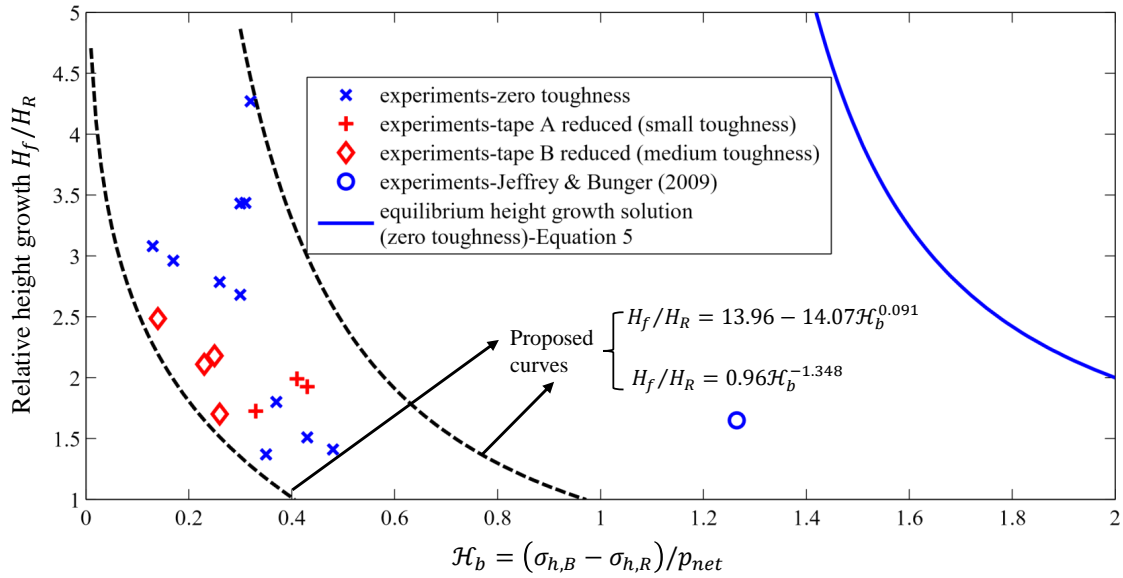


Figure 2.9: Comparison of experimental results of relative height growth H_f/H_R vs \mathcal{H}_b with equilibrium height growth solution. Note that all the data presented here are asymmetric height growth with the analogue reservoir height 12.7 mm and the maximum fracture length over reservoir height ratio is 6. For the Jeffrey and Bungler (2009) experimental result, the maximum fracture length over reservoir height ratio is 3.

The results show four distinct geometries:

- (1) Complete fracture containment corresponding to low enough net pressure when compared to the stress contrasts between the reservoir and the barrier(s) and/or between the barrier and the vertical stress acting on the weak horizontal interfaces.
- (2) T-shaped growth occurs when the difference between the vertical stress and the barrier stress is small enough. For the bonded tests, we have used a dimensionless fracture toughness parameter κ_T^{-1} , allowing the comparison of the experimental parameters with those relevant in field. T-shape growth is found to be more likely to be obtained during the tests with the largest toughness (smallest κ_T^{-1}).
- (3) Limited height growth comprised of vertical growth into the barrier layers occurs when the stress contrast between the reservoir and barrier layers is small enough relative to the net pressure and the vertical stress is large enough with respect to the barrier stress. For net fluid pressure greater than the horizontal stress contrast, our experiments exhibit limited, stable height growth while the classical equilibrium height growth model predicts uncontrolled height growth. The relative fracture height in our experiments is thus smaller than predicted by the equilibrium height growth solution. The experiments quantitatively confirm the known and often observed fact that discontinuities impede hydraulic fracture growth generally and hydraulic fracture height growth specifically. Also, the experiments show that the relative fracture height decreases as the relative horizontal stress difference increases.
- (4) A transition region of combination cases is found between limited height growth case and T-shaped growth case in both bonded and unbonded tests.

All the results of the same vertical interface toughness can be grouped together in a proposed parametric space (\mathcal{H}_b and \mathcal{H}_v) defined by the confining stresses and fluid pressure. The tests with a zero toughness vertical interface have the largest span in the parametric space due to their smaller net fluid pressure compared to the tests with finite toughness. Comparing the three groups of bonded tests, we find that with the increase of the vertical interface fracture toughness, the region formed by tests characterized by the same fracture toughness moves to upper-left corner in the parametric space. Also, increasing the value of vertical interface

toughness associated with height growth leads, to a suppression of height growth in favor of containment and T-shaped growth.

In this study, we investigate the effect of weak horizontal interface on the hydraulic fracture height. In the future investigations, fracture toughness can be introduced to the horizontal interface. In addition, the impact of varying the fluid parameters such as injection rate and fluid viscosity are important topics for future research.

3.0 LATTICE SIMULATION OF HYDRAULIC FRACTURE CONTAINMENT IN LAYERED RESERVOIRS

3.1 PREAMBLE

The content of this chapter comprises a preprint of [Xing et al. \(In Preparation\)](#). It presents a numerical study of hydraulic fracture containment in layered reservoirs using a distinct element model (DEM) that couples fluid flow with a lattice representation of the solid. Like the laboratory experiments described in the previous chapter, these simulations consider the influence of horizontal stress contrasts between layers, vertical stress, material fracture toughness, and presence of horizontal weak interfaces. The numerical results match well to laboratory experimental benchmarks, and they extend the parametric study beyond what can be considered in the laboratory. By way of this expanded parametric space, the vital role of the weak horizontal interfaces on hydraulic fracture containment can be appreciated through quantified demonstration of the conditions under which one must consider the presence of weak interfaces for accurate predictions.

3.2 ABSTRACT

This paper presents a study of hydraulic fracture containment in layered reservoirs using a numerical model that couples fluid flow with a lattice representation of the solid with quasi-random distributed nodes connected by springs. We consider the influence of horizontal stress contrasts between layers, vertical stress, material fracture toughness, and the presence of horizontal weak interfaces. The behavior observed in the numerical simulations defines dis-

tinct regions in a parametric space characterized by height growth, containment, and growth along the horizontal weak interface (T-shape growth). In this regard, these numerical results match well to laboratory experimental benchmarks, and they extend the parametric study beyond what can be considered in the laboratory. The work also shows that relative fracture height in the numerical simulation is similar to laboratory benchmarks and is smaller than predicted by equilibrium height growth predictions that neglect the presence of horizontal weak interfaces.

3.3 INTRODUCTION

Hydraulic fracturing has been widely used for enhancing gas and oil recovery. Accurate prediction of fracture height growth/containment is important for successful design and therefore it has been studied for decades. The previous studies include laboratory experiments (e.g. [El Rabaa 1987](#), [Teufel & Clark 1984](#), [Jeffrey & Bungler 2009](#), [Xing et al. In Press](#)) and model predictions (e.g. [Simonson et al. 1978](#), [Warpinski & Teufel 1987](#), [Daneshy 1978](#)). Although stress contrasts between reservoir and adjacent layers may often determine the leading behavior of the height growth, other parameters, such as interlayer contrasts in fracture toughness ([Simonson et al. 1978](#)), permeability ([de Pater & Dong 2009](#)), and stiffness ([Van Eekelen 1982](#)), can also influence height growth.

In addition to these better-studied factors, weak interfaces (e.g. bedding planes) above and/or below the reservoir can substantially limit height growth. The affect of weak interfaces on height growth has long been recognized through model predictions ([Daneshy 1978](#)), field observations ([Warpinski & Teufel 1987](#)), and in laboratory experiments ([El Rabaa 1987](#), [Teufel & Clark 1984](#)). [Xing et al. \(In Press\)](#) carried out an experimental study that considers both the stress contrasts and the presence of the horizontal weak interfaces. They observed four geometric cases: containment, height growth, T-shape growth, and the combination of height growth and T-shape. The differentiation among these cases was shown to depend on the combination of fluid pressure, vertical in-situ stress, horizontal minimum stress in each layer, and the fracture toughness of the layers.

Numerical models that fully couple mechanical deformation, crack growth, fluid flow, and the presence of pre-existing joints (horizontal interfaces) are essential in the exploration of this problem. Numerical analysis can expand the applicability of the parametric study conducted in the laboratory by [Xing et al. \(In Press\)](#). In turn, the laboratory experiments can be used to validate the numerical solution. This laboratory benchmarking of numerical simulations, and subsequent use of numerical simulations to further explore hydraulic fracture containment, comprises the main focus of this paper.

The distinct element method (DEM), introduced by [Cundall \(1971\)](#), can reproduce many of the behaviors of soil and rock including the impact of pre-existing discontinuities ([Cundall 2001](#)). DEM treats the material as an assembly of discrete particles that may or may not be bonded together. [Pine & Cundall \(1985\)](#) conducted the initial application of DEM to hydraulic fracturing of rock masses, fully coupling a hydro-mechanical model that includes the fluid flow in rock joints as approximated by the lubrication equation. However, the original coupled DEM models can only be used when the fracture path is known. To overcome this limitation, the synthetic rock mass (SRM) approach has been developed ([Pierce et al. 2007](#)). The SRM includes a bonded particle model (BPM) representing brittle rock matrix and a smooth joint model (SJM) representing the pre-existing joints. The BPM can represent crack growth including matching the fracture toughness and reproducing the scale effect ([Potyondy & Cundall 2004](#)). The SJM allows slip and separation at particle contacts while respecting the given joint orientation. The original implementations of the SRM models employ assemblies of circular/spherical particles bonded together, realized in the general-purpose codes PFC2D ([Itasca Consulting Group 2014a](#)) and PFC3D ([Itasca Consulting Group 2014b](#)).

The most recent implementation of the SRM concept uses a lattice representation of the rock matrix. Here the balls and contacts of PFC3D are replaced by point masses (nodes) and connecting springs ([Damjanac et al. 2015](#)). The lattice representation has precedent for the simulation of fracture in concrete (see [Schlangen & Garboczi 1997](#), [Bolander & Sukumar 2005](#), [Grassl & Bažant 2009](#)), including the deformation and fracture of concrete coupled with fluid flow (see e.g. [Grassl 2009](#), [Grassl et al. 2015](#)). Lattice models for simulation of jointed rock masses offer advantages over both continuum models and full DEM models

in terms of both computational efficiency and flexibility (Cundall 2011). Thus motivated, a three dimensional lattice-based hydraulic fracture simulator, XSite, has been developed (Damjanac et al. 2015).

The current study focuses on numerical simulation of hydraulic fracture growth in layered reservoirs using XSite considering different horizontal and vertical confining stress, different fracture toughness, and the presence of horizontal weak interfaces. Specifically, we focus on benchmarking XSite with respect to the experimental data presented by Xing et al. (In Press), after which we expand the parametric study originally carried out in these experiments. First we will briefly describe the setup of the experiments, and the lattice model used by XSite, after which we present the results of the numerical simulations including comparison with experimental results.

3.4 EXPERIMENTAL METHODS

The experiments carried out by Xing et al. (In Press) provide the benchmark for the numerical study in this paper. They were run with a three-layered medium constructed from transparent polyurethane (PU) that enables real-time monitoring of the evolution of the hydraulic fracture geometry. In order to enable control of the strength of the material associated with both vertical and horizontal hydraulic fracture growth, each layer was subdivided into two sub-blocks, as shown in Fig. 3.1. The length and width of the specimen are both 152.4 mm. The height of the top and bottom barriers is 50.8 mm. The reservoir height was varied, with specimens using a 50.8 mm, 25.4 mm, or 12.7 mm reservoir layer. Thus, the ratio of final crack length L over reservoir height H_R varies from 1.5 to 6. The experiments are detailed in Xing et al. (In Press).

The loads were applied with hydraulic actuators using two axes of a true tri-axial loading frame. Transparent polymethyl methacrylate (PMMA) blocks were used to evenly spread the load from the smaller actuators to the PU specimens (Fig. 3.1). The reservoir layer and the bounding layers are made of PU materials with different Young's moduli to generate the

stress contrasts upon application of the loading via platens that are much stiffer than the specimen (see [Xing et al. In Press](#)).

One of the key elements in these experiment is that the horizontal interfaces between the reservoir and adjacent layers were left unbonded so as to comprise the weak interfaces. In contrast, the strength of the vertical interfaces was varied, providing an analogue for the strength of the reservoir and barrier rocks. The vertical interfaces ranged from the limiting unbonded case to three bonded cases corresponding to different toughnesses, obtained by using different adhesives. After the loading, glycerin mixed with food dye was injected into the reservoir layer through a 3.175 mm injection hole by a syringe pump. The hydraulic fracture initiated in the interface between two blocks of the reservoir layer. The fracture paths in the experiments are prescribed; the fracture could only propagate along the interfaces between different blocks. Hydraulic fracture geometry, fluid pressure, pump rate, confining stresses, and fracture geometries were recorded during the whole procedure. By varying the stress conditions, four different geometries were obtained (see [Fig. 3.2](#)). Containment occurred when the vertical and barrier stresses were both sufficiently large compared to the reservoir stress and fluid pressure. Height growth occurred for smaller barrier stress, and T-shaped growth occurred for smaller vertical stress. Combination cases were observed over narrow ranges of parameters at transitions among the the basic geometries. A parametric space defining the stress conditions associated with these geometries is presented later along with results of the numerical simulations.

3.5 LATTICE MODEL DESCRIPTION

3.5.1 Geometry and mechanical formulation

The model is based upon a lattice formulation for simulation of deformation and fracturing of the solid. The lattice is a set of nodes connected by 1D springs. In this model, the nodes (point masses) are placed in a quasi-random arrangement with the mean nodal spacing set by a user-defined model resolution ([Damjanac & Cundall 2016](#)). There are two methods of

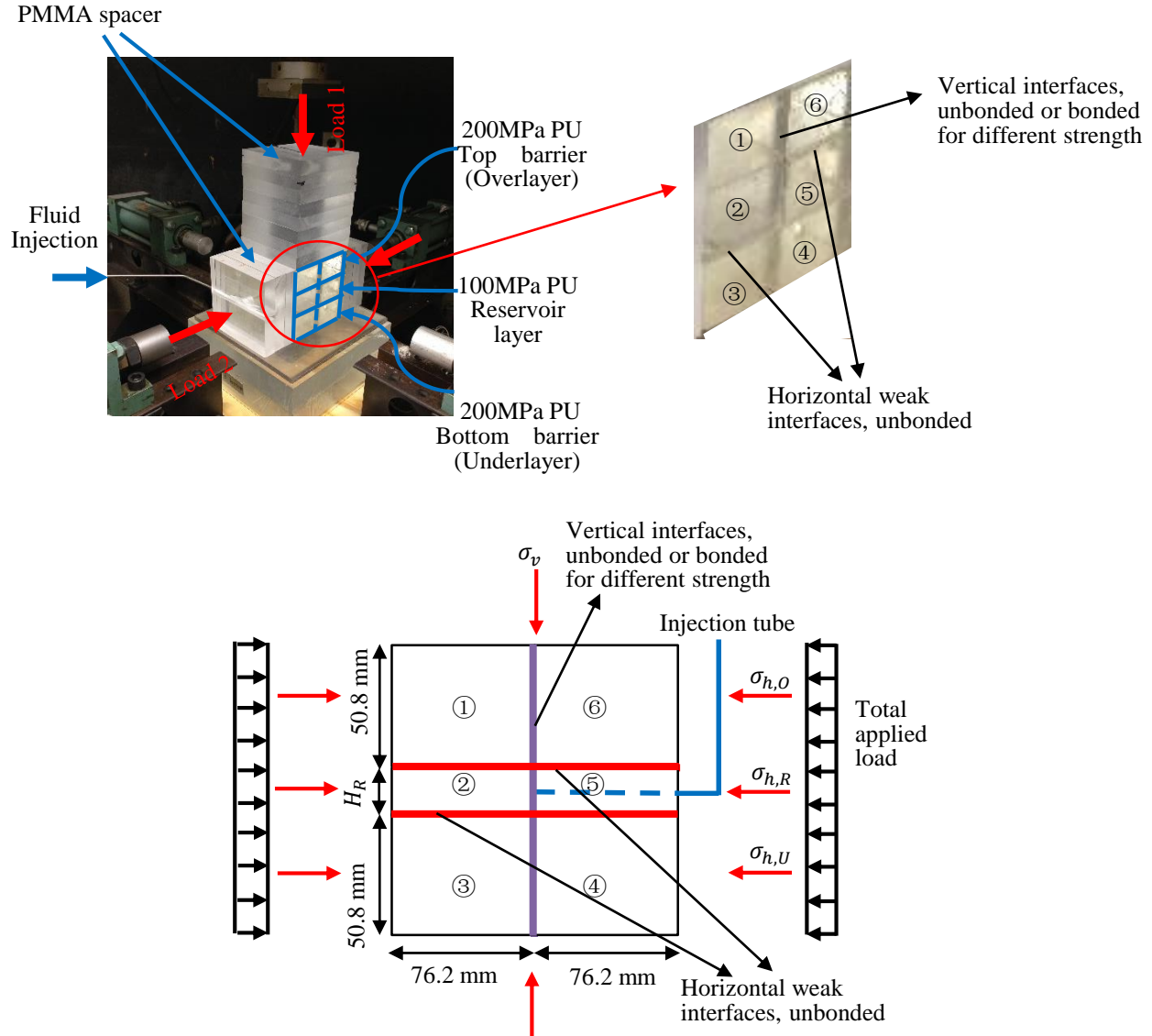


Figure 3.1: The experimental setup from Xing et al. (In Press), showing the specimen composed of six sub-blocks. Sub-blocks 1 and 6 comprise the top barrier; sub-blocks 2 and 5 comprise the analogue reservoir layer; sub-blocks 3 and 4 comprise the bottom barrier. There are three different analogue reservoir heights H_R : 50.8 mm, 25.4 mm and 12.7 mm. The stresses $\sigma_{h,O}$ (horizontal overlayer confining stress), $\sigma_{h,R}$ (horizontal reservoir confining stress), $\sigma_{h,U}$ (horizontal underlayer confining stress) and σ_v (vertical confining stress) are generated by Load 2 and Load 1. Note that there are two directions of load applied (Load 2 and Load 1) and the other direction is free, however the crack growth orientation is restricted to the planes between the blocks so that the horizontal stress (Load 2) is analogous to the minimum stress.

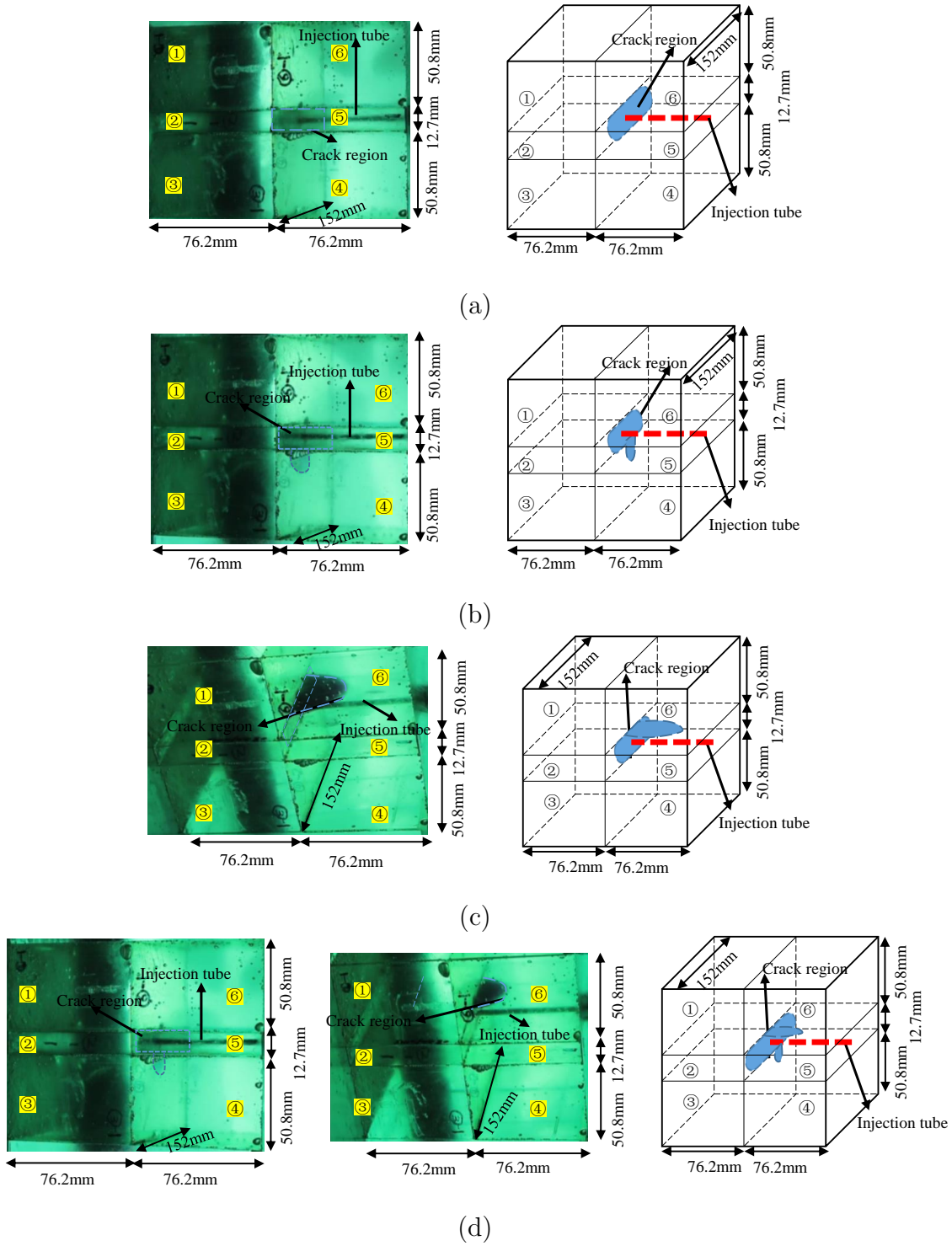


Figure 3.2: Typical fracture geometries, from Xing et al. (In Press): (a) Fracture containment, (b) Limited height growth, (c) T-shape, (d) Limited height growth and T-shape (there are two directions of views required for complete observation). The crack region is outlined by blue lines.

generating the springs that connect the nodes: regular and Voronoi. In the regular lattice the springs are based on contact relations between imagined spherical particles (i.e., the model created in PFC3D). In the Voronoi lattice, the springs are placed based on Voronoi tessellation in 3D space, where the springs are created at common faces of the discretization domains (Damjanac et al. 2015).

Once the nodes are placed and connected by springs, the law of motion for each node can be expressed according to linear momentum balance and an explicit time stepping expressing the displacement in terms of the nodal velocity, that is

$$\begin{aligned}\dot{u}_i^{(t+\Delta t/2)} &= \dot{u}_i^{(t-\Delta t/2)} + \Sigma F_i^{(t)} \Delta t / m \\ u_i^{(t+\Delta t)} &= u_i^{(t)} + \dot{u}_i^{(t+\Delta t/2)} \Delta t\end{aligned}\tag{3.1}$$

where $\dot{u}_i^{(t)}$ and $u_i^{(t)}$ are the velocity and position (respectively) of component i ($i = 1, 3$) at time t , m is the mass of node, and $\Sigma F_i^{(t)}$ is the sum of all force components i acting on the nodes with time step Δt . Then, the force changes in the springs can be calculated using the relative displacements of the nodes according to

$$\begin{aligned}F^N &\leftarrow F^N + \dot{u}_i^N k^N \Delta t \\ F_i^S &\leftarrow F_i^S + \dot{u}_i^S k^S \Delta t\end{aligned}\tag{3.2}$$

where N denotes “normal”, S denotes “shear”, k is the spring stiffness, and F is the spring force. If the force exceeds the calibrated spring strength (either in tension or shear), the spring breaks and a microcrack is formed.

3.5.2 Fluid flow formulation

A fluid flow model is an essential part of any hydraulic fracture simulator. Fluid flow in hydraulic fracture(s) is solved using a network of pipe-like fluid elements located at the centers of springs that are either broken or that were initially designated represent pre-existing joints. Pipes are thus formed between the fluid elements within a certain distance between each other, a function of the resolution. The pipe network evolves with the development of damage in the mechanical model and is updated automatically by connecting newly formed

microcracks to the existing ones. Using the lubrication equation, the flow rate q along a pipe from fluid node A to node B, is calculated as (Damjanac et al. 2015):

$$q = \beta \frac{w^3}{12\mu} [p^A - p^B + \rho_w g (z^A - z^B)] \quad (3.3)$$

where w is hydraulic aperture, μ is the viscosity of the fluid, p^A and p^B are the fluid pressures at nodes A and B, respectively, z^A and z^B are the elevations of nodes A and B, respectively, and ρ_w is fluid density. A fluid reservoir in node A or B is regarded as a penny-shaped crack with the aperture w that depends on its fluid content. The dimensionless number β is a built-in calibration parameter, a function of resolution that is obtained through matching the conductivity of a pipe network to the conductivity of a joint represented by parallel plates with aperture w . Note that although the pipes are linear elements, a network of pipes in a plane can in this way approximate planar fluid flow (Damjanac et al. 2015). In XSite, the mechanical deformation and flow models are fully coupled by the dependence of w on the local deformation of the solid.

3.5.3 Joints

In order to model a typical rock mass, it is necessary to represent pre-existing joints (discontinuities). In XSite, each joint consists of a planar array of bonds that obey the smooth joint model (SJM). The SJM allows slip and separation at particle contacts, while respecting the given joint orientation rather than local contact orientations (Damjanac & Cundall 2016). Separation and slip on the joint plane are modeled as limits on spring forces, resolved in the joint directions via the following logic:

- if the force generated by the fluid pressure is greater than the normal force of joint spring, then both the normal force and shear force of the joint springs will become zero;
- if the force generated by fluid pressure is smaller than the normal force of the springs, then the shear force of the joint springs will be updated to the smaller of the previous shear force and the value obtained by the Coulomb slip law.

This logic can be expressed as (Cundall 2011):

$$\begin{aligned} \text{If } F^n - pA < 0 \text{ then } F^n = 0, F_i^s = 0 \\ \text{else } F_i^s \leftarrow \frac{F_i^s}{|F_i^s|} \min \{ (F^n - pA) \tan \phi, |F_i^s| \} \end{aligned} \quad (3.4)$$

where ϕ is the friction angle, F^n is the normal force (compression positive), F_i^s is the shear force, p is the fluid pressure in the joint segment, and A is the apparent area of the segment determined by common faces of the discretization domains.

3.5.4 Macroscopic and spring parameters

The spring stiffness in lattice models must be chosen to correspond to the elastic moduli of the rock mass. Also, the spring strength must be chosen so as to replicate the macroscopic strength of the rock. In XSite the user may specify typical macroscopic elastic properties, as it is done for continuum-based numerical models. The calibration factors that relate macroscopic parameters (e.g. Young's modulus, Poisson's ratio and tensile strength of the joint) and spring properties (e.g. normal spring stiffness, shear spring stiffness, and spring strength) are built-in, because the generated node arrays are derived by scaling from a previously determined, calibrated relationship (Damjanac et al. 2015).

Under Voronoi tessellation the simulator uses tensile strength and fracture toughness to determine the spring properties. The spring tensile strength F_{max}^N is calculated based on both criteria, and whichever is satisfied first will be active. Otherwise, with regular tessellation only the tensile strength criterion is used. The desire to make use of the fracture toughness criterion thus motivates choosing the Voronoi tessellation as the method for generating the springs in our study.

3.5.5 Toughness calibration

Before simulating hydraulic fracture growth, it is necessary to relate the material fracture toughness to the tensile strength of the rock matrix or the pre-existing joints by calibration. Here we limit consideration of fracture growth to the pre-existing joints. This limitation is justified in light of the goal being to simulate laboratory experiments for which hydraulic

fracture growth was restricted to pre-existing interfaces between blocks. In XSite, for the pre-existing joints, tensile strength, shear strength and friction angle can be defined but fracture toughness cannot be directly defined. Instead it is obtained by choice of the combination of tensile strength and model resolution. Hence the purpose of the calibration is to build this relationship. To do this, a strain-controlled numerical pull off test on a dry sample of dimensions 0.15 m × 0.15 m × 0.112 m containing an initial through crack of 0.035 m half-length was performed (Fig. 3.3a). The initial crack was modeled using a very weak pre-existing joint (tensile strength is zero) while the bonded region used pre-existing joints with finite strength. The reaction force was monitored and so the fracture toughness can be calculated by (Tada et al. 2000):

$$K_{Ic} = \sigma \sqrt{\pi a} \left[\sec \left(\frac{\pi a}{2W} \right) \right]^{1/2} \left[1 - 0.025 \left(\frac{a}{W} \right)^2 + 0.06 \left(\frac{a}{W} \right)^4 \right] \quad (3.5)$$

where σ is the far field stress at the peak force, a is the half length of the crack, and W is the half length of the specimen.

Fig. 3.3b shows the calibration results for the case with tensile strength $\sigma_t=0.75$ MPa, resolution $R=0.004$ m and loading velocity 0.005 m/s. Here, the peak force is 3953.3 N and the fracture toughness is calculated as 0.068 MPa · m^{1/2} based on Eq. 3.5. Figs. 3.3c and 3.3d describe the calibration results with different resolutions, namely $R = 0.004$ m and $R = 0.003$ m, respectively. The proposed curves relating joint tensile strength and fracture toughness are found in this way to be linear and can be expressed as

$$\begin{aligned} K_{Ic} &= 0.089\sigma_t + 7.3 \times 10^{-4} \text{ MPa} \cdot \text{m}^{\frac{1}{2}}, & R &= 0.004 \text{ m} \\ K_{Ic} &= 0.078\sigma_t + 1.0 \times 10^{-3} \text{ MPa} \cdot \text{m}^{\frac{1}{2}}, & R &= 0.003 \text{ m} \end{aligned} \quad (3.6)$$

Note that in the following numerical simulations of hydraulic fracture growth, we used different resolutions in different layers (0.004 m in the barrier layer, 0.003 m in the reservoir layer) in order to increase the computation efficiency. The resulting small difference in fracture toughness for different layers does not significantly impact the solution. Hence, for a certain value of fracture toughness in experiments, we defined the interface tensile strength by averaging the results from Eq. 3.6 for different resolutions ($R=0.004$ m and 0.003 m),

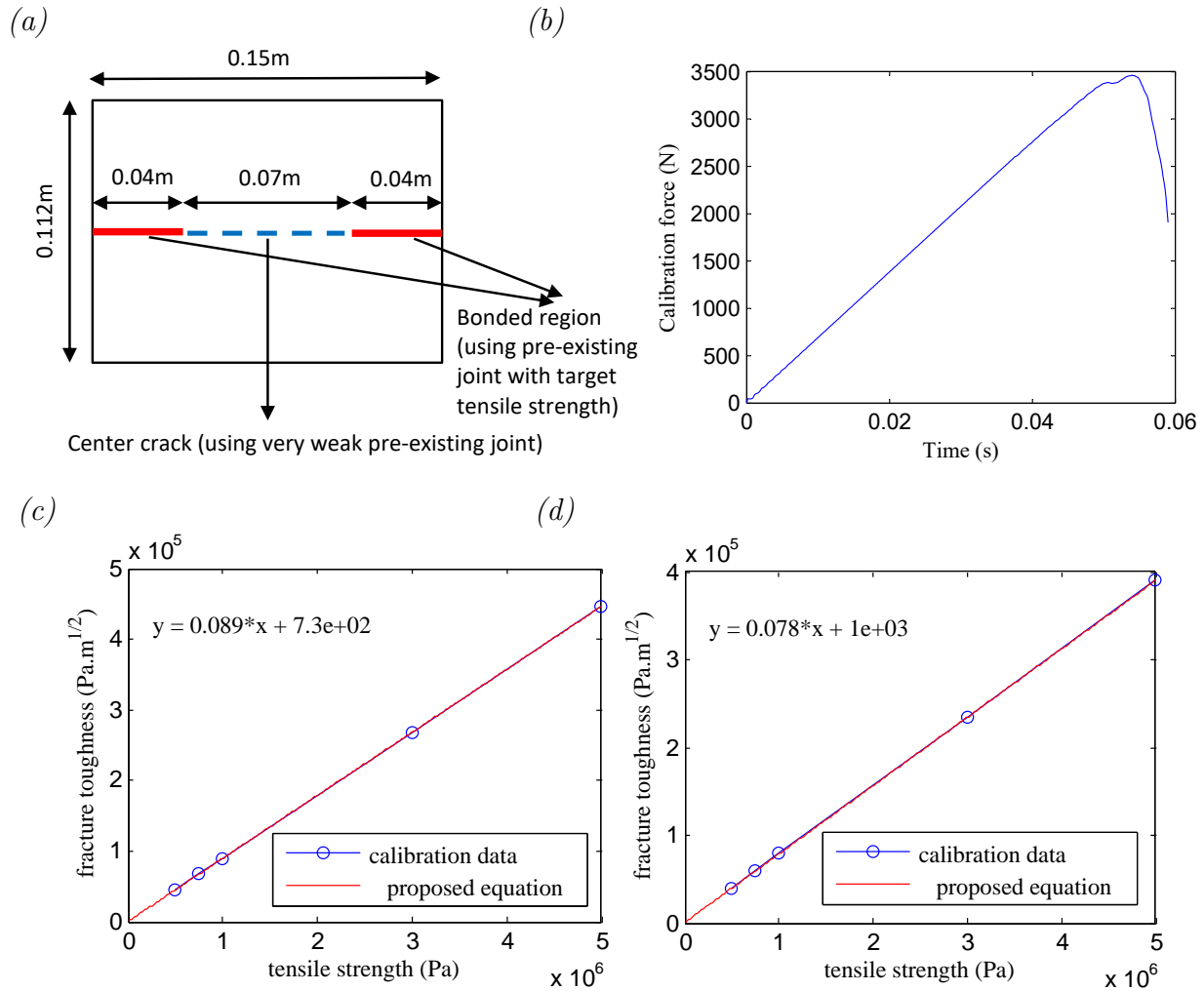


Figure 3.3: Fracture toughness calibration for the pre-existing joint: (a) sketch of the calibration experiment, (b) simulated force versus time for the case with $\sigma_t = 0.75$ MPa and $R = 0.004$ m, (c) fracture toughness versus tensile strength for resolution $R=0.004$ m and (d) fracture toughness versus tensile strength for resolution $R=0.003$ m.

as shown in Table 3.1. Also, the equivalent fracture toughness of the vertical interface in different layers is listed in Table 3.1.

3.5.6 Verification problem

Before simulating the hydraulic fracture experiment, we benchmark our model to a relevant analytical solution. The verification problem is a circular hydraulic fracture propagating in a viscosity dominated regime with no leak-off (Savitski & Detournay 2002). The simulation is carried out at laboratory scale with parameters chosen to match laboratory conditions. The dimension of the domain is $0.15 \times 0.15 \times 0.15$ m and the applied confining stress perpendicular to the fracture plane is 1 MPa, similar in magnitude to the experiments. The solid is characterized by a Young's modulus of 100 MPa and Poisson's ratio of 0.25. Fluid with viscosity of $0.3 \text{ Pa} \cdot \text{s}$ is injected at a constant rate $1 \times 10^{-6} \text{ m}^3/\text{s}$ into the center of the pre-defined joint with the smallest possible initial aperture (10^{-6} m).

Fig. 3.4 shows a visualization of the fluid pressure when the radius has attained 0.013 m, and Fig. 3.5(a) shows the corresponding net fluid pressure profile together with analytical solutions from Savitski & Detournay (2002). The corresponding crack aperture is also shown in Fig. 3.5(b) together with the analytical solution. Besides the point by point values of the numerical results, we also present the averaged value, which is compared with the analytical benchmark. The match is acceptable with deviation strongest near the tip and inlet. The reason for the discrepancy at small distance near the inlet is most likely because the numerical source has a finite size rather than a point source as is assumed in the analytical solution. Near the leading edge, the finite initial aperture allows seepage ahead of the crack tip. In contrast, there is zero initial aperture and thus zero seepage in the theoretical solution (Damjanac et al. 2013).

Table 3.1: Fracture toughness with different adhesives in the experiments and the corresponding tensile strength of vertical interface in XSite.

	Large toughness	Medium toughness	Small toughness
K_{IcE} (MPa · m ^{1/2})	0.40 (Tape A*)	0.069 (Tape B reduced**)	0.026 (Taped A reduced***)
σ_t (MPa)	4.80	0.82	0.30
K_{IcR} (MPa · m ^{1/2})	0.38	0.065	0.027
K_{IcB} (MPa · m ^{1/2})	0.43	0.074	0.024

* Ve-ge carpet tape

** Chica and Jo double sided tape with surface treating agent Amodimethicone

*** Ve-ge carpet tape with surface treating agent Amodimethicone

K_{IcE} - Fracture toughness of the vertical interface used in the experiments

σ_t - Tensile strength of the vertical interface in XSite

K_{IcR} - Equivalent fracture toughness of the vertical interface in the reservoir layer in XSite

K_{IcB} - Equivalent fracture toughness of the vertical interface in the barrier layers in XSite

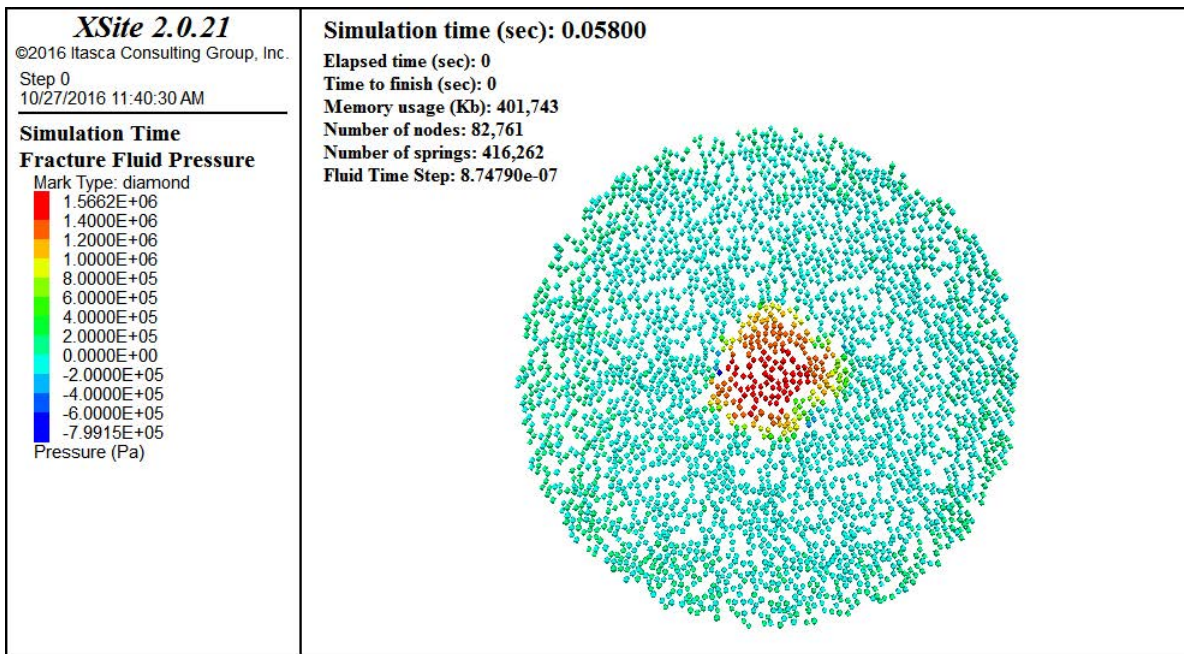
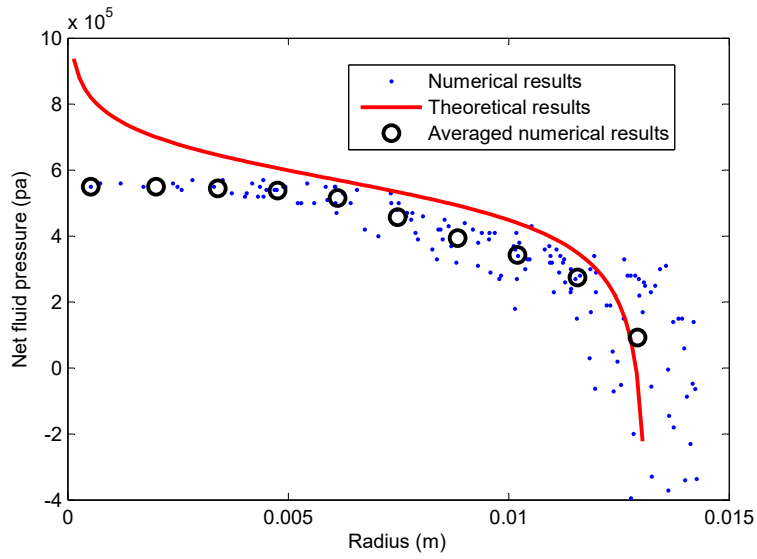


Figure 3.4: The fluid pressure field inside the hydraulic fracture for the verification case. Note the pressure are negative in the outer annulus of the flow disk.

(a)



(b)

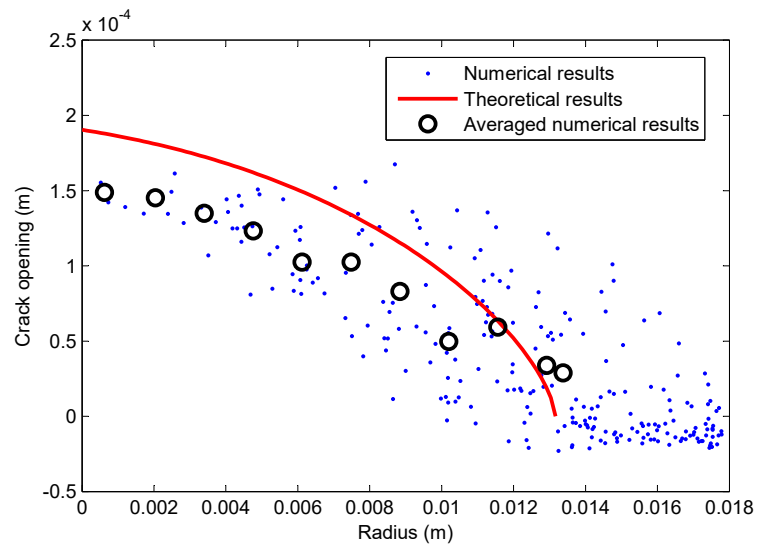


Figure 3.5: The verification case at 0.058 s (0.013 m radius) showing: (a) Net fluid pressure profile, and (b) crack aperture profile.

3.6 NUMERICAL SIMULATIONS

XSite is now used to simulate the conditions of the laboratory experiments described in Section 2. The model is set up with three layers. The middle reservoir layer has smaller horizontal confining stress compared to the top and bottom layers. The horizontal interfaces between each layer are defined by “very weak” pre-existing joints where tensile strength is zero, cohesion is zero and friction coefficient is 0.01. The tensile strength of the vertical interface varies from zero to finite values corresponding to the fracture toughness used in the experiments (Table 3.1).

The dimensions and boundary conditions of the simulation are the same as the experiments, as shown in Fig. 3.6. The Young’s modulus of the reservoir layer is 100 MPa and barriers is 200 MPa. The Poisson’s ratio of all the layers is 0.4. The injection rate is 2×10^{-7} m³/s and the fluid viscosity is 0.3 Pa · s. In the barrier layers the resolution is 0.004 m and in the reservoir layer the resolution is 0.003 m. With these parameters and the specimen dimensions fixed, the parametric study consists of varying the toughness of the vertical interfaces and the horizontal and vertical confining stresses.

Recall that in the experiments we obtained four geometries: containment, limited height growth, T-shape growth, and the combination of limited height growth and T-shape (see Fig. 3.2). Our intent here is to explore conditions leading to these geometries in the simulations. However, due to the initial aperture of the pre-existing joints (the minimum value is 1×10^{-6} m), there is always a non-zero fluid volume penetrating into the horizontal interface accompanied by a non-zero opening. Therefore, we set the criteria for the geometries based on the crack aperture ratio and fluid volume ratio. These criteria are detailed in Table 3.2. Please note that there is no standard to refer to for devising these criteria. We first roughly design the criteria and then adjust them according to the experimental data under zero toughness presented in the parametric space. Then in numerical simulations of other cases with finite toughness vertical interface, the same criteria are used. That is to say, the exact threshold values in the criteria are calibrated according to the experimental data. Similar to the experiments, we numerically obtained all four geometries according the criteria defined by Table 3.2:

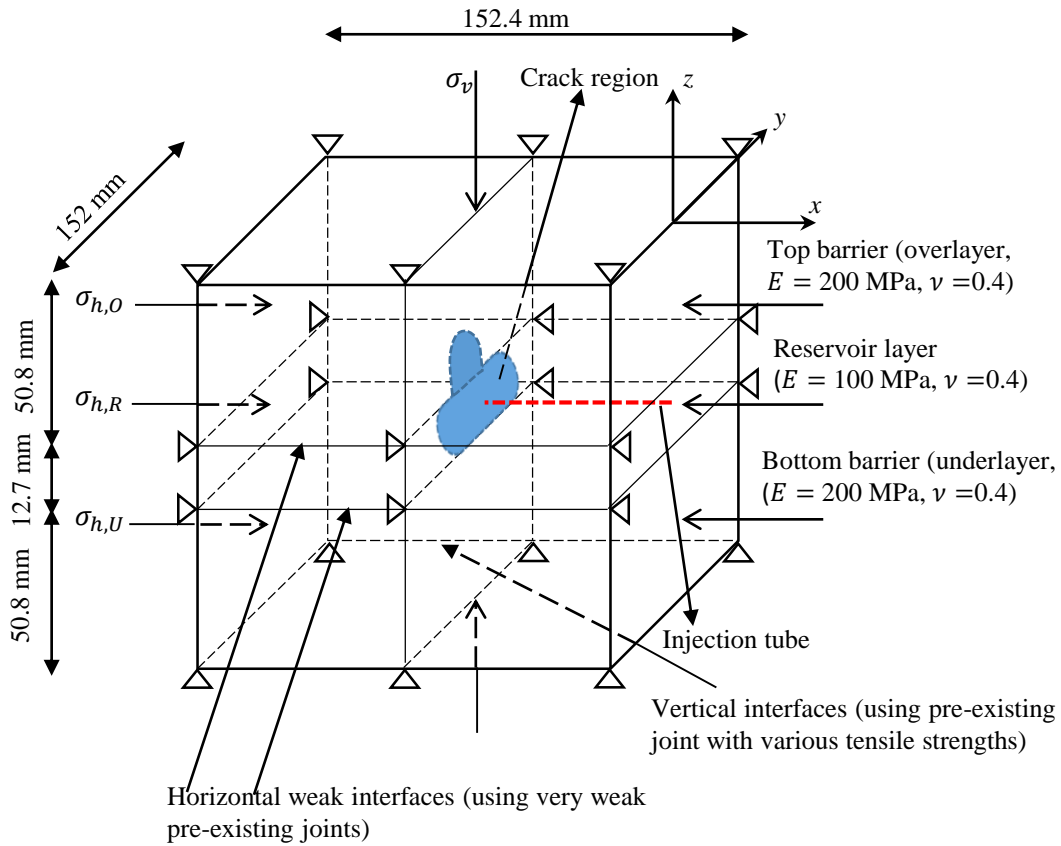


Figure 3.6: Sketch of the numerical model. The model far-field boundary conditions are fixed displacement. Here σ_v is the vertical confining stress, $\sigma_{h,R}$ is the confining stress of reservoir, $\sigma_{h,O}$ is the overlayer horizontal confining stress, and $\sigma_{h,U}$ is the overlayer horizontal confining stress.

- 1) *Limited height growth.* Fig. 3.7 illustrates a typical case of limited height growth. Note that similar to experiments, the horizontal confining stress in the top bounding layer (overlayer) is smaller than that of the bottom bounding layer (underlayer), thus promoting upward height growth. The crack aperture profiles show that the crack aperture of the barrier is greater than 6% of the maximum crack aperture of the reservoir while the crack aperture of the horizontal interface are smaller than 5%. The crack aperture ratio together with the calculated volume ratio indicates limited height growth according to Table 3.2.

- 2) *Containment.* A typical case of containment is described in Fig. 3.8. The fracture only propagates in the reservoir layer. Note although the pressure of some elements of the overlayer are greater than zero, they could be neglected according to the criteria in Table 3.2. This is evidenced by the crack aperture profiles showing that both the crack aperture of the barrier and the horizontal interface are smaller than the critical ratio (6% and 5% respectively) of the maximum crack aperture in the reservoir.

- 3) *T-shape growth.* Fig. 3.9 shows a typical case of T-shape growth. The pressure distribution indicates that fluid significantly penetrated into the horizontal weak interfaces, forming a T-shape geometry when viewed growth together with the fracture in the reservoir. The crack aperture profiles show that the crack aperture within the barrier is smaller than 6% of the maximum crack aperture of the reservoir, while the crack apertures in the horizontal interfaces are greater than 5%, which together with the calculated volume ratio indicates the T-Shaped growth case.

- 4) *Combination of T-shape and limited height growth.* Fig. 3.10 is a typical example of the combination geometry. The fracture simultaneously propagates in the reservoir layer, the top barrier, and the horizontal weak interfaces. As we can see from the crack aperture profiles that both the crack aperture of the barrier and the horizontal interface are greater than the critical ratio (6% and 5% respectively) of the maximum crack aperture of the reservoir. The crack aperture ratio and calculated volume ratio both satisfy the criteria for the combination case.

Table 3.2: Criteria for fracture geometries based on crack aperture and fluid volume ratio.

Limited height growth	$w_O/w_{max} > 0.06,$ $w_H/w_{max} \leq 0.05,$	$V_O/V_{total} > 0.05$ $V_H/V_{total} \leq 0.05$
T-shape growth	$w_O/w_{max} \leq 0.06,$ $w_H/w_{max} > 0.05,$	$V_O/V_{total} \leq 0.05$ $V_H/V_{total} > 0.05$
Containment	$w_O/w_{max} \leq 0.06,$ $w_H/w_{max} \leq 0.05,$	$V_O/V_{total} \leq 0.05$ $V_H/V_{total} \leq 0.05$
Combination	$w_O/w_{max} > 0.06,$ $w_H/w_{max} > 0.05,$	$V_O/V_{total} > 0.05$ $V_H/V_{total} > 0.05$

w_{max} - the maximum crack aperture in the reservoir layer,
 w_O - the maximum crack aperture in the barrier layer with smaller confining stress (overlayer in the current configuration),
 w_H - the maximum crack aperture in the horizontal interface,
 V_O - the fluid volume of overlayer,
 V_{total} - the total injected fluid volume,
 V_H - the fluid volume of the horizontal interface (one wing).

In order to compare the numerical results with the experiments, we present them in the same parametric space defined by \mathcal{H}_b and \mathcal{H}_v , which are expressed as (Xing et al. In Press)

$$\begin{aligned}\mathcal{H}_b &= \frac{\sigma_{h,B} - \sigma_{h,R}}{p_{net}} \\ \mathcal{H}_v &= \frac{\sigma_v - \sigma_{h,B}}{p_{net}}\end{aligned}\quad (3.7)$$

Here p_{net} is the net fluid pressure at the wellbore, taken as a difference between the fluid pressure p_f and the reservoir confining stress $\sigma_{h,R}$, noting that the fluid pressure is taken at the end of each simulation, when the hydraulic fracture reaches the boundary of the domain. Also σ_v is the vertical confining stress and $\sigma_{h,B}$ is the horizontal barrier confining stress (the smaller of the overlayer and underlayer $\sigma_{h,O}$ and $\sigma_{h,U}$, respectively). These two parameters therefore embody comparisons of net fluid pressure with the horizontal stress contrast between the barrier and reservoir, and the stress contrast between the vertical stress acting on horizontal bedding plane and horizontal stress in the barrier, respectively. Hence, when $\mathcal{H}_b \rightarrow 0$, the stress jump to the barrier layer(s) vanishes and the height growth is expected to be unbounded. In contrast, for large \mathcal{H}_b , the fracture growth is expected to

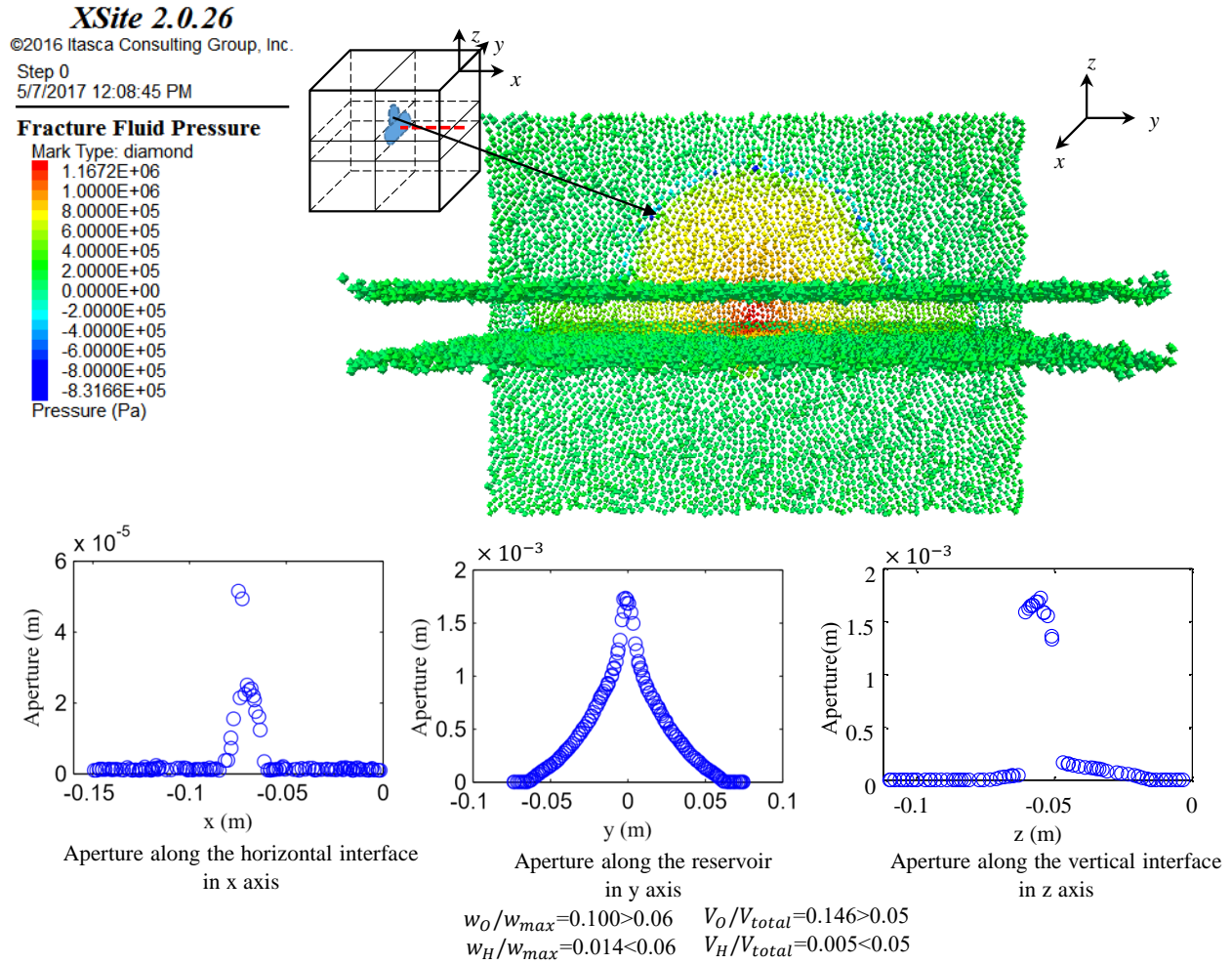


Figure 3.7: Pressure distribution for the vertical interface (top) and the crack aperture profiles (bottom) for a limited height growth case.

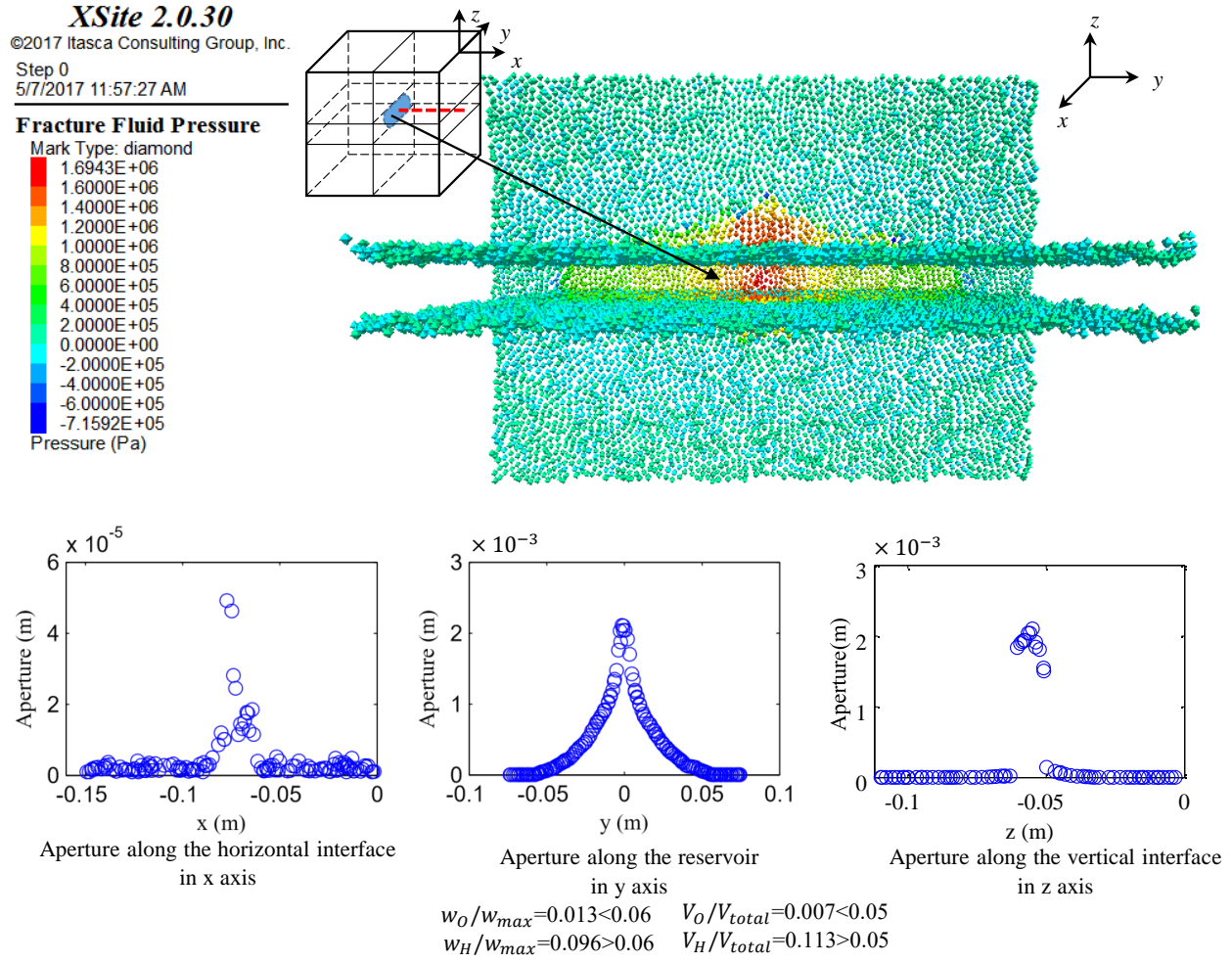


Figure 3.8: Pressure distribution for the vertical interface (top) and the crack aperture profiles (bottom) for a containment case.

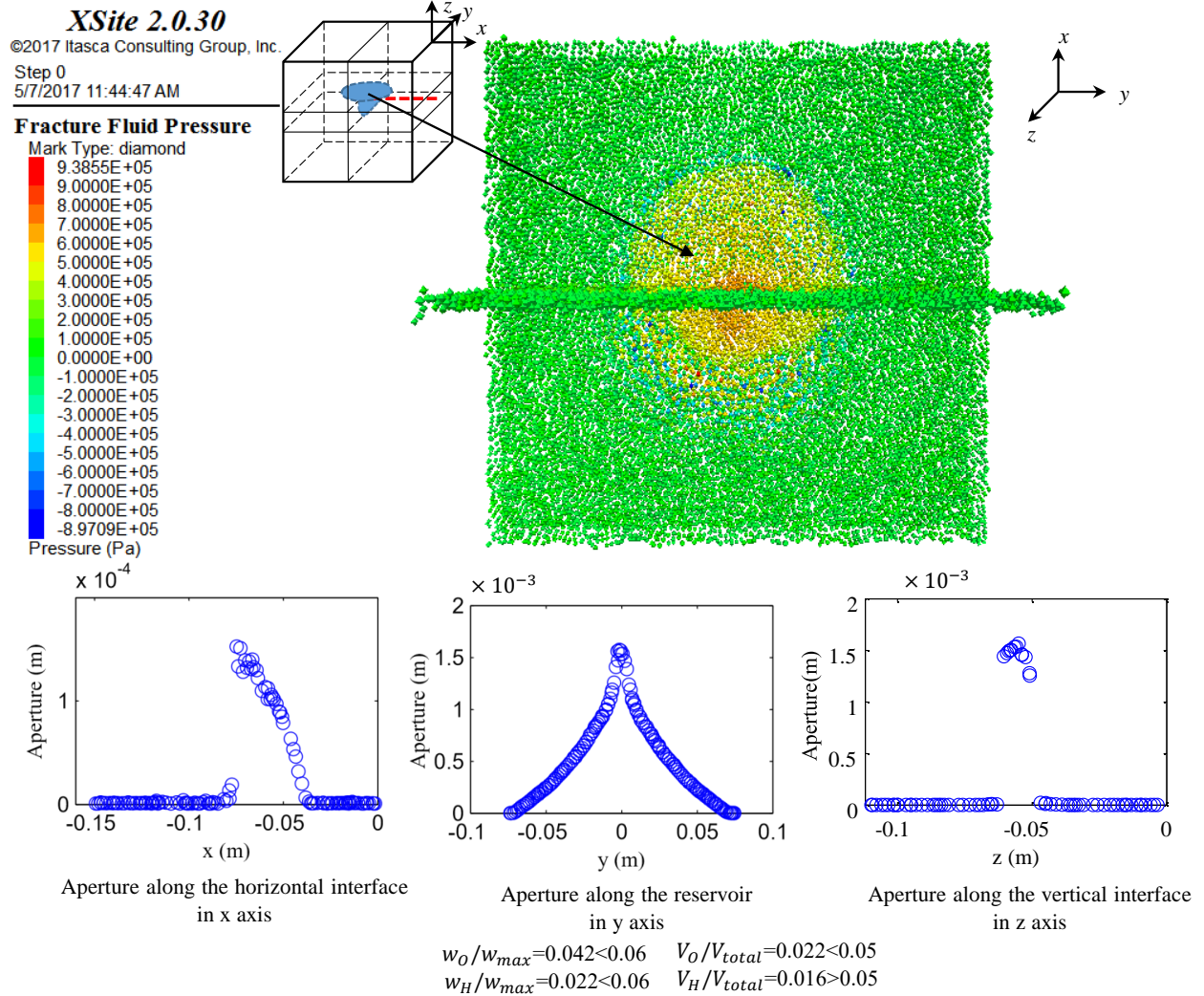


Figure 3.9: Pressure distribution for the horizontal interface (top) and the crack aperture profiles (bottom) for case with a T-shape growth.

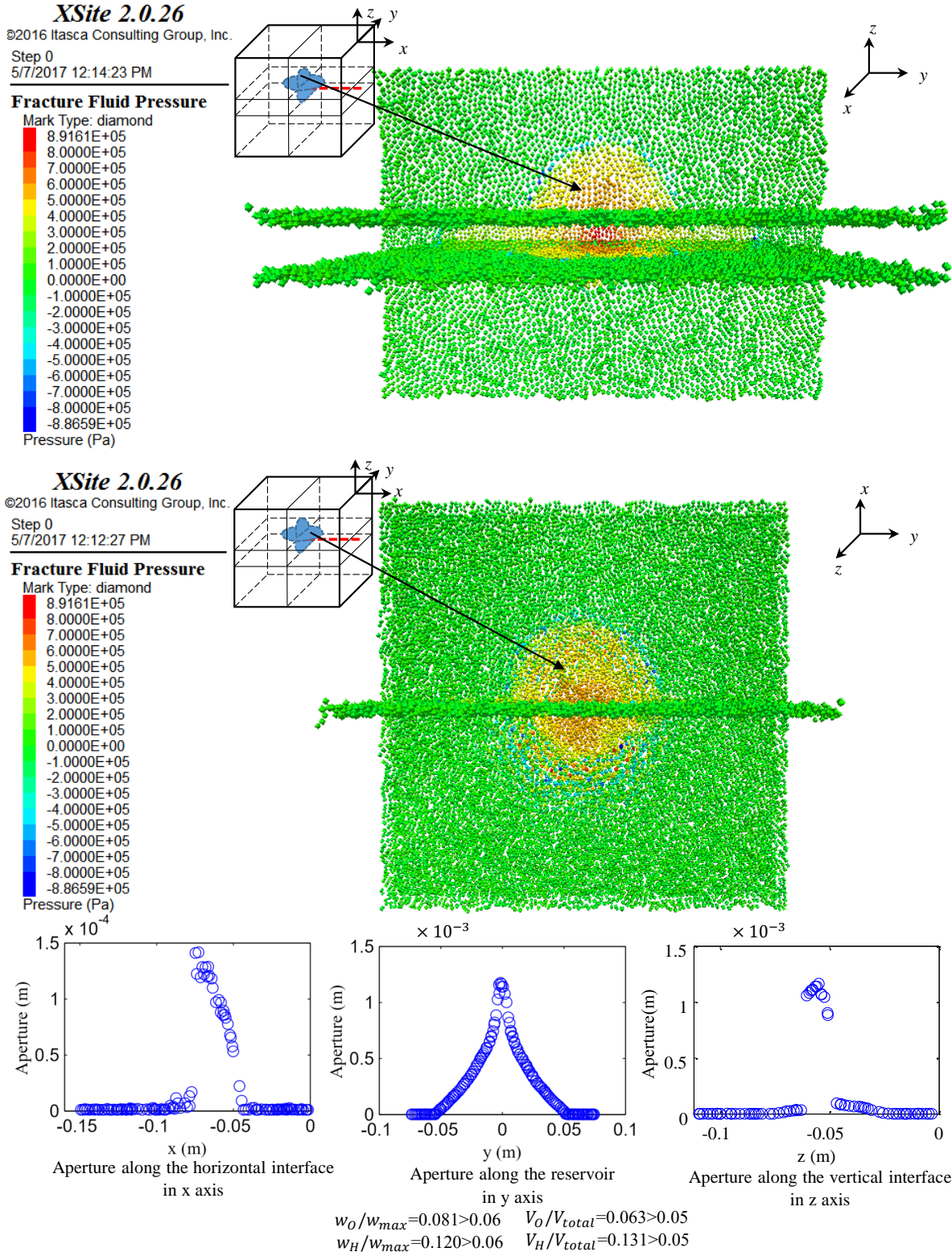


Figure 3.10: Pressure distribution for the vertical interface (top) and horizontal interface (middle) as well as the crack aperture profiles (bottom) for a combination for T-shape and limited height growth case.

be restricted to the reservoir and/or horizontal bedding planes. On the other hand, whether fracture growth occurs on the horizontal bedding plane is proposed to be embodied mainly by \mathcal{H}_v ; smaller values of \mathcal{H}_v correspond to cases with relatively smaller vertical stresses which are more likely to promote growth along the horizontal weak interfaces.

3.6.1 Zero and small toughness vertical interface

First we present numerical simulation results with zero toughness vertical interfaces, that is, cases for which tensile strength of the interface is set as zero. The numerical simulation results are presented in the \mathcal{H}_b and \mathcal{H}_v parametric space, and are compared to the experimental results as shown in Fig. 3.11. Generally, the simulation results match the experiments very well. The numerical results show all four geometries, including the combination of T-shape growth and limited height growth near the boundary of T-shape growth cases and limited height growth cases. This behavior was also observed in the experiments.

Besides providing numerical results in the range of \mathcal{H}_b and \mathcal{H}_v accessed by the experiments, we also carried out numerical simulations when \mathcal{H}_v is larger ($2 < \mathcal{H}_v < 8$), thus enabling the drawing of lines A and B to describe the boundaries between different geometries in the parametric space.

We find that for the cases of small toughness vertical interfaces, the numerical and experimental results are indistinguishable from the zero toughness cases as shown (Fig. 3.12). Most importantly, both the experimental and numerical cases define essentially the same regions in the parametric space with the exception of only a few cases very near the boundaries between the regions zero and small toughness cases. Hence we conclude the numerical simulation results match well with the experiments.

3.6.2 Medium to large toughness vertical interface

For cases with medium to large toughness of the vertical interface, we set the tensile strength of the vertical interface according to Table 3.1 while leaving the horizontal interface tensile strength as zero (recall Fig. 3.6).

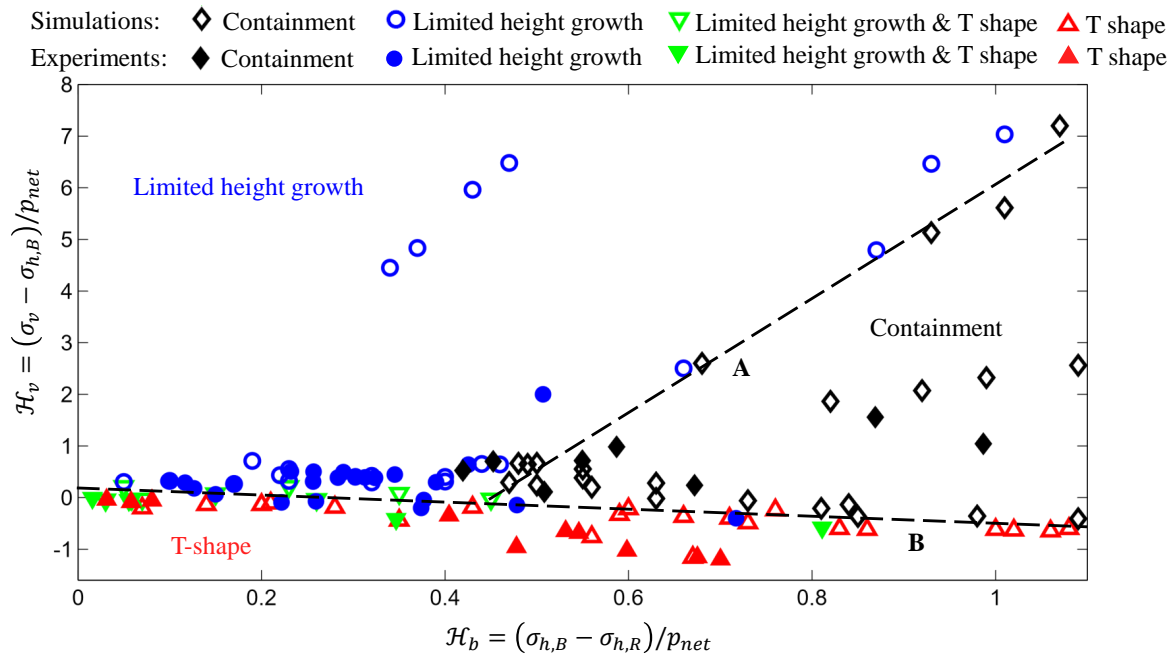


Figure 3.11: Comparison of simulation and experimental results for cases with zero toughness vertical interfaces.

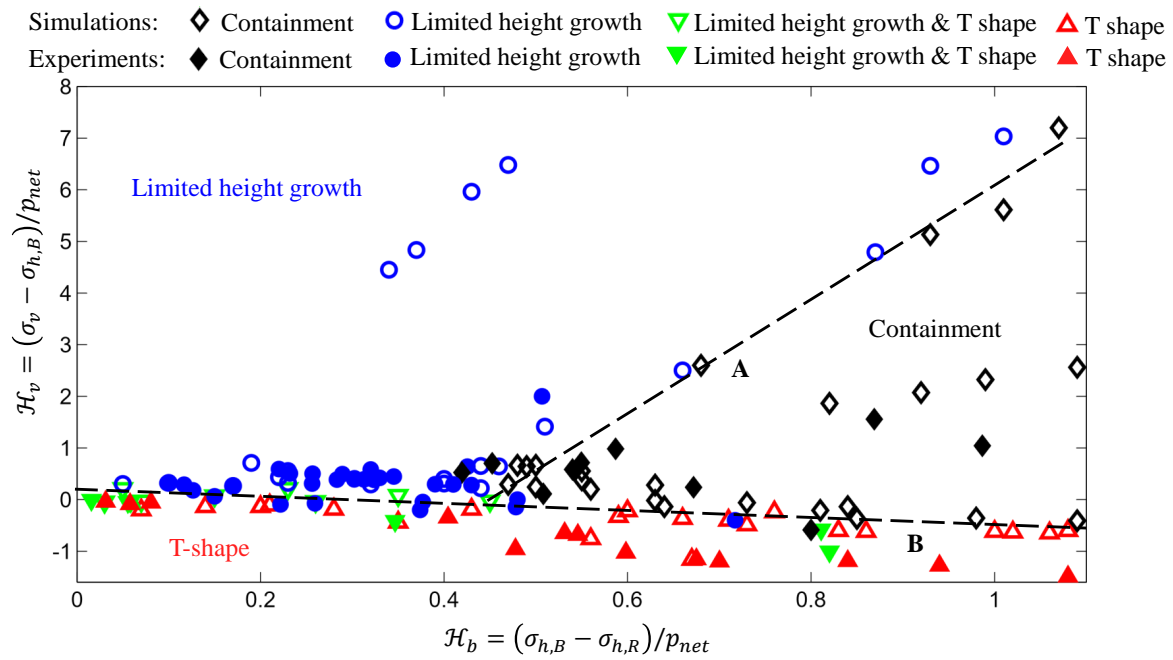


Figure 3.12: Comparison of simulation and experimental results with both zero and small toughness vertical interfaces.

For the cases with medium toughness, Fig. 3.13 shows the comparison between numerical results and experiments, and we can see they match very well. We also extend the numerical predictions to higher values of \mathcal{H}_v , again revealing boundaries dividing the parametric space into different geometries. But compared to zero/small toughness cases, the boundary line A moves leftward and boundary line B moves upward. This indicates that, compared to zero/small toughness cases, containment is obtained for smaller values of the reservoir-barrier stress contrast and T-shaped growth is obtained for larger values of the vertical stress. We also observe that the slopes of lines A and B are slightly larger. This indicates the transition between containment and height growth is less sensitive to \mathcal{H}_v and the transition to T-shaped growth is more sensitive to \mathcal{H}_b compared to the zero/small toughness cases.

Continuing this trend, we find in both numerical predictions and laboratory experiments for large toughness that the region of height growth is completely suppressed, as shown in Fig. 3.14. The boundary between containment cases and T-shape cases mainly depends on \mathcal{H}_v again with weak dependence on \mathcal{H}_b . Once again the location of the boundary line B moves upward compared to the cases of medium toughness showing that for increasing toughness of the vertical interfaces, T-shaped growth is obtained with increasingly larger vertical stress.

3.6.3 Hydraulic fracture height

So far we have only discussed height growth versus containment as a binary transition. However, for the numerical simulations of the limited height growth cases, we also study the relative fracture height H_f/H_R versus \mathcal{H}_b , where H_f is the overall fracture height, and a band results defined by the laboratory experiments are shown to occur (Fig. 3.15). Like Xing et al. (In Press), we plot the experimental value from Jeffrey & Bunger (2009), which was obtained from experiments similar to the present experiments except there was no weak interface and no contrast in elastic properties between the layers. For reference, we additionally plot the zero toughness equilibrium height growth prediction of Simonson et al. (1978). We observe that the simulation results for zero toughness cases fall into the range of the proposed curves formed by the experimental values. In the simulations H_f/H_R decreases with the increase

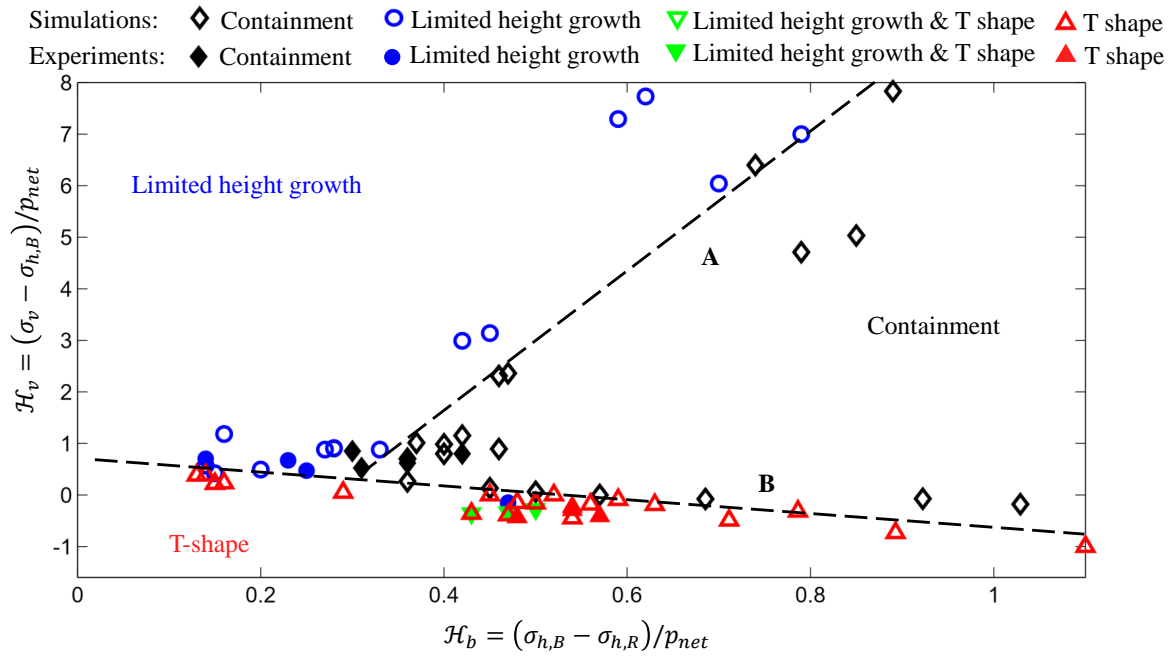


Figure 3.13: Comparison of simulation and experimental for cases with medium toughness vertical interfaces.

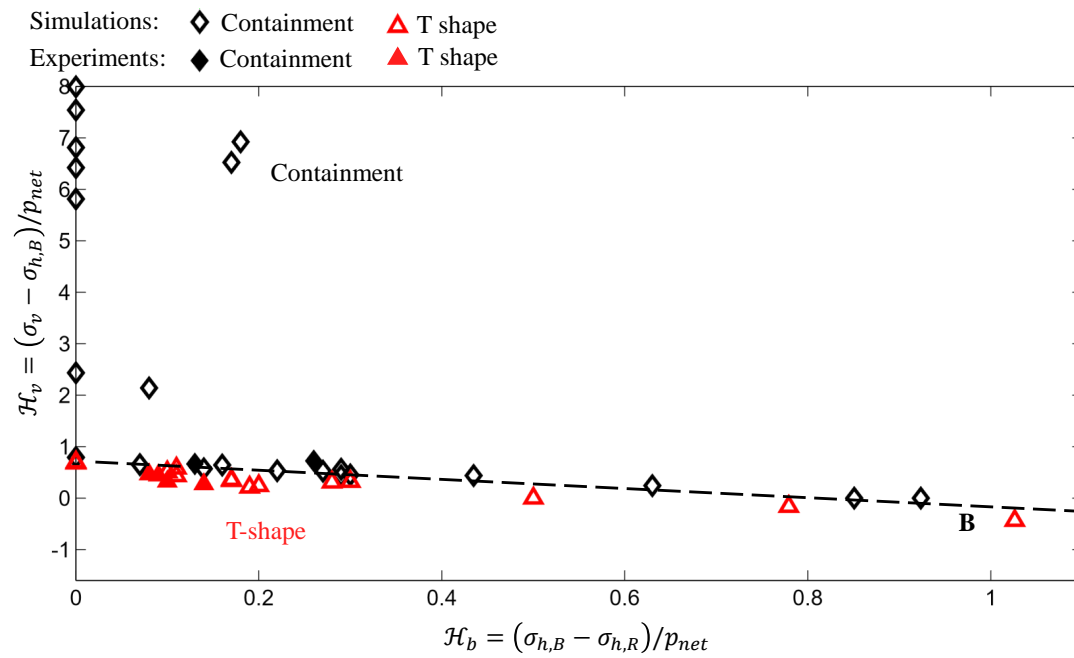


Figure 3.14: Comparison of simulation and experimental results for cases with large toughness vertical interfaces.

of \mathcal{H}_b , which is the same trend in the experiments. Note that \mathcal{H}_v in both the numerical simulations and experiments of Xing et al. (In Press) in Fig. 3.15 is in the same range (0.14 – 2.00). The simulation results also confirms that with the presence of horizontal weak interfaces H_f/H_R are smaller than that predicted by equilibrium height growth solution.

To better appreciate the role of the weak interface embodied by dependence upon \mathcal{H}_v , Fig. 3.16 presents the simulation results for H_f/H_R versus \mathcal{H}_b under small \mathcal{H}_v ($\mathcal{H}_v \leq 2$) and large \mathcal{H}_v ($\mathcal{H}_v > 2$). These are presented for for both zero & small toughness cases (Fig. 3.16a) and medium toughness cases (Fig. 3.16b). It is thus shown that, the cases with higher \mathcal{H}_v have larger relative height growth, which means increase of \mathcal{H}_v promotes height growth.

3.6.4 Discussion

For the numerical simulation cases with zero, small, and medium toughness, the parametric space can be divided into three regions corresponding to limited height growth, containment and T-shape growth respectively. T-shape growth occupies the lower part of the parametric space, indicating this geometry corresponds to small enough vertical stress. Limited height growth, on the other hand, occupies the upper left part, indicating it occurs when the vertical stress is high enough to suppress T-shaped growth but the reservoir-barrier stress contrast is insufficient to promote containment. Containment occupies the remaining upper right part of the parametric space. The results of zero toughness and and small toughness are ostensibly indistinguishable, but for medium toughness, it is easier to obtain T-shaped growth and containment cases than for small/zero toughness. For large toughness cases, we only obtain containment cases and T-shapes cases.

In the context of this problem, we observe that XSite tends to overestimate the apparent shear strength of the smooth joints. Therefore, in the simulation, we use “very weak” pre-existing joints (friction coefficient is 0.01) to model the horizontal interfaces. The friction coefficient of the simulation is smaller than the value measured in laboratory experiment (0.20) (Xing et al. In Press). By reducing the friction coefficient, we obtained the numerical results that captured the influence of weak horizontal interface which was observed in the

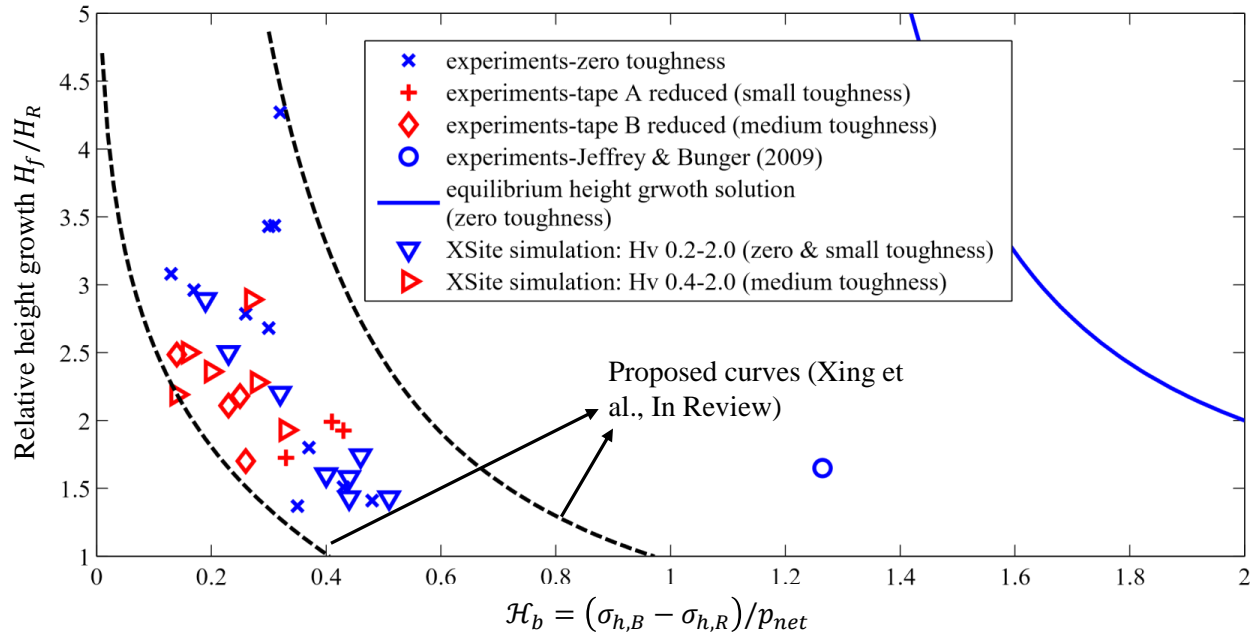


Figure 3.15: Comparison of simulation results for relative height growth H_f/H_R versus \mathcal{H}_b with experimental values and proposed curves from Xing et al. (In Press). Note that all the data presented here are characterized by asymmetric height growth upward with the reservoir height 12.7 mm and the maximum fracture length over reservoir height ratio is 6. For the Jeffrey and Bungler (2009) experimental result, the maximum fracture length over reservoir height ratio is 3.

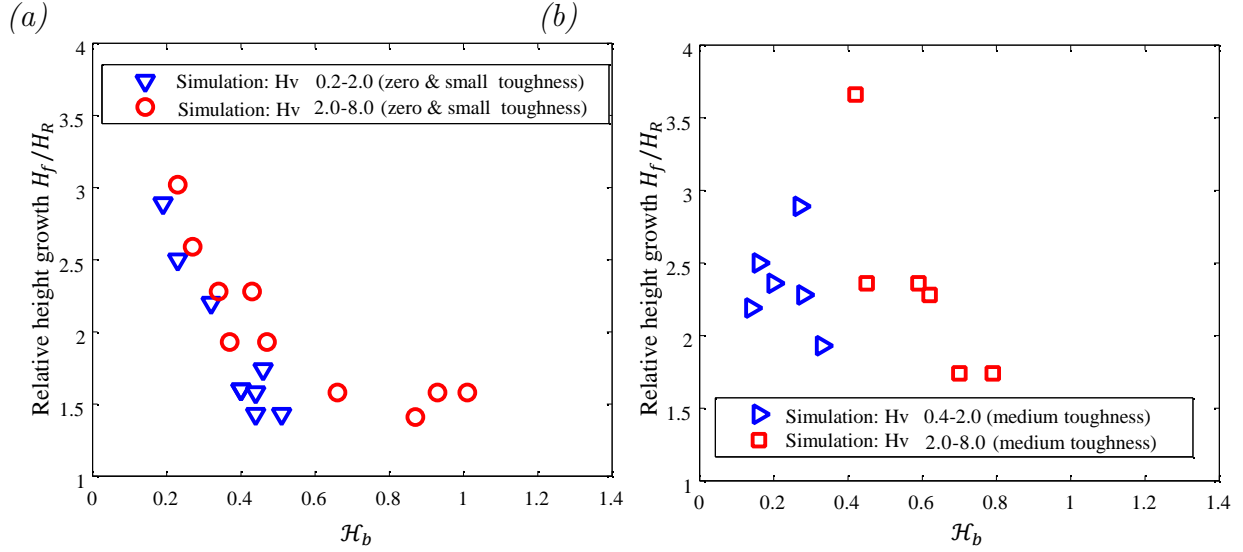


Figure 3.16: Comparison of simulation results for relative height growth H_f/H_R versus \mathcal{H}_b under different \mathcal{H}_v for (a) both small and zero toughness, and (b) medium toughness.

experiments. It is unclear whether such a modification would be required for other types of smooth joint simulation for hydraulic fracturing, however, it points to a caveat that is likely rooted in the local heterogeneity of the stress field in the lattice-type model.

Note that in the numerical study, all of the parameters including size of the specimen and the injection rate are similar to the experiments. Here we only provide the simulation cases of laboratory scale. The method of scaling the results to the field scale, especially in terms of fluid flow, remains a topic for future research.

In spite of this limitation on the scale of the simulations, one striking outcome is the dependence of height growth on the presence of the horizontal weak interface. This is shown on the one hand, rather obviously, by the existence of the T-shaped geometry for relatively small values of vertical stress. However, somewhat more subtly but equally importantly, this impact of the horizontal interface can be seen by examination of Line A separating containment from height growth cases. Specifically, we refer to the behavior in the zero, small, and medium toughness cases (Figs. 3.11-3.13), recalling that for the largest toughness cases there were no occurrences of height growth (Fig. 3.14). Firstly, we observe that the

transition from height growth to containment occurs for smaller values of the reservoir-barrier stress contrast than would be predicted by equilibrium height growth. In contrast to these numerical results, equilibrium height growth with zero toughness and ignoring the contrast in elastic properties (Simonson et al. 1978) predicts that “containment” essentially requires $p_{net} \lesssim 0.4(\sigma_{h,B} - \sigma_{h,R})$, meaning that containment should occur for $\mathcal{H}_b \gtrsim 2.5$. So, containment is clearly persisting for relatively smaller stress contrast than is predicted by equilibrium height growth.

Secondly, we observe that Line A is not a vertical line—which would have indicated independence from \mathcal{H}_v . Instead, the sloping Line A shows that the transition from containment to height growth depends upon the vertical stress. Specifically, for higher vertical stress the required reservoir-barrier stress contrast for containment is higher. We can see, then, that the results could be interpreted to approach the equilibrium height growth solution when the vertical stress is sufficiently large so as to suppress the the role of the horizontal interface.

Taken together, these observations point to the vital role of horizontal weak interfaces in determining hydraulic fracture containment. Similar observations were made based on experimental results by Xing et al. (In Press). However, because of the limitations on the range of stress contrasts available for the laboratory experiments, it was not clear if Line A depended upon \mathcal{H}_v , that is, on the vertical stress. By enabling extension of the range of parametric investigation, these numerical simulations have further clarified and indeed made more striking the impact of horizontal weak interfaces on height growth.

3.7 CHAPTER CONCLUSIONS

Numerical simulations have been carried out using a commercial lattice-based simulator to study hydraulic fracture containment. This study focuses on the influence of the horizontal confining stresses in the layers, vertical confining stress, material fracture toughness, and the horizontal weak interfaces between the reservoir and barrier layers. The goal is to benchmark the simulator with the laboratory experiments and to then use the simulator to extend the range of the parametric study. Similar to the laboratory experiments, we

simulated four distinct geometries: containment, limited height growth, T-shape growth, and the combination of T-shape and limited height growth. Also, similar to the experiments, the results of the numerical simulations can be grouped together by geometry to define distinct regions defined by the vertical stress, fluid pressure, and horizontal stress in both the reservoir and barrier layers. Finally, again as in the experiments, the numerical simulations show that with the presence of horizontal weak interfaces, the fracture height is substantially less than prediction from the classical models that neglect the influence of horizontal weak discontinuities.

The numerical results also expand the applicable region of the parametric space. These results lead to an enhanced and clarified understanding of the vital role that horizontal weak interfaces play in determining height growth. For small enough values of the vertical stress, the weak interfaces are conducive to hydraulic fracture containment, leading to T-shaped geometry. For larger values of the vertical stress, T-shaped growth is suppressed. But the weak interfaces continue to play a demonstrable role in promoting fracture containment even in the absence of T-shaped growth, evidenced by the persistence of hydraulic fracture containment even for relatively small reservoir-barrier stress contrast compared to the fluid net pressure. Importantly, as the vertical stress increases, this promotion of containment by the weak interface diminishes, meaning that for relatively larger values of the vertical stress containment requires also relatively larger values of the reservoir-barrier stress contrast. Hence, through both benchmarking to laboratory experiments and extending the range of the laboratory parametric study, these numerical simulations show that neglecting the role of weak interfaces on hydraulic fracture height growth must be done with the utmost of caution and only if the combination of stress conditions, rock strength, and horizontal interface strength can indeed show to correspond to a range where the interface is expected to play a negligible role in limiting the fracture height growth.

4.0 CONCLUSIONS

An experimental and numerical study has been carried out to explore hydraulic fracture (HF) containment. These comprise a parametric study on the influence on the fracture containment of horizontal confining stress in both the reservoir and barrier layers, vertical confining stress, material fracture toughness, and the horizontal weak interfaces between the reservoir and barrier layers.

Firstly, this study presents experimental confirmation of several theoretically-predicted asymptotic behaviors. The specimens were constructed and confining stress conditions were chosen so as to restrict the HF to a central layer within the specimen. Hence the experiments pertain to HF growth under conditions of negligible fracture toughness, with growth progressing from early-time radial geometry to large-time blade-like (PKN) geometry. These measurements show strong agreement between the evolution of the crack length and the relevant analytical solutions. Perhaps even more importantly, the crack opening in the tip region, measured using a photometric method, leads to:

- The first experimental observation of a theoretically predicted asymptotic solution of the form $w \sim s^{3/2}$ (LEFM) in the region immediately adjacent to the tip, recalling w is crack aperture and s is the distance from the crack tip,
- Confirmation of a predicted transition to an asymptotic solution of the form $w \sim s^{2/3}$ away from the tip, with the transition length scale also consistent with theory,
- The first experimental validation of a transition to an asymptotic solution of the form $w \sim s^{1/3}$ after the fracture attains blade-like (PKN) geometry,

- Evidence for the existence of a region near the tip of a blade-like (PKN) HF in which plane strain conditions persist, with the thickness of this region of the same order as the crack height.

These results show that the complex behavior of the tip region of HFs is both an inescapable and experimentally-demonstrable phenomenon. These results also combine with prior experiments ([Bunger & Detournay 2008](#)) to comprehensively validate the theoretically-predicted tip structure for HFs propagating through an impermeable solid, driven by a Newtonian fluid under conditions of laminar flow, and when fracture growth is restricted by containing barrier layers. Additionally, these comparisons between experiments and theory provide validation of the experimental methods, confirming the measurements of crack length opening and tip velocity as well as the characteristics of the fluid viscosity and the elastic moduli of the polyurethane blocks.

The attention then turns to hydraulic fracture containment/height growth experiments. These experiments are the first to obtain and systematically study the conditions leading to four distinct geometries. These are:

- 1) Complete fracture containment, which occurs with low enough net pressure when compared to the stress contrasts between the reservoir and the barrier(s) and/or between the barrier and the vertical stress acting on the horizontal weak interfaces.
- 2) T-shaped growth, which occurs when the difference between the vertical stress and the barrier stress is small enough. T-shape growth is found to be more likely to be obtained during the tests with the largest toughness and hence greatest contrast in strength relative to the unbonded horizontal interfaces.
- 3) Limited height growth characterized by vertical growth into the barrier layers, which occurs when the stress contrast between the reservoir and barrier layers is small enough relative to the net pressure and the vertical stress is large enough with respect to the barrier stress. For net fluid pressure greater than the horizontal stress contrast, our experiments exhibit limited, stable height growth while the classical equilibrium height growth model predicts uncontrolled height growth. The relative fracture height in our experiments is thus smaller than predicted by the equilibrium height growth solution.

Also, the experiments show that the relative fracture height decreases as the relative horizontal stress difference increases.

- 4) Combination cases with both height growth and T-shaped growth occupying a transition is found between limited height growth case and T-shaped growth case in both bonded and unbonded tests.

Results are grouped together in a parametric space (\mathcal{H}_b and \mathcal{H}_v) defined by the confining stresses and fluid pressure. The manner of distinguishing conditions leading to the various geometries has been both proposed and validated as a part of this research. The experimental validation is key, but limited in the range of parameters that can be explored. To expand the parametric study, numerical simulations have been carried out using a commercial, lattice type Distinct Element (DEM) hydraulic fracture simulator. The first goal is to benchmark the simulator with the laboratory experiments, and then secondly to use the simulator to extend the range of the parametric study. Similar to the laboratory experiments, the simulations predict four distinct geometries. Also, similar to the experiments, the results of the numerical simulations can be grouped together by geometry to define distinct regions in the parametric space embodying the stresses and fluid pressure. The regions defined by these groupings coincide nearly perfectly with the experiments, thus providing validation of the model. The numerical simulations show that with the presence of horizontal weak interfaces, the fracture height is substantially less than prediction from the classical models that neglect the influence of weak horizontal discontinuities. This impact of the weak interface is made more striking through the expansion of the range of the parametric study enabled by the simulations.

The results presented in this paper together lead to an enhanced and clarified understanding of the vital role that horizontal weak interfaces play in determining height growth. For small enough values of the vertical stress, the weak interfaces are conducive to hydraulic fracture containment, leading to T-shaped geometry. For larger values of the vertical stress, T-shaped growth is suppressed. But the weak interfaces continue to play a demonstrable role in promoting fracture containment even in the absence of T-shaped growth, evidenced by the persistence of hydraulic fracture containment even for relatively small reservoir-barrier stress contrast compared to the fluid net pressure. Importantly, as the vertical stress in-

creases, this promotion of containment by the weak interface diminishes, meaning that for relatively larger values of the vertical stress containment requires also relatively larger values of the reservoir-barrier stress contrast. Hence, through both benchmarking to laboratory experiments and extending the range of the laboratory parametric study, these numerical simulations show that neglecting the role of weak interfaces on hydraulic fracture height growth must be done with the utmost of caution and only if the combination of stress conditions, rock strength, and horizontal interface strength can indeed show to correspond to a range where the interface is expected to play a negligible role in limiting the fracture height growth.

APPENDIX A

SQUEEZE OUT METHOD

We use a “squeeze-out” test to calibrate the stress contrasts among different layers (see also [Xing et al. 2016](#)). The principle of the squeeze out test is rooted in the classical fluid mechanics problem wherein two rigid plates separated by a viscous fluid are loaded by diametrically-opposed forces. Following from classical treatments of this problem (reviewed in e.g. [Wikes 2005](#)), by neglecting the small variations of pressure in the y direction and hence restricting the fluid flow to be only along x direction (Figure [A1a](#)), the relationship between the total compressive force F_s and the rate of change of the thickness of the fluid layer is given by

$$\sigma_s = \frac{F_s}{a_s b_s} = \frac{3\mu a_s^2}{2w^3} \frac{dw}{dt}, \quad (\text{A.1})$$

where w is the thickness of the fluid, a_s and b_s are the width and length of the plates (Figure [A1a](#)) and μ is the viscosity of the fluid, known from testing using a Canon-Fenske viscometer.

The width is then obtained from photometric analysis of video images, that is, using the light absorbance of fluid filled region according to [Bunger \(2006\)](#)

$$A \equiv \log_{10} \left(\frac{I_0}{I} \right) = \frac{w}{k}. \quad (\text{A.2})$$

Here k is a photometric constant, I is the intensity of light, and I_0 is the intensity of light in the reference (initial) configuration. The photometric constant k is determined in relation to the concentration of dye by a calibration method that uses fluid-filled wedges of known

thickness, as described in [Bunger \(2006\)](#), also verified by linear variable differential transducer (LVDT). Thus, taking k to be known from separate calibrations and the absorbance A to be data obtained from video images, Equation [A.1](#) can be rewritten as

$$\sigma_s = \frac{3\mu a_s^2}{2k^2 A^3} \frac{dA}{dt}. \quad (\text{A.3})$$

The premise, then, is that if fluid is initially placed in each layer (interfaces between 1-6, 2-5, and 3-4 in [Figure A1b](#)), and if each layer is subjected to a different stress, then these different stresses can be ascertained from Equation [A.3](#) using the evolution of the absorbance in each layer as measured from video images. Please note that the fluid among different layers is separated by a thin film to avoid flow across the layers so that the fluid flow is also restricted in x direction. To illustrate, under a certain applied load (i.e. the total force by a pair of actuators, [Figure 2.1](#)), the variation of absorbance of light of three layers with time is shown in [Figure A2a](#). Using this data and Equation [A.3](#), and repeating the experiment for varying levels of applied load, the relationship among the confining stresses in the three layers can be obtained, as shown in [Figure A2b](#). The repeatability of the squeeze out tests show that the error is in the order of ten percent.

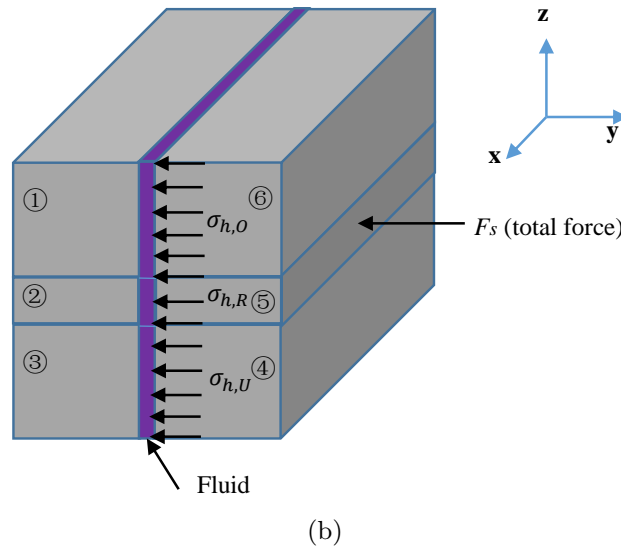
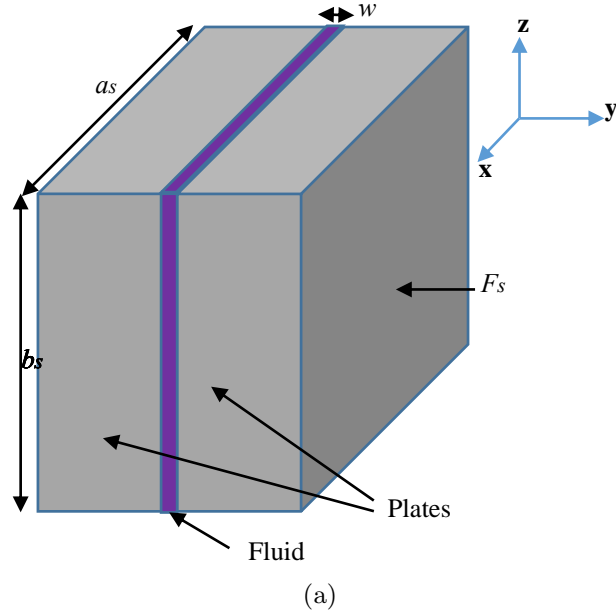


Figure A1: Squeeze-out experiments, showing a) two rectangular plates separated by a viscous fluid layer and the fluid flow restricted in x direction, where a_s and b_s are the width and length of the plates and F_s is the applied compressive force, and b) the setup for the experiment with fluid being initially placed between all 3 layers (analogue reservoir and 2 barriers in Figure 2.1) and squeezed out simultaneously by an applied load (note that the fluid among different layers is separated by a thin film to avoid flow across the layers so that the fluid flow is also restricted in x direction). Here $\sigma_{h,U}$ is the stress of the bottom barrier, $\sigma_{h,R}$ is the stress of the analogue reservoir, and $\sigma_{h,O}$ is the stress of the top barrier. Figure adapted from Xing et al. (2016).

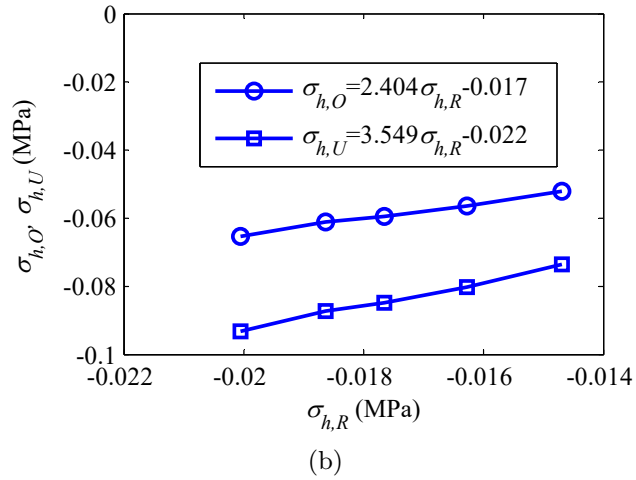
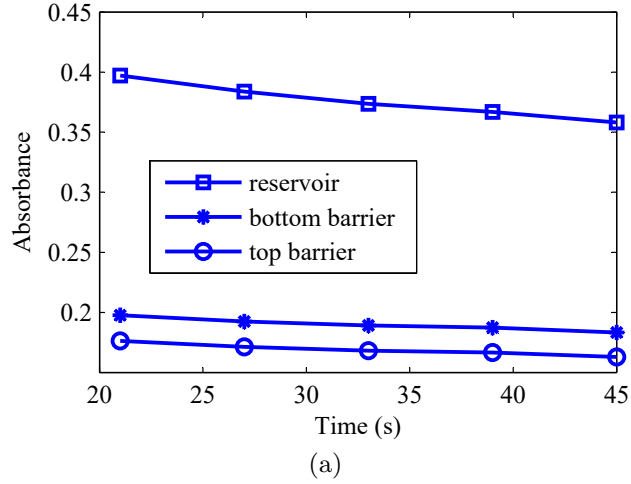


Figure A2: The results of the squeeze out test, showing a) absorbance variation with time of three layers, and b) the relationship of the stress among different layers ($\sigma_{h,U}$ is the stress of the bottom barrier, $\sigma_{h,R}$ is the stress of the analogue reservoir, and $\sigma_{h,O}$ is the stress of the top barrier). Figure adapted from [Xing et al. \(2016\)](#).

APPENDIX B

INTERFACE FRACTURE TOUGHNESS MEASUREMENT

Double notch tension laboratory tests (see Figure B1) were used to obtain the fracture toughness of the interfaces bonded by adhesives. In the tests, two small PU blocks with dimension of 50 mm×50 mm×25 mm ($b=12.5$ mm, $h=50$ mm) are bonded together and on each side of the interface an approximately 5 mm notch is made by leaving it unbonded. The specimen is then placed in a loading machine and loaded by displacement control. We have carried out these tests with three different types of adhesives on PU with Young's modulus 100 MPa: tape A, tape A reduced, and tape B reduced. The typical loading-displacement curves of the tests with three adhesives are plotted in Figure B2.

Because some of the curves (especially tape A) exhibit strongly non-brittle properties, it is necessary to use critical energy to represent the criteria of fracture propagation. It is convenient to divide J into elastic and plastic components:

$$J = J_{el} + J_{pl}. \quad (\text{B.1})$$

The elastic J_{el} is compute from the elastic stress intensity:

$$J_{el} = \frac{K_{el}^2}{E'}. \quad (\text{B.2})$$

And K_{el} can be inferred from (Tada et al. 2000) at the peak load:

$$K_I = \sigma \sqrt{\pi a} F\left(\frac{a}{b}\right), \quad (\text{B.3})$$

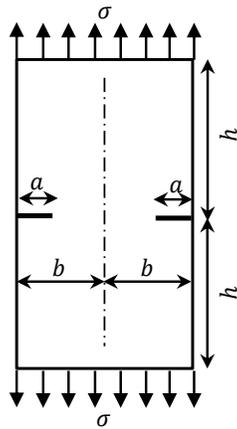


Figure B1: The double notch direct tension specimen (after [Tada et al. 2000](#)). Here σ is the applied stress, b is the half of the initial crack length, a is the half of the specimen width, and h is the specimen height.

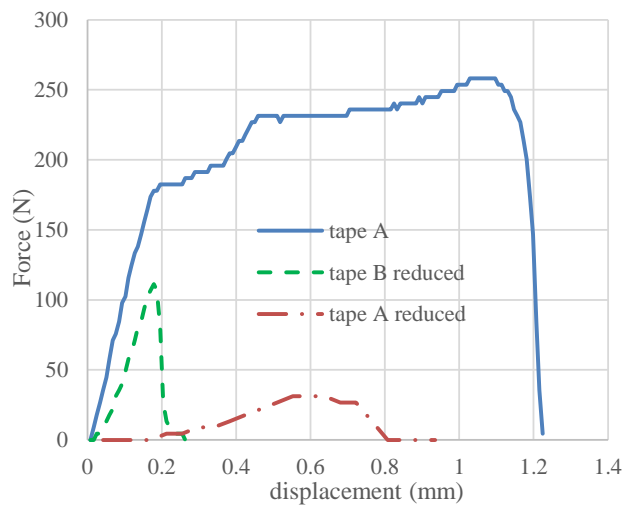


Figure B2: The force-displacement of double notch tension tests of PU sub-block bounded by adhesives.

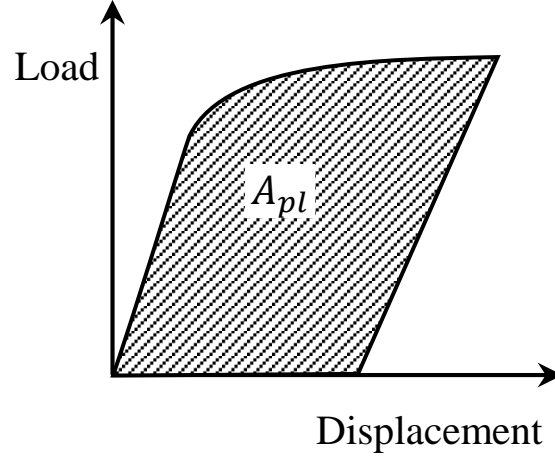


Figure B3: Plastic energy absorbed by a test specimen during a critical energy release rate test (after [Anderson 2005](#)). Here A_{pl} is the plastic area under the load-displacement curve.

where $F(a/b)$ is obtained by numerical simulations. The basic procedure in ASTM E 1820 includes a simplified method for computing J_{pl} from the plastic area under the load-displacement curve (see [Figure B2](#)):

$$J_{pl} = \frac{\eta A_{pl}}{B_N b_o}, \quad (\text{B.4})$$

where $\eta_{pl} = 1.9$ is a dimensionless constant, A_{pl} is the plastic area under the load-displacement curve, B_N is the thickness, and b_o is the initial ligament length. Then the corresponding fracture toughness K_{Ic} that includes both the elastic and plastic behavior can be calculated as

$$K_{Ic} = \sqrt{J E'}. \quad (\text{B.5})$$

The average fracture toughness K_{Ic} for each adhesive is listed in [Table B1](#).

Table B1: Fracture toughness for PU specimen with various adhesives

Adheisve	Tape A	Tape B reduced	Tape A reduced
K_{Ic} (MPa.m ^½)	0.40	0.069	0.026

APPENDIX C

HYDRAULIC FRACTURE GROWTH RATE

In the containment case, the hydraulic fracture grows from an early time radial shape to large time blade-like (PKN) shape. The evolution of the crack radius of radial shape hydraulic fracture under negligibly-small fracture toughness can be expressed as (Savitski & Detournay 2002)

$$L = 0.5277 \left(\frac{E'(2V_c)^3}{\mu} \right)^{1/9} t^{1/9}. \quad (\text{C.1})$$

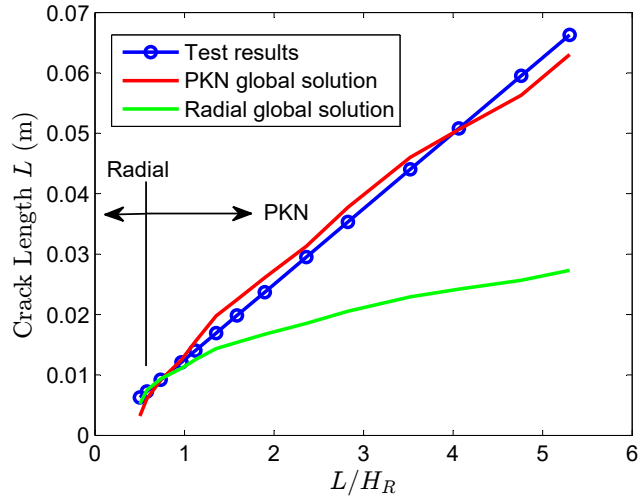
Here we have replaced the product $Q_o t$ in the original solution, where Q_o is a constant injection rate, with $2V_c$, representing the crack volume. Technically the original solution is valid for constant injection rate Q_o while the Q_o is not strictly constant due to the compressibility of the injection system in the experiments. Therefore, we introduce the actual volume of the crack V_c , which can be measured in the experiments.

In the case when hydraulic fracture is much longer than its height and when the height growth is completely contained by barrier layers, based on Nordgren's solution (Nordgren 1972) and similarly introducing half-volume of the crack V_c , the evolution of the crack length is given by

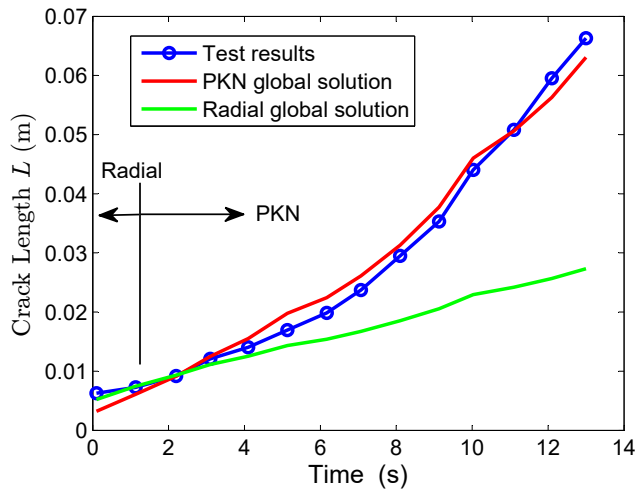
$$L = 0.68 \left(\frac{E'V_c^3}{2\mu H_f^4} \right)^{1/5} t^{1/5}, \quad (\text{C.2})$$

where H_f is the crack height.

The comparison of measured hydraulic fracture growth rate of one typical containment case with the theoretical solution is described in Figure C1 (see also Xing et al. (2017)).



(a)



(b)

Figure C1: Measured crack length in the containment case scaled by a) Radial global solution and b) PKN global solution vs ratio of crack length over height L/H_R . In the test, analogue reservoir height H_R is 12.7 mm. Figure from Xing et al. (2017) (with permission).

As shown, the measured crack length during the radial portion of the growth (early time or $L/H_R \leq 1$) is close to the radial solution given by Equation C.1. As length increases relative to the height (early time or $L/H_R > 1$), it approaches the PKN solution given by Equation C.2.

BIBLIOGRAPHY

- Abbas, S., Gordeliy, E., Peirce, A., Lecampion, B., Chuprakov, D. & Prioul, R. (2014), Limited height growth and reduced opening of hydraulic fractures due to fracture offsets: An xfm application, *in* ‘SPE Hydraulic Fracturing Technology Conference’, Society of Petroleum Engineers. SPE-168622.
- Adachi, J. & Detournay, E. (2002), ‘Self-similar solution of a plane-strain fracture driven by a power-law fluid’, *International Journal for Numerical and Analytical Methods in Geomechanics* **26**(6), 579–604.
- Adachi, J. I. & Peirce, A. P. (2008), ‘Asymptotic analysis of an elasticity equation for a finger-like hydraulic fracture’, *Journal of Elasticity* **90**(1), 43–69.
- Adachi, J., Siebrits, E., Peirce, A. & Desroches, J. (2007), ‘Computer simulation of hydraulic fractures’, *International Journal of Rock Mechanics and Mining Sciences* **44**(5), 739–757.
- Anderson, T. L. (2005), *Fracture Mechanics: Fundamentals and Applications*, CRC press.
- Blanton, T. L. et al. (1986), Propagation of hydraulically and dynamically induced fractures in naturally fractured reservoirs, *in* ‘SPE unconventional gas technology symposium’, Society of Petroleum Engineers. SPE-15261.
- Bolander, J. E. & Sukumar, N. (2005), ‘Irregular lattice model for quasistatic crack propagation’, *Physical Review B* **71**(9), 094106.
- Brown, E. & Hoek, E. (1978), ‘Trends in relationships between measured in-situ stresses and depth’, *International Journal of Rock Mechanics and Mining Sciences & Geomechanics Abstracts* **15**(4), 211–215.
- Bunger, A., Jeffrey, R. G. & Zhang, X. (2014), ‘Constraints on simultaneous growth of hydraulic fractures from multiple perforation clusters in horizontal wells’, *SPE Journal* **19**(04), 608–620.
- Bunger, A. P. (2006), ‘A photometry method for measuring the opening of fluid-filled fractures’, *Measurement Science and Technology* **17**(12), 3237–3244.
- Bunger, A. P. & Detournay, E. (2008), ‘Experimental validation of the tip asymptotics for a fluid-driven crack’, *Journal of the Mechanics and Physics of Solids* **56**(11), 3101–3115.

- Bunger, A. P., Detournay, E. & Jeffrey, R. G. (2005), ‘Crack tip behavior in near-surface fluid-driven fracture experiments’, *Comptes Rendus Mecanique* **333**(4), 299–304.
- Bunger, A. P., Gordeliy, E. & Detournay, E. (2013), ‘Comparison between laboratory experiments and coupled simulations of saucer-shaped hydraulic fractures in homogeneous brittle-elastic solids’, *Journal of the Mechanics and Physics of Solids* **61**(7), 1636–1654.
- Bunger, A. P., Lakirouhani, A. & Detournay, E. (2010), Modelling the effect of injection system compressibility and viscous fluid flow on hydraulic fracture breakdown pressure, in ‘Rock stress and earthquakes-proceedings of the 5th international symposium on in-situ rock stress, 25-27 August, Beijing, China’, Beijing, China, pp. 59–67. ISRM-ISRS-2010-008.
- Chuprakov, D., Melchaeva, O. & Prioul, R. (2014), ‘Injection-sensitive mechanics of hydraulic fracture interaction with discontinuities’, *Rock mechanics and rock engineering* **47**(5), 1625–1640.
- Cundall, P. (2001), ‘A discontinuous future for numerical modelling in geomechanics?’, *Proceedings of the Institution of Civil Engineers-Geotechnical Engineering* **149**(1), 41–47.
- Cundall, P. (2011), Lattice method for modeling brittle, jointed rock, in ‘Proceedings of the 2nd International FLAC/DEM Symposium on Continuum and Distinct Element Numerical Modeling in Geomechanics, Melbourne, Australia’.
- Cundall, P. A. (1971), A computer model for simulating progressive, large-scale movements in blocky rock system, in ‘Proc. Int. Symp. for ISRM, Nancy, Paper II-8’, number 8.
- Damjanac, B. & Cundall, P. (2016), ‘Application of distinct element methods to simulation of hydraulic fracturing in naturally fractured reservoirs’, *Computers and Geotechnics* **71**, 283–294.
- Damjanac, B., Detournay, C. & Cundall, P. (2013), Three-dimensional numerical model of hydraulic fracturing in fractured rock masses, in ‘Effective and sustainable hydraulic fracturing’, InTech, Chapter 41.
- Damjanac, B., Detournay, C. & Cundall, P. A. (2015), ‘Application of particle and lattice codes to simulation of hydraulic fracturing’, *Computational Particle Mechanics* **3**(2), 249–261.
- Daneshy, A. A. (1978), ‘Hydraulic fracture propagation in layered formations’, *Society of Petroleum Engineers Journal* **18**(01), 33–41.
- de Pater, C. J. (2015), Hydraulic fracture containment: New insights into mapped geometry, in ‘SPE Hydraulic Fracturing Technology Conference, 3-5 February, The Woodlands, Texas, USA’, Society of Petroleum Engineers. SPE-173359.
- de Pater, C. J. & Dong, Y. (2009), Fracture containment in soft sands by permeability or strength contrasts, in ‘SPE Hydraulic Fracturing Technology Conference, 19-21 January, The Woodlands, Texas, USA’, Society of Petroleum Engineers. SPE-119634.

- Desroches, J., Detournay, E., Lenoach, B., Papanastasiou, P., Pearson, J., Thiercelin, M. & Cheng, A. (1994), The crack tip region in hydraulic fracturing, *in* ‘Proceedings of the Royal Society of London A: Mathematical, Physical and Engineering Sciences’, Vol. 447, The Royal Society, pp. 39–48.
- Detournay, E. (2004), ‘Propagation regimes of fluid-driven fractures in impermeable rocks’, *International Journal of Geomechanics* **4**(1), 35–45.
- Detournay, E. (2016), ‘Mechanics of hydraulic fractures’, *Annual Review of Fluid Mechanics* **48**, 311–339.
- Detournay, E. & Peirce, A. (2014), ‘On the moving boundary conditions for a hydraulic fracture’, *International Journal of Engineering Science* **84**, 147–155.
- Diamond, W. P. & Oyler, D. (1987), Effects of stimulation treatments on coalbeds and surrounding strata: evidence from underground observations. report of investigations 9083, Technical report, Bureau of Mines, Pittsburgh, PA (USA). Pittsburgh Research Center.
- Economides, M. J. & Nolte, K. G. (2000), *Reservoir Stimulation*, John Wiley & Sons, Chichester UK, 3rd edition.
- El Rabaa, W. (1987), Hydraulic fracture propagation in the presence of stress variation, *in* ‘SPE Annual Technical Conference and Exhibition, 27-30 September, Dallas, Texas, USA’, Society of Petroleum Engineers. SPE-16898.
- Garagash, D. & Detournay, E. (2000), ‘The tip region of a fluid-driven fracture in an elastic medium’, *Journal of applied mechanics* **67**(1), 183–192.
- Garagash, D. I. (2009), Scaling of physical processes in fluid-driven fracture: perspective from the tip, *in* ‘IUTAM symposium on scaling in solid mechanics’, Springer, pp. 91–100.
- Garagash, D., Rohde, A. & Bunger, A. (2009), Leading edge of a hydraulic fracture crossing a stress boundary, *in* ‘Proceedings 12th International Conference on Fracture, July 12-17, Ottawa, Canada’.
- Geertsma, J. & De Klerk, F. (1969), ‘A rapid method of predicting width and extent of hydraulically induced fractures’, *Journal of Petroleum Technology* **21**(12), 1–571. SPE-2458.
- Grassl, P. (2009), ‘A lattice approach to model flow in cracked concrete’, *Cement and Concrete Composites* **31**(7), 454–460.
- Grassl, P. & Bažant, Z. P. (2009), ‘Random lattice-particle simulation of statistical size effect in quasi-brittle structures failing at crack initiation’, *Journal of engineering mechanics* **135**(2), 85–92.

- Grassl, P., Fahy, C., Gallipoli, D. & Wheeler, S. J. (2015), ‘On a 2d hydro-mechanical lattice approach for modelling hydraulic fracture’, *Journal of the Mechanics and Physics of Solids* **75**, 104–118.
- Gu, H., Weng, X., Lund, J. B., Mack, M. G., Ganguly, U. & Suarez-Rivera, R. (2012), ‘Hydraulic fracture crossing natural fracture at nonorthogonal angles: a criterion and its validation’, *SPE Production & Operations* **27**(01), 20–26. SPE-139984.
- Hoskins, E., Jaeger, J. & Rosengren, K. (1968), ‘A medium-scale direct friction experiment’, *International Journal of Rock Mechanics and Mining Sciences & Geomechanics Abstracts* **5**(2), 143–152.
- Irwin, G. R. (1957), ‘Analysis of stresses and strains near the end of a crack traversing a plate’, *ASME J. Appl. Mech.* **24**(361-364), 4.
- Itasca Consulting Group, I. (2014a), *PFC2D Particle flow code in 2 dimensions version 5.0*, Minneapolis.
- Itasca Consulting Group, I. (2014b), *PFC3D Particle flow code in 3 dimensions version 5.0*, Minneapolis.
- Jeffrey, R. G., Brynes, R. P., Lynch, P. J. & Ling, D. J. (1992), An analysis of hydraulic fracture and mineback data for a treatment in the german creek coal seam, *in* ‘SPE Rocky Mountain Regional Meeting, 18-21 May, Casper, Wyoming, USA’, Society of Petroleum Engineers. SPE-24362.
- Jeffrey, R. G. & Bungler, A. (2009), ‘A detailed comparison of experimental and numerical data on hydraulic fracture height growth through stress contrasts’, *SPE Journal* **14**(03), 413–422. SPE-106030.
- Johnson, E. & Cleary, M. P. (1991), Implications of recent laboratory experimental results for hydraulic fractures, *in* ‘Low Permeability Reservoirs Symposium, 15-17 April, Denver, Colorado, USA’, Society of Petroleum Engineers. SPE-21846.
- Kovalyshen, Y. & Detournay, E. (2010), ‘A reexamination of the classical pkn model of hydraulic fracture’, *Transport in porous media* **81**(2), 317–339.
- Kresse, O., Weng, X., Gu, H. & Wu, R. (2013), ‘Numerical modeling of hydraulic fractures interaction in complex naturally fractured formations’, *Rock mechanics and rock engineering* **46**(3), 555–568.
- Lakirouhani, A., Detournay, E. & Bungler, A. (2016), ‘A reassessment of in situ stress determination by hydraulic fracturing’, *Geophysical Journal International* **205**(3), 1859–1873.
- Lecampion, B., Desroches, J., Jeffrey, R. G., Bungler, A. P. & Burghardt, J. (2015), Initiation and breakdown of transverse hydraulic fracture: theory and experiments, *in* ‘Proceedings 13th International Society for Rock Mechanics (ISRM) Congress, 10-13 May, Montreal, Canada’. ISRM-13CONGRESS-2015-285.

- Lecampion, B., Peirce, A., Detournay, E., Zhang, X., Chen, Z., Bungler, A., Detournay, C., Napier, J., Abbas, S. & Garagash, D. (2013), The impact of the near-tip logic on the accuracy and convergence rate of hydraulic fracture simulators compared to reference solutions, *in* 'ISRM International Conference for Effective and Sustainable Hydraulic Fracturing', International Society for Rock Mechanics.
- Mendelsohn, D. (1984a), 'A review of hydraulic fracture modeling-ii: 3d modeling and vertical growth in layered rock', *ASME J. Energy Resour. Technol* **106**(4), 543–553.
- Mendelsohn, D. (1984b), 'A review of hydraulic fracture modeling-part i: general concepts, 2d models, motivation for 3d modeling', *ASME J. Energy Resour. Technol* **106**(3), 369–376.
- Meyer, B. R. & Bazan, L. W. (2011), A discrete fracture network model for hydraulically induced fractures-theory, parametric and case studies, *in* 'SPE Hydraulic Fracturing Technology Conference, The Woodlands, Texas, USA.', Society of Petroleum Engineers. SPE-140514.
- Nolte, K. G. & Smith, M. B. (1981), 'Interpretation of fracturing pressures', *Journal of Petroleum Technology* **33**(09), 1147–1155.
- Nordgren, R. (1972), 'Propagation of a vertical hydraulic fracture', *Society of Petroleum Engineers Journal* **12**(04), 306–314.
- Peirce, A. & Detournay, E. (2008), 'An implicit level set method for modeling hydraulically driven fractures', *Computer Methods in Applied Mechanics and Engineering* **197**(33), 2858–2885.
- Perkins, T. & Kern, L. (1961), 'Widths of hydraulic fractures', *Journal of Petroleum Technology* **13**(09), 937–949. SPE-89-PA.
- Pierce, M., Cundall, P., Potyondy, D. & Mas Ivars, D. (2007), A synthetic rock mass model for jointed rock, *in* 'Rock Mechanics: Meeting Society's Challenges and Demands, 1st Canada-US Rock Mechanics Symposium, Vancouver, May 2007', Vol. 1, pp. 341–349.
- Pine, R. & Cundall, P. (1985), Applications of the fluid-rock interaction program (frip) to the modelling of hot dry rock geothermal energy systems, *in* 'Proc. Int. Symp. on Fundamentals of Rock Joints, Bjorklidn', Centek, pp. 293–302.
- Potyondy, D. & Cundall, P. (2004), 'A bonded-particle model for rock', *International Journal of Rock Mechanics and Mining Sciences* **41**(8), 1329–1364.
- Renshaw, C. & Pollard, D. (1995), 'An experimentally verified criterion for propagation across unbounded frictional interfaces in brittle, linear elastic materials', **32**(3), 237–249.
- Rice, J. R. (1968), 'Mathematical analysis in the mechanics of fracture', *Fracture: an advanced treatise* **2**, 191–311.

- Rohde, A. & Bungler, A. (2009), Fluid flow visualization for hydraulic fracture experiments, *in* ‘Proceedings Second Thailand Rock Mechanics Symposium, March 12-13, Chonburi, Thailand’.
- Savitski, A. & Detournay, E. (2000), Propagation of a penny-shape hydraulic fracture in an impermeable rock, *in* ‘Rock Mechanics for Industry – Proc. 37th US Rock Mechanics Symp., Rotterdam: Balkema’, pp. 851–858.
- Savitski, A. & Detournay, E. (2002), ‘Propagation of a penny-shaped fluid-driven fracture in an impermeable rock: asymptotic solutions’, *International Journal of Solids and Structures* **39**(26), 6311–6337.
- Schlangen, E. & Garboczi, E. (1997), ‘Fracture simulations of concrete using lattice models: computational aspects’, *Engineering Fracture Mechanics* **57**(2), 319–332.
- Settari, A. & Cleary, M. P. (1984), ‘Three-dimensional simulation of hydraulic fracturing’, *Journal of Petroleum Technology* **36**(07), 1–177.
- Simonson, E. R., Abou-Sayed, A. S. & Clifton, R. J. (1978), ‘Containment of massive hydraulic fractures’, *Society of Petroleum Engineers Journal* **18**(01), 27–32.
- Spence, D. & Sharp, P. (1985), Self-similar solutions for elastohydrodynamic cavity flow, *in* ‘Proceedings of the Royal Society of London A: Mathematical, Physical and Engineering Sciences’, Vol. 400, The Royal Society, pp. 289–313.
- Stone, R. A. & Shafer, S. A. (1994), ‘Determination of surface roughness from reflected step edges’, *Journal of the Optical Society of America A* **11**(11), 2969–2980.
- Tada, H., Paris, P. & Irwin, G. (2000), *The Stress Analysis of Cracks Handbook*, 3 edn, New York: ASME Press.
- Teufel, L. W. & Clark, J. A. (1984), ‘Hydraulic fracture propagation in layered rock: experimental studies of fracture containment’, *Society of Petroleum Engineers Journal* **24**(01), 19–32.
- Van Eekelen, H. A. M. (1982), ‘Hydraulic fracture geometry: Fracture containment in layered formations’, *Soc Pet Engr J* **22**(03), 341–349.
- Warpinski, N., Abou-Sayed, I., Moschovidis, Z. & Parker, C. (1993), ‘Hydraulic fracture model comparison study: Complete results. tech. rep. sand93-7042’, *Sandia National Laboratories*.
- Warpinski, N. R. & Teufel, L. W. (1987), ‘Influence of geologic discontinuities on hydraulic fracture propagation (includes associated papers 17011 and 17074)’, *Journal of Petroleum Technology* **39**(02), 209–220.
- Wikes, J. O. (2005), *Fluid Mechanics for Chemical Engineers with Microfluidics and CFD*, Prentice Hall, 2nd edition.

- Wu, R., Bunger, A., Jeffrey, R. & Siebrits, E. (2008), A comparison of numerical and experimental results of hydraulic fracture growth into a zone of lower confining stress, *in* 'The 42nd US Rock Mechanics Symposium (USRMS), 29 June-2 July, San Francisco, California, USA', American Rock Mechanics Association. ARMA-08-267.
- Xing, P., Bunger, A. P., Yoshioka, K., Adachi, J. & El-Fayoumi, A. (2016), Experimental study of hydraulic fracture containment in layered reservoirs, *in* '50th US Rock Mechanics/Geomechanics Symposium, 26-29 June, Houston, Texas, USA', American Rock Mechanics Association. ARMA-2016-049.
- Xing, P., Yoshioka, K., Adachi, J., El-Fayoumi, A. & Bunger, A. P. (2017), 'Laboratory measurement of tip and global behavior for zero-toughness hydraulic fractures with circular and blade-shaped (pkn) geometry', *Journal of the Mechanics and Physics of Solids* .
- Xing, P., Yoshioka, K., Adachi, J., El-Fayoumi, A. & Bunger, A. P. (In Press), 'Laboratory demonstration of hydraulic fracture height growth across weak discontinuities', *Submitted to Geophysics* . Conditional Acceptance on 14 November 2017.
- Xing, P., Yoshioka, K., Adachi, J., El-Fayoumi, A., Damjanac, B. & Bunger, A. P. (In Preparation), 'Lattice simulation of hydraulic fracture containment in layered reservoirs', *To be Submitted to Computers and Geotechnics* .